NTNU
Norwegian University of
Science and Technology

A CFD-model of the Fluid Flow in a Hydrogen Peroxide Monopropellant Rocket Engine in ANSYS Fluent 16.2

Frida Vestnes

Norges teknisk-
naturvitenskapelige universitet
NTNU

Fakultet for ingeniørvitenskap og teknologi
Institutt for energi- og prosessteknikk

⊙ NTNU

EPT-P-2015-149

HOVEDOPPGAVE

for

Frida Vestnes

Vår 2016

CFD- beregning av strømning med faseovergang for hydrogen peroksid i rakettmotor

CFD-model of fluid flow with phase change in hydrogen peroxide for rocket propulsion

Bakgrunn

Et klassisk prinsipp for rakettfremdrift benytter en katalytisk kjemisk reaksjon mellom hydrogen peroksid og en katalysator, bestående primært av en porøs plugg bygget opp av sølvpletterte ståltråder i en gitterstruktur. Den frigjorte gassen ekspanderes gjennom en dyse for å generere ønsket skyv kraft på raketten. Grunnleggende teoretiske elementer i konseptet ble diskutert i en prosjektoppgave høsten 2015, og et aktuelt CFD verktøy ANSYS/Fluent ble identifisert som realistisk ramme for kvantitativ numerisk beregning av strømning med fase – og varmeovergang gjennom en slik reaktor. Fysiske og kjemiske parametere, samt valgte driftsbetingelser, er avgjørende for stabil operasjon av konseptet, og numerisk simulering antas å være det mest aktuelle verktøyet for å oppnå øket innsikt i slike forhold.

Mål

Oppgaven bearbeides ut fra følgende punkter:

1.
2.
3.

---- " ---

Belastningen på prosjektet utgjør 15 studiepoeng.

Besvarelsen redigeres mest mulig som en forskningsrapport med innholdsfortegnelse, et sammendrag på norsk, konklusjon, litteraturliste, etc. Ved utarbeidelsen av teksten skal kandidaten legge vekt på å gjøre teksten oversiktlig og velskrevet. Med henblikk på lesing av besvarelsen er det viktig at de nødvendige henvisninger for korresponderende steder i tekst, tabeller og figurer anføres på begge steder. Ved bedømmelsen legges det stor vekt på at

resultatene er grundig bearbeidet, og at de oppstilles tabellarisk og/eller grafisk på en oversiktlig måte og diskuteres utførlig.

Det forutsettes at kandidaten på eget initiativ etablerer et tilfredsstillende kontaktforhold med faglærer og eventuelle veileder(e).

Risikovurdering av kandidatens arbeid skal gjennomføres i henhold til instituttets prosedyrer. Risikovurderingen skal dokumenteres og inngå som del av besvarelsen. Hendelser relatert til kandidatens arbeid med uheldig innvirkning på helse, miljø eller sikkerhet, skal dokumenteres og inngå som en del av besvarelsen. Hvis dokumentasjonen på risikovurderingen utgjør veldig mange sider, leveres den fulle versjonen elektronisk til veileder og et utdrag inkluderes i besvarelsen.

I henhold til "Utfyllende regler til studieforskriften for teknologistudiet/sivilingeniørstudiet" ved NTNU § 20, forbeholder instituttet seg retten til å benytte alle resultater og data til undervisnings- og forskningsformål, samt til fremtidige publikasjoner.

Besvarelsen leveres til instituttet innbundet i 3 komplette eksemplarer.

Leveringsfrist: *22. Juni 2016.*

☐ Arbeid i laboratorium (vannkraftlaboratoriet, strømningsteknisk, varmeteknisk)
☐ Feltarbeid

Institutt for energi- og prosessteknikk, 12. Januar 2016.

_____   _____
Olav Bolland   Tor Ytrehus
Instituttleder   Faglærer/veileder

Acknowledgement

Summary

The use of hydrazine in monopropellant thrusters has dominated the market for several decades. Due to the toxic nature of hydrazine, the interest in developing thrusters based on green propellants has increased. A common issue found during the development of these thrusters is the optimisation of the catalyst used to decompose the liquid propellant into a hot gas. The work presented in this thesis was therefore performed in order to evaluate if it is possible to simulate the fluid flow of a hydrogen peroxide thruster with the commercially available CFD software ANSYS Fluent 16.2. A successful simulation would make it possible to investigate the fluid flow inside the catalyst, which could lead to an optimised design without the large costs connected to the optimisation process through extensive tests.

Through an extensive research on the different models available in the commercial CFD software ANSYS Fluent 16.2 it was found that the software should be able to model this problem. As the phases in a HTP thruster were found not to be in an equilibrium, the fluid flow had to be modelled by the complex Eulerian multiphase model. The different chemical substances were modelled through the species model. The pressure drop over the catalyst was modelled as a porous media. The heterogeneous reaction mechanism for HTP and vaporisation of water was modelled through a volumetric reaction model and two-resistance model respectively, as part of the phase interaction methods. The turbulent flow in the thruster was modelled with the $k - \omega$ turbulence model.

The simulations performed with the Eulerian multiphase model did not converge despite taking several measures to stabilise the solver. The simulation was therefore split into different cases, where one sub-case built on the previous case results, to find the root cause of the stability issues. Through these simulations it was found that the Eulerian multiphase model is not capable of handling the compressible flow in this simulation. An attempt to model the flow with the mixture multiphase model was therefore attempted.

By comparing the simulation results obtained for mixture model case 1 and 2 with experimental test data the results in case 1 were verified and validated. The porous media model was concluded to be modelled incorrectly as the pressure drop far exceeded results found during experimental test. The y+ values obtained in the solutions were used to conclude that the $k - \omega$ turbulence model used in this simulation was accurately modelled for the overall goal of the simulation. Instability issues were found when the reaction mechanism was enabled. Fluent reported that divergence in the x-momentum equation had occurred. An error in this equation could have many root causes, as the equations in the simulation is closely linked to each other. The results obtained prior to divergence in this case displayed a large pressure in the thruster catalyst region. To remove the porous media as a source for divergence, the results obtained from the pure nozzle flow (case 1/3) was used as an initial field for the reaction case. The solution diverged in this case as well, with the same results as the previous case. The issue connected to this problem was not found.

Through these simulations it was concluded that with the setup used in this simulation it is not possible to simulate the fluid flow in a monopropellant rocket engine in ANSYS Fluent 16.2 due to stability issues connected to the Eulerian multiphase model and by enabling the heterogeneous reaction model modelled in the mixture multiphase model.

Samandrag

Hydrasin har i fleire tiår vore det mest brukte drivstoffet i monopropellant trustarar. Dette stoffet er svært giftig, og interessa for å utvikle trustarar som kan nytte seg av grønt drivstoff har difor auka kraftig dei siste åra. Det mest vanlege problemet med å utvikle desse trusterane har vist seg å vere ein optimalisert katalysator, som vert brukt for å dekomponere væskedrivstoffet til varm gass. Arbeidet som blir presentert i denne masteroppgåva vart difor gjennomført for å kunne simulere strøyminga i ein hydrogenperoksid (HP) truster med det kommersielt tilgjengelige programmet ANSYS Fluent 16.2. Ved å kunne gjennomføre denne simuleringa vil det vere mogleg å utforske strøyminga inne i katalysatoren. Dette kan legge eit godt grunnlag for vidare optimalisering utan å føre til store kostnadar knytt til omfattande testar som no er den vanlegaste metoden for optimaliseringa.

Gjennom eit djupsøk i dei forskjellige modellane som Fluent nyttar seg av, viste det seg at det burde vere mogleg å simulere dette problemet i Fluent. Sidan fasane som er inkludert i dette problemet ikkje er i likevekt, måtte dette modellerast med den komplekse Euler-fleirfasestrøymingsmodellen. Dei kjemiske stoffa vart modellert ved species modellen. Trykkfallet over katalysatoren vart modellert ved å modellere denne delen som eit porøst medium. Den kjemiske reaksjonen knytt til dekomponering av HP og fordamping av vatn. Den turbulente strøyminga i trusteren vart modellert ved $k-omega$ turbulensmodellen.

Simuleringsresultata for Euler-fleirfasemodellen konvergerte ikkje trass fleire forsøk på å stabilisere løysaren som er brukt i Fluent. Simuleringa vart difor splitta opp i tre nivå for å finne årsaka til konvergensproblema. Gjennom dette simuleringsarbeidet kom det fram at Euler-modellen ikkje klarer å handtere kompressibel strøyming. Det vart difor gjort eit forsøk på å simulere problemet med mixture fleirfasemodellen.

Resultata som vart funne med mixture modellen for rein dysestrøyming, fyrste nivå i simuleringa, vart validert og verifisert gjennom ei samanlikning med eksperimentelle resultat. Det viste seg at trykkfallet som vart utrekna i den neste simuleringa, som inkluderte porøs medium, ikkje var korrekt modellert ved samanlikning med eksperimentelle resultat. For å validere turbulensmodellen brukt i simuleringa vart y+ verdiar ved veggen av trusteren analysert. Resultata frå dette viste at mesh'et i simuleringa ikkje hadde god nok oppløysing nær veggane i trusteren. Ein kan gå ut ifrå at påverknadane dette har på dei overordna resultata er små, og mesh'et vart difor ikkje endra. Då reaksjonsmekanismen og fordampingsmodellen vart inkludert i simuleringa divergerte likninga for rørslemengd i x-retning. Årsaka til denne feilen vart ikkje funnen, men på grunn av det store trykket som resultata viste så vart den porøse sona fjerna. Ei ny simulering utan denne modellen vart utført, men likninga divergerte på same måte som tidlegare.

Gjennom dette simuleringsarbeidet vart det konkludert at oppsettet som her har vore brukt ikkje gjer det mogleg å simulere strøyminga i ein monopropellant truster i ANSYS Fluent 16.2. Dette på grunn av stabilitetsproblem knytt til den Eulerian-fleirfasemodellen og ved å inkludere reaksjon- og fordampingsmodellen i mixture fleirfasemodellen.

Contents

List of Figures

List of Tables

Nomenclature

α	Permeability of porous media
$\bar{\bar{\tau}}$	Stress tensor
β	non-Darcy coefficient
$\dfrac{1}{\alpha}$	viscous resistance coefficient
$\dot{m}_{q,p}$	Mass transfer between phases
η	Drag modification factor
$\mathbf{F}_q$	External body force
$\mathbf{F}_{lift,q}$	Lift force
$\mathbf{F}_{td,q}$	Turbulent dispersion force
$\mathbf{F}_{vm,q}$	Virtual mass force
$\mathbf{F}_{wl,q}$	Wall lubrication force
$\mathbf{q}_q$	Phase q heat flux
$\mathbf{v}_q$	Phase velocity of phase q
$\mathbf{v}_{pq}$	Interphase velocity
μ	Dynamic viscosity
$\nabla p'$	Pressure gradient in flow direction
ρ_s	Solid medium density
ρ_{pq}	Phase reference density
τ_p	Particulate relaxation time
ε	Porosity/void fraction in porous media
A_0	Pre-exponential factor
A_i	Interfacial area
A_{mesh}	Surface area of the catalyst mesh screen
$c_{p,q}$	Specific heat at constant pressure of phase q
d_p	diameter of a spherical particle of a pellet based catalyst
d_p	Bubble or droplet diameter
E_A	Activation energy
E_f	Total fluid energy
E_s	Total solid medium energy
h_q	Heat transfer coefficient of phase q

h_q	Specific enthalpy of the phase q
H_qS	Phase enthalpy of phase q
h_{pq}	Interphase enthalpy
h_{pq}	Volumetric heat transfer coefficient between phase q and p
k_1	Reaction rate constant
k_f	Fluid phase thermal conducitivity
k_q	Thermal conductivity of phase q
k_s	Solid medium thermal conductivity
k_{eff}	Effective thermal conductivity of the medium
K_{pq}	Internal phase momentum exchange coefficient
MW_i	Molecular weight
Q_{pq}	Heat exchange intensity between phase q and p
Q_{pq}	Volumetric rate of energy transfer between phases
R_i	Net rate of production of species in homogenous chemical reaction
r_{cyl}	Radius of the cylinder containing the calatys
S_f^h	Fluid enthalpy source term
S_q	Enthalpy source term, in this case the chemical reaction
T_S	Interface temperature
u'	Superficial velocity in porous media.
Y_i	Species mass fraction
HP	Hydrogen Peroxide
HTP	High Test Peroxide
MIB	Minimum impulse bit
TRL	Technology Readiness Level

Chapter 1

Introduction

1.1   Monopropellant Rocket

A monopropellant rocket utilises a single liquid as propellant, which is stored in a pressurised tank. By the feeding pipe-system and the distribution plate, the liquid is fed into the decomposition chamber, as depicted in Figure 1.1 where the catalyst is placed. The liquid is then decomposed by the catalyst into a hot gas and enters the thrust chamber where the gas is expanded through a nozzle generating thrust.
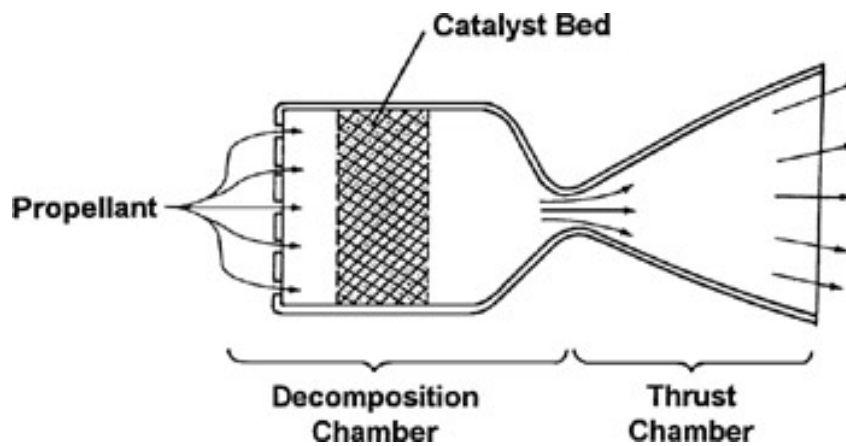
Figure 1.1. Monopropellant thruster concept [1].

These types of monopropellant thruster systems, as seen in Figure 1.2, are used in a larger launch vehicles for propellant settling and attitude control. Including the piping and tank configuration these systems culminates in a complex installation and have restrictions in terms of operating temperature and other extreme environmental factors followed by operating in space. The thruster systems are also used as a propulsion system for satellites as described in Figure 1.3.
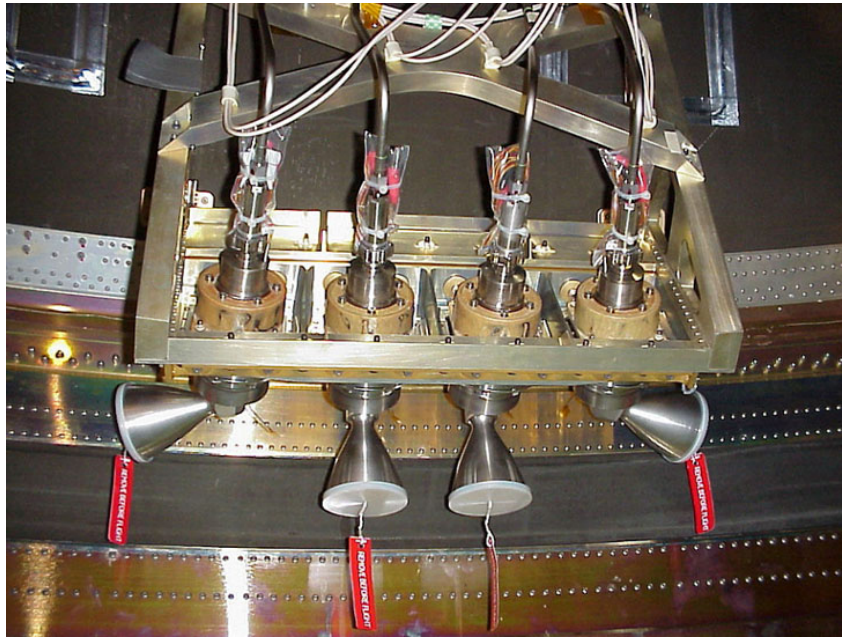
Figure 1.2. 400 N hydrazine thrusters on-board the European Space Agency (ESA) satellite launch vehicle Ariane 5 [2].
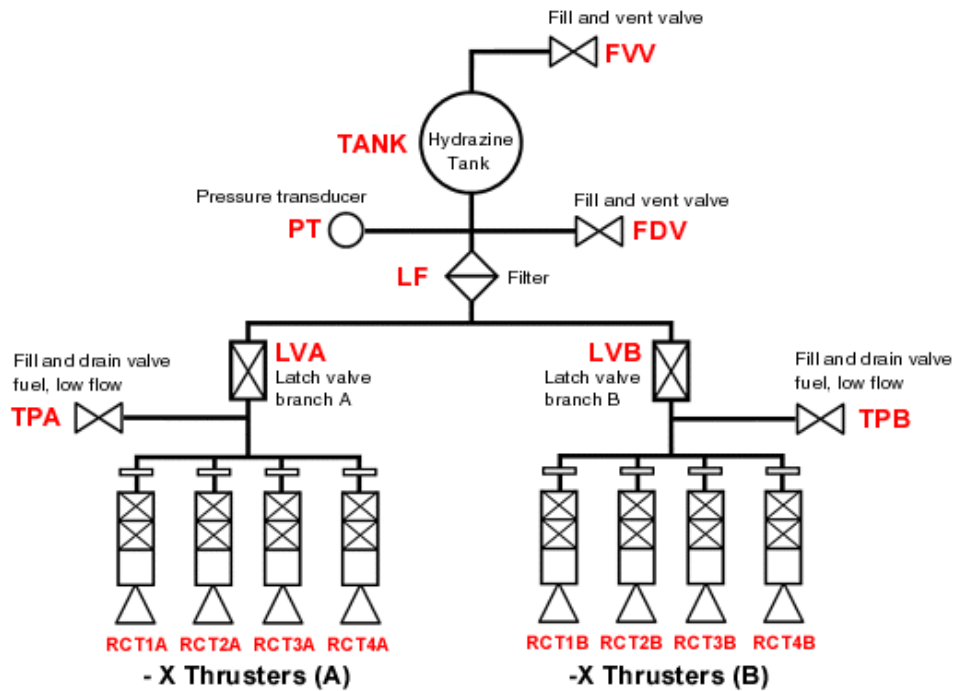
Figure 1.3. Propulsion schematics for the Gallileo satellite monopropellant thruster system [3].

Weighing in on a range between 0.5 to 3 kilograms, these thrusters are very small in size compared to the main engines on the launch vehicle. The thrusters can deliver more then 200 N of thrust with high precision. They must be able to operated in steady state as well as in a pulsing mode, depending on the launch or satellite mission. The performance of a thruster is measured by its thrust level, start time, shutdown time, minimum impulse bit (MIB) and the delay between the centroid of the on command until the centroid time of the obtained thrust, as described in Figure 1.4 [4]. The start time is defined by the time it takes from the on command is sent and the valves open up and until 90% of thrust is obtained. The shut down time is defined as the time between the cessation of the on command and the final decay in thrust. The MIB is a measure of the minimum altitude change that can be commanded to the system.
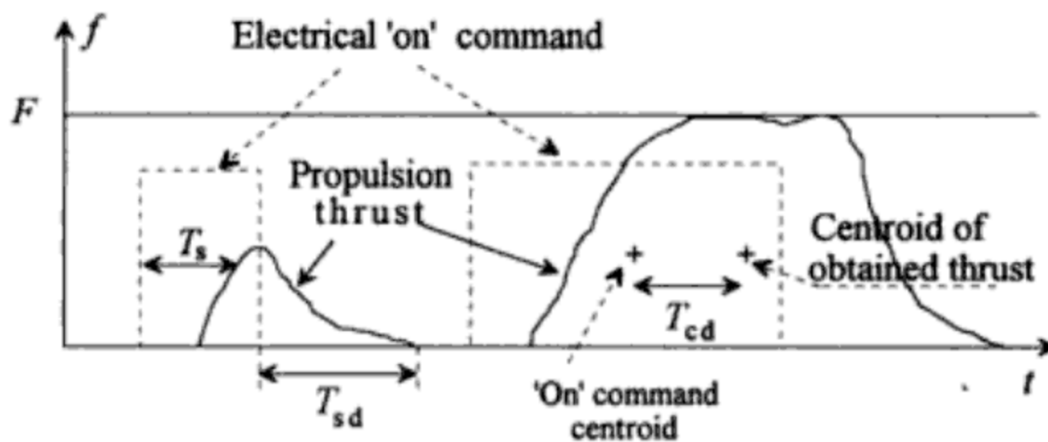
Figure 1.4. Time-domain of truster pulse [4].

Dependent upon the thruster specifications these performance measures are usually found to be in the range of milliseconds to a few seconds. With these performance criterion it follows that careful design, reliability and precision are extremely important factors of these thruster systems.

1.2 Green Propellants

Currently, the most commonly used liquid monopropellant is hydrazine. Due to its carcinogenic nature, hydrazine was added to the European Chemicals Agency list of substances of very high concern in 2011 [12]. Making it to this list is the first step in the process of making all use of this substance in the European Union a subject of authorisation under the REACH (Registration, Evaluation, Authorisation and Restriction of Chemicals) [13] regulation. In addition to this listing, the toxic nature increases the overall costs of a hydrazine system due to the necessary precautions needed during the operation and handling of the fluid.

The interest of replacing hydrazine with a green propellant, with no or negligible toxic or carcinogenic risk, has therefore increased to a large extent over the last decade. Several different viable green propellant options exists, such as nitrous oxide, aqueous ammonium dinitrate (ADN), aqueous hydroxyl ammonium nitrate (HAN) and hydrogen peroxide.

Due to the new interest in these propellants, as well as the development of stable solutions of ADN and HAN are still under development, the literature on the performance of these propellant solutions is sparse.

1.2.1 Nitrous Oxide

Nitrous oxide, also known as dinitrogen monoxide or laughing gas, with the chemical formula N_2O. With its high vapour pressure, nitrous oxide allows the thruster system to be self-pressurized. This would simplify the overall system, as a separate pressure feeding system is not necessary. That being said, a N_2O self pressurizing system only benefits the overall performance on a small scaled configuration, as higher pressure is needed for an optimal blowdown in larger systems.

N_2O has a higher specific impulse, 206 s, than hydrogen peroxide, 180 s, [14] but with its low density the overall gain would be lost as the system would in turn have to be heavier and include more mass than with hydrogen peroxide. N_2O has largely been overlooked as a viable propellant due to the difficulty of maintaining reproducible catalytic decomposition. In addition, a $N2O$ system requires pre-heating of the catalyst in order to fully decompose and obtain maximum thrust.

1.2.2 Ammonium Dinitrate

Ammonium dinitrate (ADN) is a high-energy inorganic salt, mainly intended as oxidizer in solid rocket propellants. The catalytic decomposition of ADN is by far not well documented and has not been achieved at room temperature. In general, preheating of the catalyst to at least 150 degrees is required in order to ensure catalytic decomposition [15]. Further development is therefore required for ADN to become a fully viable option to replace hydrazine, which will be both cost- and time-consuming.

1.2.3 Hydroxyl Ammounium Nitrate

Hydroxyl ammonium nitrate (HAN), with the chemical formula NH_3OHNO_3, is a nitrate salt of hydroxylamine and is soluble in water. HAN is a relatively new synthetic energetic chemical. Due to the fact that it has been newly discovered, this propellant has very limited flight heritage. HAN monopropellants have demonstrated and delivered specific impulse of 270 s in laboratory engines [16].

With a current launch year of 2017, NASAs Green Propellant Infusion Mission (GPIM) intends to perform a technology demonstation mission of a HAN fuel/oxidiser blend on a satellite in orbit [17]. According to the developers behind this thruster the experimental results of their developed HAN solution has displayed a 50% higher performance than hydrazine.

1.2.4 Hydrogen Peroxide

Another alternative to hydrazine is hydrogen peroxide, H_2O_2. At a concentration between 70-98% hydrogen peroxide is known as high test peroxide (HTP) [18]. HTP has a larger amount of flight heritage than any of the other alternatives. It has been used on the Russion Souyz Rockets to drive the turbopump feeding the main engines. The British rocket, Black Arrow, also used hydrogen peroxide as propellant [18]. Most of the research found on this propellant is linked to the 1960's, before hydrazine with its improved performance compared to HTP entered the market. The overall decomposition process of HP can be described as follows

$$H_2O_2 \rightarrow H_2O + \frac{1}{2}O_2 \tag{1.2.1}$$

which makes it a "green" propellant as the products are water and oxygen gas. As hydrazine has dominated the market for decades, the technological readiness level (TRL) for HP systems is fairly low and a lot of research is still to be done in order to increase HTP system market share. One of the main advantages of HTP is that there are fewer precautions to be made during production and handling of the liquid, which will drive the launch costs down compared to a hydrazine based system. The specific impulse of HTP does not reach the same level as hydrazine [19], but looking at the density specific impulse HTP is a very good candidate for developing a compact system.

HP is currently produced almost exclusively by the anthraquinone oxidation process [20]. After this process, all impurities in the solution must be removed due to the decomposition abilities of HTP. As the formation of water is more favourable than hydrogen peroxide, the final solution consists of both HP and water. Through distillation one is able to increase the concentration of HTP.

With more flight heritage than any of the other alternatives, in addition to its high density impulse and increased availability, hydrogen peroxide is a very promising replacement of hydrazine for monopropellant thrusters. This report will therefore consider a HTP thruster operating with a HTP concentration of 87.5%.

1.3 Catalyst

The decomposition process of HTP is a favourable process, which means that decomposition occurs at all time where the rate of decomposition is dependent on temperature. If HP comes in contact with another substance that may function as a catalyst, the rate of decomposition can increase dramatically and have severe consequences. A catalyst is a material which itself is not consumed in the decomposition process. It functions merely as a booster and increases the rate of decomposition by reducing the activation energy. The activation energy is the minimum amount of energy required to convert a stable molecule into a reactive molecule.

There are many types of catalysts that may be used along with HP, whereas silver screens, various liquid permanganates, solid manganese dioxide, platinum and iron oxide

are widely used in both industrial processes and in rocket engines [18]. According to Batonneau et. al [15], pellet-based catalysts for HTP have a significantly lower pressure drop than the other althernatives. However, the pellet based catalyst were observed to be more prone to pressure oscillations at high flow rates. This thesis will therefore consider a catalyst screen structure as seen in Figure 1.5.
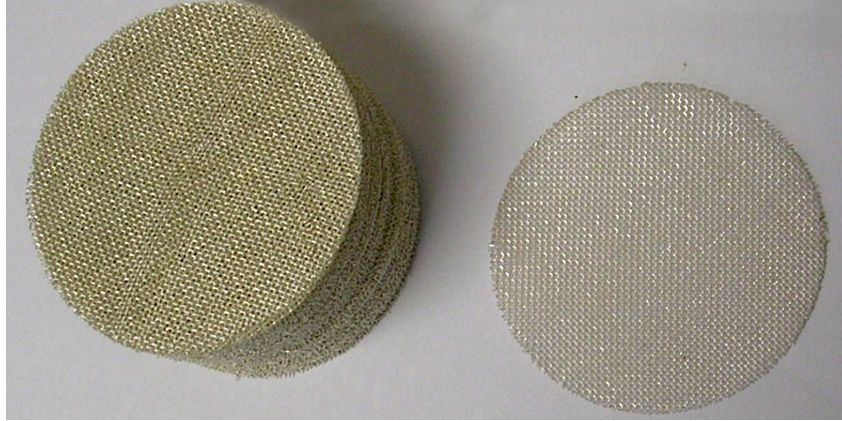
Figure 1.5. Monopropellant mesh screen catalyst [5].

1.4 Distribution Plate

In order to maximise the decomposition of HTP, an important parameter is the contact area between the solid catalyst and the liquid. The flow must therefore be properly distributed upon injection into the catalyst, as seen in Figure 1.1. In this report the inlet flow to the catalyst will be considered to be evenly distributed.

1.5 CFD Simulations of Rocket Engines

The most common way of developing and optimising a thruster, or other types of rocket engines, has been through extensive testing. These tests are very expensive and more importantly, even though the engine is packed with different sensors to collect data, you cannot see what is happening inside the engine as it runs. By utilising CFD it is possible to simulate and optimize the design before the test sequence starts, and the remaining tests would the be used to fine-tune the system even further.

For years, commercial CFD software has been used to optimise combustion engines in cars. The chemical process and fluid flow in car engines are complex, but not as complex as in a rocket engine.

One of the major difficulties are linked to the varieties of time scales of the simulation, as seen in Figure 1.6. The chemical reactions in a rocket engine take place at between 10^{-11} and 10^{-9} seconds, depending on the complexity of the reaction [6]. The advection, the mechanism describing the bulk fluid motion, occurs between 10^{-7} and 10^{-6} seconds. The chamber residence, when the fuel is burning and being ejected by the engine, and the acoustical vibrations occur at 10^{-4} and 10^{-3} seconds. The time scale that a CFD

simulation of a rocket engine has to cover is therefore very broad. Furthermore, the physical sizes are also an issue that needs to be considered. At the one extreme, the combustion chamber of larger rocket motors are around 1 meter and at the other end we find the Kolmogorov scale, at one micrometer, which controls the rate of viscous dissipation in a turbulent fluid and determines the rate of combustion in the rocket engine.
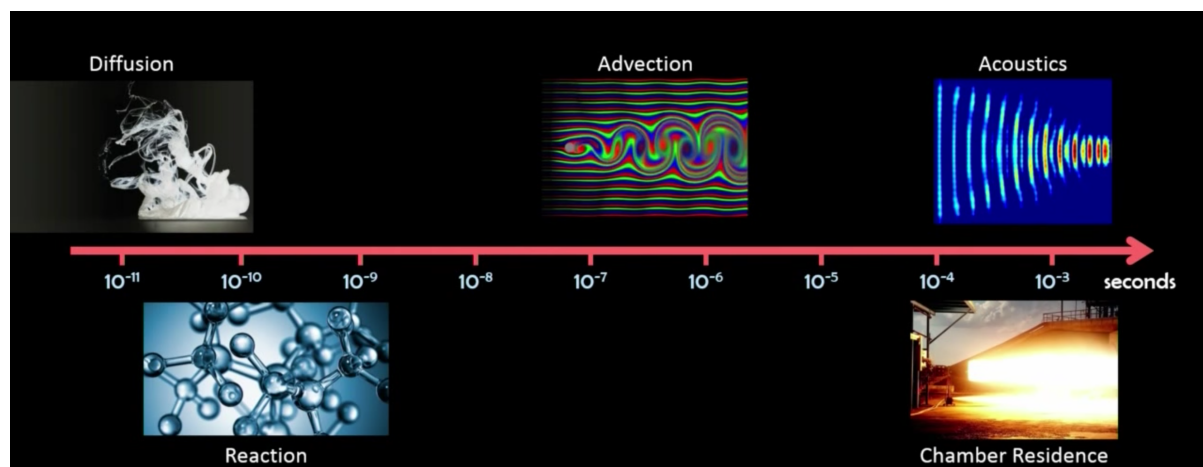
Figure 1.6. The different time scales present in the combustion process of a rocket engine [6].

Companies working on large scale rocket engines have therefore not been utilising commercial CFD software, but developed in-house technology and software to be able to meet the criterion of these flows. Despite the development of an optimised software, the calculations are still computationally expensive. As presented during the 2015 GPU Technology Conference, new developments are being done in this field by the propulsion team in SpaceX by the utilisation GPU acceleration. A lot of resources and large costs are connected to these types of developments and the details and availability of these software are therefore extremely limited outside of the company that has developed the software.

1.6   Problem Description

As described earlier, the fluid flow in a monopropellant rocket does not include combustion, but a chemical reaction. With an increasing interest and research being done on HTP it is of great importance to be able to model the fluid flow inside the thruster. The most common issue met in the development of monopropellant thrusters have been seen through literature to be an optimised catalyst. As this problem may not be, to such a large extent, bound by the same issues as described in section 1.5 it has therefore been of high interest to investigate if it is possible to simulate this type of fluid flow with a commercially available CFD software. With this possibility, the industry as well as academia would be able to perform further research on both catalytic behaviour and rocket engine performance as the utilisation of more specialized CFD software is limited to their respective developers.

The problem of describing this flow is of a complex nature, involving several different complex models which in turn are linked to each oter. Crude simplifications could be made to the problem in order to decrease the complexity. However, this would result in a loss in physics. The consequences of these losses have not been possible to quanitfy, due to the complexity of the interaction of all the different models.

In this report, the problem description has been simplified to a state which the losses in physics have been considered minimal. The different models, their derivation and assumptions will be described to an extent that makes it clear why they have been selected as adequate to describe the given phenomena. The complete physical description of all models will not be described as that is beyond the scope of this thesis. The goal of this thesis is to describe a method of simulating the steady state fluid flow of the thruster in the commercially available CFD software ANSYS Fluent 16.2 Academic version, and the simulation would thereby consist of:

- Multiphase flow
- Multicomponent flow
- Reaction mechanics of decomposition
- Mass transfer by decomposition and evaporation
- Turbulent flow
- Compressible flow
- Catalyst pressure drop
- Heat transfer

The CFD model should thereby be able to simulate, as depicted in Figure 1.7, water and liquid hydrogen peroxide entering into a catalyst, modelled as a porous region, where the hydrogen peroxide decompose into water vapour and oxygen gas. The gas will then be expelled through a nozzle and generate the desired thrust level of 200 N.
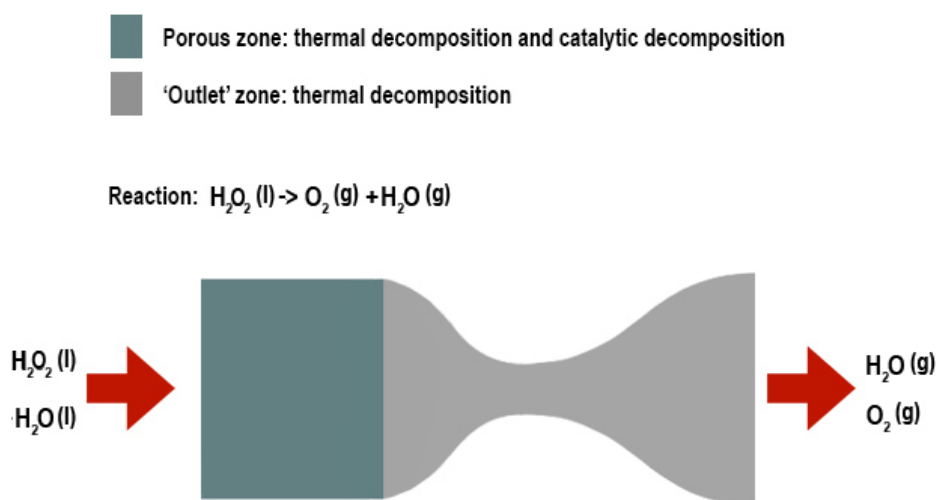
Figure 1.7. Problem description of thermal and catalytic decomposition of hydrogen peroxide.

Chapter 2

Theoretical Background

2.1 Decomposition of Hydrogen Peroxide

Hydrogen peroxide decomposition is a favourable process, which means that it occurs at all time, as a thermal reaction or as a catalytic process. The overall reaction equation for decomposition of hydrogen peroxide can be written as

$$H_2O_2 \xrightarrow{k1} H_2O + \frac{1}{2}O_2, \tag{2.1.1}$$

where k_1 is the global reaction rate constant, with units of s^{-1}, and is expressed by means of a reaction equation

$$\frac{d[H_2O_2]}{dt} = k_1[H_2O_2]. \tag{2.1.2}$$

The reaction rate constant is dependent upon temperature and is generally given by the Arrhenius expression [21]

$$k_1 = A_0 \exp\left(\frac{-E_A}{R_cT}\right), \tag{2.1.3}$$

where the constant A_0 is the pre-exponential factor, or frequency factor, which strictly is not constant but dependent on collision theory [21]. In simpler terms, this factor describes how often the molecular collisions occur, which leads to the splitting of the molecules to form the products.

E_A is the activation energy, which is the minimum required energy that is necessary for the decomposition to occur. The exponential term can then be interpreted as the fraction of collisions that has a relative kinetic energy larger than the activation energy E_A and will thereby take part in a catalytic reaction.

As the decomposition occurs in two different manners, thermal or catalytic, the Arrhenius constants connected to the different reactions will be different. These constants, A_0 and E_A, must therefore be found for both cases specifically for hydrogen peroxide in order to simulate the decomposition process.

2.1.1 Thermal Decomposition

The thermal decomposition of HP is generally accepted to be a first order reaction [22]. From the overall reaction Equation 2.1.1 it is clear that the reaction cannot occur in one elementary step and be a first order reaction at the same time. If it was an elementary reaction the resulting reaction rate constant would be $k = [H_2O_2]^2$, as there would be two HP molecules colliding at the same time. The relation is thereby not linear and the reaction is therefore non-elementary [23].

Given that the reaction is in fact first order, despite being non-elementary, several intermediate radical species must be involved in the decomposition process. This means that the decomposition mechanism must consists of several additional reaction steps, which finally lead up to the final products of oxygen gas and water vapour. When it comes to HTP, a generally supported complete mechanism of the thermal decomposition has so far not been reported. An investigation into the different general models, which can be used to model non-elementary reactions, was therefore performed to evaluate whether or not they could be utilised in Fluent.

One of these models was introduced in the 1920s; the Lindemann-Hinshelwood theory [24]. The reaction consists of two steps; an activation step where the molecule, H_2O_2, collides with another molecule M and is consequently brought into an activated state and decomposes into its product. The limitations of this model is that it does not take into account the structure of and the energy distribution within the molecule. Neither does it account for all the intermediate products which are formed and consumed, and the model is therefore not well suited for this problem [22].

A more extended model, known as Rice-Ramsperger-Kassel-Markus (RRKM) theory, or the transition theory, has been developed and result in reaction rates which are, in general, in closer agreement with experimental data [24]. The RRKM theory is based on quantum mechanics, and despite the large increase in available computational power, large scale simulations have not been possible to model [22].

As the currently developed methods to model the complete decomposition process are not fit for a CFD implementation, the Arrhenius parameters for the overall reaction must be determined experimentally. Koopmans [22] performed an extensive literature search on the published experiments for HTP. The most adequate constants for the gas phase were found in [25] where the values were an average of other values found in literature by other researchers [26]. The values for the liquid phase have not been extensively evaluated according to Koomans. The values listed in Table 2.1 were found by Takagi and Ishigure [27] which were evaluated for a pressure range up to 4 MPa.

Table 2.1. Arrhenius parameters for thermal decomposition.

Phase	A_0 [s^{-1}]	E_A [kJ/mol]
Liquid	$1 \cdot 10^{5.8}$	71
Gas	$1 \cdot 10^{15}$	200

2.1.2 Catalytic Decomposition

A catalytic decomposition process can be subdivided into 7 steps [7] as depicted in Figure 2.1:

1. External diffusion - diffusion of the reactant from the bulk liquid or gas phase through the boundary layer to the outside of the catalyst material.

2. Internal diffusion - diffusion of the reactant from the outside material into the catalyst material

3. Adsorption

4. Actual decomposition

5. Desorption

6. Internal diffusion - diffusion of the products from the catalyst material to the outside

7. External diffusion - diffusion of the product through the boundary layer to the bulk liquid or gas phase
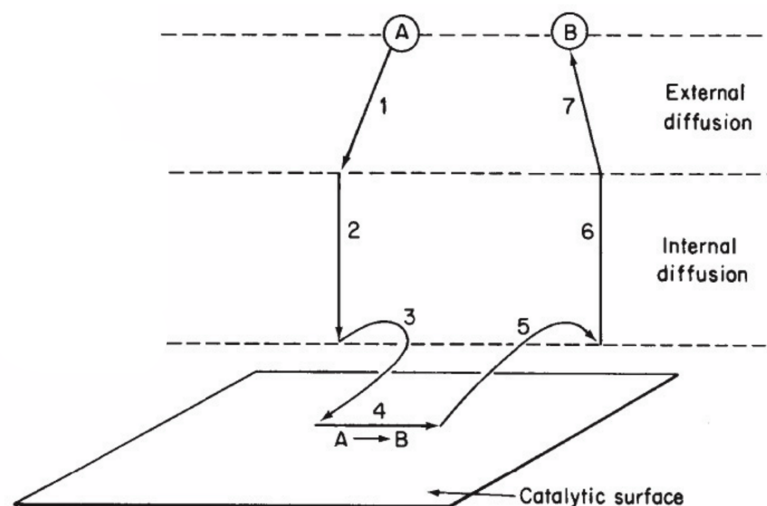
Figure 2.1. Steps in a heterogeneous catalytic reaction [7].

According to Turns [21], adsorption is the process where a molecule is held at the solid surface. This can be done in two ways: by Van der Waals bonds, which is referred to as physisorption or it can make a strong chemical bond, which is referred to as chemisorption. Chemisorption is required for catalysis and can be preceded by physisorption. The sites at the catalyst that promote reaction are known as active sites. At the active site the adsorbed molecules decompose to form reaction products. For an arbitrary molecule of particles A this process can be described by

$$A + site \underset{k_{ad}}{\overset{k_{de}}{\rightleftharpoons}} A - site \xrightarrow{k_{rec}} products. \tag{2.1.4}$$
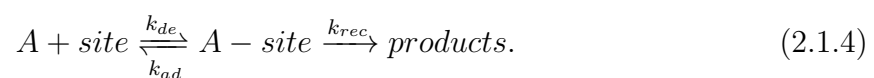
where k_{ad} and k_{de} are the adsorption and desorption constant respectively and k_{reac} the reaction rate constant for the decomposition.

When HP is consumed during the decomposition process, the concentration of HP is consequently lower at the catalyst surface compared to the bulk fluid. The overall decomposition rate is governed by the slowest process in the steps mentioned above, being either diffusion through the boundary layer or the decomposition at the catalyst. Diffusion is defined as the spontanous intermingling or mixing of atoms or molecules by random thermal motion [8]. The molar flux consists of two contributions, molecular diffusion flux relative to the bulk fluid produced by a concentration gradient and the flux resulting from the bulk motion of the fluid. At the surface, a small boundary layer δ will form due to the concentration gradient between the surface and the bulk fluid as seen in Figure 2.2.
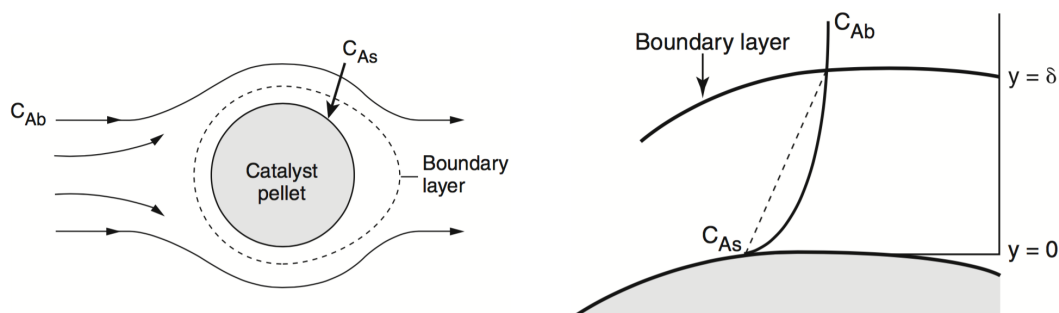
Figure 2.2. Boundary layer around a catalyst pellet with the described concentration of substance A profile from the surface C_{As} till the boundarylayer limit C_{Ab} [8].

In a diffusion limited reaction, the amount of mass transfer in and out of the boundary layer is thereby limiting the overall reaction rate [8]. According to Koopmans [22], research performed by Holub et. al. [28] concluded that due to the tortuous flow in the catalyst, consisting of twists and turns, the formation of a velocity and diffusion boundary layer is prevented. In addition, according to research performed by Oehmichen et. al [29] the decomposition process is reaction limited when the concentration of HP exceeds 30%. This conclusion was related to the research performed on the influence of bubble formation in the catalytic process. The experimental results argued that the bubble formation was the origin of this dependence. Koopmans [22] elaborated on this dependency by considering that the volume of the reaction products are more than 62 times the volume of the liquid peroxide that is decomposed. 99% of this volume increase can be attributed to the formation of oxygen bubbles emerging from the catalyst surface. Once the bubble is detached from the surface the gap is filled with liquid once again, this process enhances mixing, resulting in a reduced difference in peroxide concentration between the catalyst surface and the bulk fluid. With a reduced concentration gradient, the diffusion boundary layer would not form.

Furthermore, a diffusion limited reaction becomes reaction limited when the velocity of the bulk fluid is increased or the diameter is decreased[8]. The relation for this is given in Figure 2.3. This effect is caused by the decreased thickness of the boundary layer as the velocity increases or the diameter decreaeses. With the given case dimensions, the catalyst mesh thread diameter and massflow measurements found in experiments, in addition to the above stated arguments, the catalytic reaction of hydrogen peroxide is considered to be reaction rate limited. With this conclusion the boundary layer around the mesh threads does not have to be considered in the simulation.
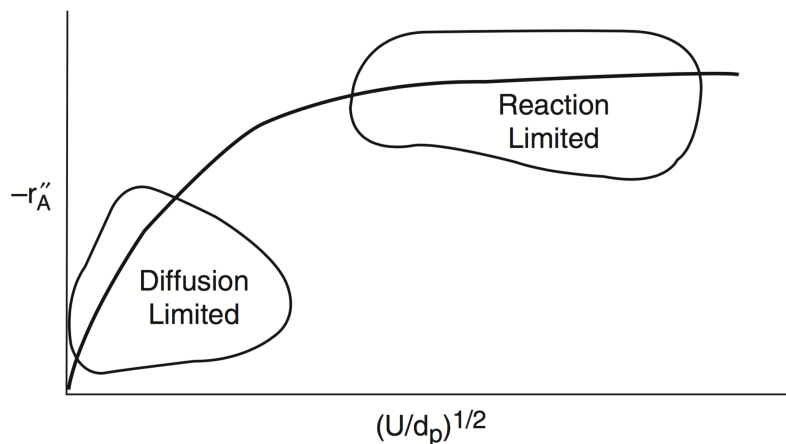
Figure 2.3. Plot of the region where a reaction is regarded as diffusion limitied, as a result from the reaction rate and droplet size [8].

When it comes to the catalytic decomposition of HP vapour, little research has been performed on this field according to Koopmans [22]. The process mentioned above is not present in the gas phase but the underdevelopment of the boundary layer due to the tortuousity still holds and Koopmans therefore assumed that external diffusion can be neglected.

Several models for HP catalytic decomposition have been developed. According to Giamello et. al [30] 'almost every conceivable mechanism for the catalytic decomposition of hydrogen peroxide has been proposed' and a thorough description is far from being accomplished.

For modeling purposes it will be assumed that the decomposition mechanism can be described accurately enough by a single step where HP is directly converted into its products. According to [22] this approach is often taken by researchers in the field of hydrogen peroxide based rocket motors [[31], [32], [33], [34]]. Values found in literature by Koompans [22] are listed in Table 2.2.

Table 2.2. Arrhenius parameters for catalytic decomposition.

Phase	$\mathbf{A}_0$ [ms^{-1}]	$\mathbf{E}_A$ [kJ/mol]
Liquid	$2.6{\cdot}10^4$	52.5
Gas	$1{\cdot}10^1$	41.8

2.2 Convergent Divergent Nozzle

In a convergent divergent nozzle, the flow can transition to a supersonic flow with a Mach number larger than 1. This occurs when the nozzle is choked, where the maximum mass flow is obtained in the throat area and the Mach number is larger than 1 [9], as seen in Figure 2.4.
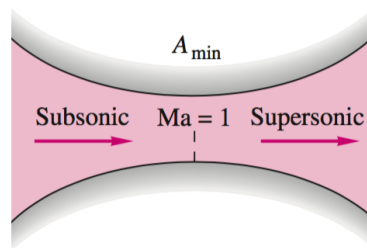
Figure 2.4. Flow through a convergent divergent nozzle where the flow is accelerated smoothly from subsonic to supersonic [9].

The properties of the flow changes in a different manner when it is supersonic compared to a subsonic [9]. The pressure decreases when the area is increased and the velocity increases as seen in Figure 2.5.

Figure 2.5. Effects of supersonic and subsonic flow on property changes with changes in area in a duct [9].

The difference between back pressure and the stagnation pressure of the fluid flow determines the pressure distributions inside and outside of the convergent divergent nozzle. In Figure 2.6, the different distributions are depicted for isentropic flow.
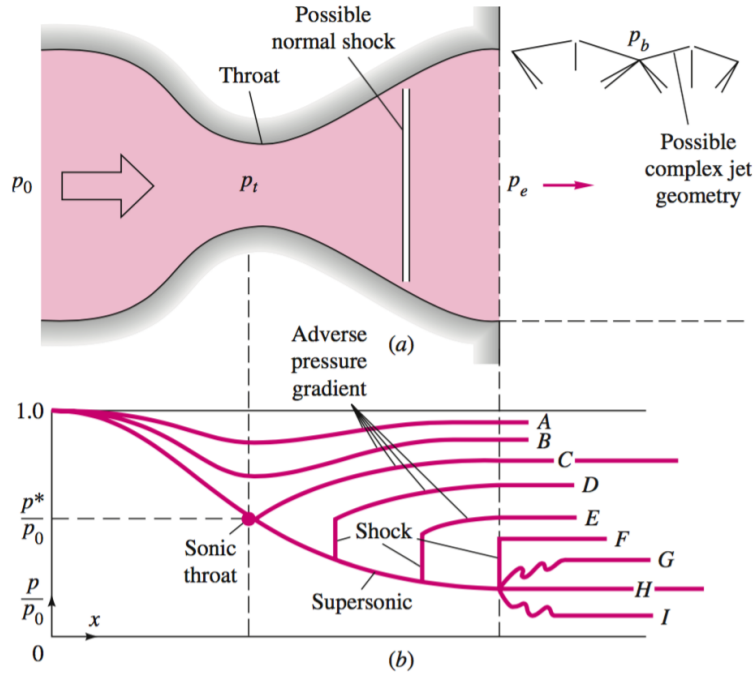
Figure 2.6. Operation of a converging–diverging nozzle: (a) nozzle geometry with possible flow configurations; (b) pressure distribution caused by various back pressures [9].

In case A and B, as seen in Figure 2.6, the flow is subsonic throughout the nozzle as the nozzle has not been choked. In case C the nozzle is choked but supersonic flow is not achieved in the divergent section [9]. For case D to I the flow after the throat is supersonic. In case D and E a normal shock inside the nozzle occurs to ensure fulfillment of $p_e = p_b$ at the exit. In case F the normal shock occurs at the exit. The design condition is shown in case H, where $p_e = p_b$ and no shock is present.

Chapter 3

ANSYS Fluent Models

In order to meet the requirements of simulating the fluid flow in the thruster as described in section 1.6, a careful consideration of the different models to be implemented in Fluent had to be made. The following sections describe the different models used and how they are implemented in Fluent.

3.1 Multiphase Model

A complete description of the multiphase interactions and behaviour for the given problem is of a complex nature. The presence of the surface and the turbulence between two phases or components in the flow introduces great difficulties in the mathematical and physical formulation of the problem. It is therefore necessary to describe the characteristics of the local flow in order to derive the field and constitutive equations. From that local flow, the macroscopic properties can be obtained with an appropriate averaging procedure [35].

According to Ishii and Hibiki [35] the different averaging procedures can be classified into three main groups:

- *Eulerian averaging*: considers the average quantities of each phase represented as a given volume fraction within the selected control volume. The interactions between the phases are dealt with by means of source and sink terms in the conservation equations.

- *Lagrangian averaging*: describes the behaviour of a single particle or a number of individual particles.

- *Boltzmann statistical averaging*: describes a group of particles that are clustered together and includes the dynamic features between them by a collision model.

In Fluent [36] it is possible to model dispersed flow with the Euler-Lagrange and Euler-Euler method. With the goal of modelling the complete field of the flow, the Euler-Euler method is most well suited for that purpose. The available Euler-Euler methods in Fluent consist of two different models; the mixture model and the Eulerian model.

3.1.1 Mixture Model

The mixture model approximation of multiphase flow assumes a local equilibrium between the phases over short spatial length scales and is a good alternative to the complex Eulerian method. The equations being solved in the mixture model are therefore defined in a simpler form than for the Eulerian model; the momentum, continuity and energy

equations are solved for the mixture and the volume fraction equations are solved for the secondary phases [37].

Through the utilisation of slip velocity, the model makes it possible to describe fluid flow where the phases move at different velocities, which is not the case in the standard description of a mixture model whereas the mixture velocity is a property of the average flow [35]. The model assumes a strong coupling between the phases and is especially useful in cases where the inter-phase laws are unknown[37].

According to Koopmans [22] the phases in a H_2O_2 catalyst will generally not be in a state of equilibrium. The reason for this conclusion was based on the significant temperature difference between both phases, whereas H_2O_2 87.5%wt has an expected gas temperature just below 700 °C while in liquid the temperature is typically hundred degrees lower. In addition to this issue, the density difference between the phases are of 2 to 3 orders of magnitude. These differences gives way to state that there is no mechanical equilibrium either. Performing the simulation with the mixture model was therefore considered not to be adequate as it would introduce a loss in physics deemed important for this case.

3.1.2 Eulerian Model

The Eulerian model is the most complex multiphase model available in Fluent [36]. The number of allowed phases are only limited by memory requirements. The model considers volume fractions, which represent the space occupied by each phase, and the laws of conservation of mass and momentum are satisfied by each phase individually. Heat exchange between the phases are accounted for as a function of temperature difference.

The main assumption of the model is that a single pressure is shared by all phases. The turbulence models $k - \epsilon$ and $k - \omega$ are available and may be applied to all phases or the mixture. Periodic flow is not allowed in the Eulerian model in Fluent, which would thereby prohibit the simulation of a thruster in a pulse mode firing. Simulating the thruster in this state is beyond the scope of this thesis and this model was therefore considered to be the best fit despite its complexity, something of which would contribute to a less computationally stable model.

3.2 Species Model

In order to resolve the aspect of the multicomponent fluid flow, where a given phase consists of a mixture of different fluids, the species model must be included in the simulation. In Fluent, the species equation is solved for each phase k, and predicts the mass fraction of each species, Y_i^k, through the solution of a convection-diffusion equation for the ith species, and is given by

$$\frac{\partial}{\partial t} \left(\rho^q \alpha^q Y_i^q \right) + \nabla \cdot \left(\rho^q \alpha^q \mathbf{v}^q Y_i^q \right) = -\nabla \cdot \alpha^q \mathbf{J}_I^q + \alpha^q S_i^q + \sum_{p=1}^{n} \left(\dot{m}_{pi,qj} - \dot{m}_{qj,pi} \right) + Rate. \quad (3.2.1)$$

In this equation R_i^q is the net rate of production of species in a homogeneous chemical reaction for phase q, $\dot{m}_{qi,pi}$ is the mass transfer source between species i and j from phase q and p, and $Rate$ is the heterogeneous reaction rate. In addition, α^q is the volume fraction for phase q and S_i^q is the rate of creation by addition from the dispersed phase, i.e. evaporation.

3.3 Conservation of Energy

In Fluent 16.2 the conservation of energy in the Eulerian multiphase model is solved for each phase by

$$\frac{\partial}{\partial t}\left(\alpha_q \rho_q h_q\right) + \nabla \cdot \left(\alpha_q \rho_q \mathbf{u}_q h_q\right) = \alpha_q \frac{p_q}{\partial t} + \bar{\bar{\tau}}_q : \nabla \mathbf{u}_q - \nabla \cdot \mathbf{q}_q + S_q + \sum_{p=1}^{n}\left(Q_{pq} + \dot{m}_{pq} h_{pq} - \dot{m}_{qp} h_{qp}\right) \tag{3.3.1}$$

where h_q is the specific enthalpy of the qth phase, $\mathbf{q}_q$ is the heat flux, Q_{pq} is the intensity of heat exchange between the pth and qth phases, and h_{pq} is the interphase enthalpy. S_q is a source term that includes sources of enthalpy, in this case the chemical reaction. The S_q term that includes the source of energy due to chemical reaction $S_{q,rxn}$ is given by

$$S_{q,rxn} = -\sum_j \frac{h_j^0}{M_j} R_j \tag{3.3.2}$$

where h_j^0 is the enthalpy of formation of species j and R_j is the volumetric rate of creation of species j.

3.4 Volume Fraction and Continuity Equation

In a multiphase simulation the concept of phasic volume fractions, α_q, is introduced to represent the space occupied by each phase. The volume of phase q, V_q, is defined in Fluent by [36]

$$V_q = \int_V \alpha \, dV, \tag{3.4.1}$$

where

$$\sum_{q=1}^{n} \alpha_q = 1. \tag{3.4.2}$$

The effective density of phase q is given by

$$\hat{\rho}_q = \alpha_q \rho_q \tag{3.4.3}$$

where ρ_q is the physical density of phase q. The volume fraction can be solved either through implicit or explicit time discretisation.

The volume fraction for each phase is calculated from the continuity equation [36]

$$\frac{1}{\rho_{rq}} \left(\frac{\partial}{\partial t} \left(\alpha_q \rho_q \right) + \nabla \cdot \left(\alpha_q \rho_q \mathbf{v}_q \right) = \sum_{p=1}^{n} \left(\dot{m}_{pq} - \dot{m}_{qp} \right) \right) \qquad (3.4.4)$$

where ρ_{rq} is the phase reference density, or the volume average density of the qth phase in the solution domain. The solution to this equation for each secondary phase, along with the condition that the volume fraction sum to one, allows for the calculation of the primary phase volume fraction.

3.5 Interfacial Area Concentration

The interfacial area concentration is defined as the interfacial area between two phases per unit mixture volume. This is an important parameter for predicting mass, momentum and energy transfer through the interface between the phases.

With the Eulerian multiphase model, this interface area can be calculated using a transport equation or an algebraic relationship between a specific bubble diameter and the interfacial area concentration.

The different algebraic models available in Fluent are the particle model, which is used for dispersed fluid flow, the Ishii model, used for boiling flow only and the symmetric model. By the nature of the fluid flow in the thruster, the symmetric model was therefore selected.

The symmetric model introduces the complementary volume fraction (corresponding to the primary phase volume fraction for a two-phase flow) which ensures that the interfacial area concentration approaches 0 as α_p approaches 1.

$$A_i = \frac{6\alpha_p(1 - \alpha_p)}{d_p} \qquad (3.5.1)$$

where d_p is the bubble or droplet diameter.

3.6 Momentum Equation

The fluid-fluid conservation of momentum equation solved in the eulerian multiphase model by ANSYS Fluent 16.2 is given by [36]

$$\frac{\partial}{\partial t} \left(\alpha_q \rho_q \mathbf{v}_q \right) + \nabla \cdot \left(\alpha_q \rho_q \mathbf{v}_q \mathbf{v}_q \right) = - \alpha_q \nabla p + \nabla \cdot \bar{\bar{\tau}}_q + \alpha_q \rho_q \mathbf{g}$$

$$+ \sum_{p=1}^{n} \left(K_{pq} \left(\mathbf{v}_p - \mathbf{v}_q \right) + \dot{m}_{pq} \mathbf{v}_{pq} - \dot{m}_{qp} \mathbf{v}_{qp} \right) \qquad (3.6.1)$$

$$+ \left(\mathbf{F}_q + \mathbf{F}_{lift,q} + \mathbf{F}_{wl,q} + \mathbf{F}_{vm,q} + \mathbf{F}_{td,q} \right),$$

where $\mathbf{F}_q$ is an external body force, $\mathbf{F}_{lift,q}$ is a lift force, $\mathbf{F}_{wl,q}$ is a wall lubrication force, $\mathbf{F}_{vm,q}$ is a virtual mass force, and $\mathbf{F}_{td,q}$ is a turbulent dispersion force. $\mathbf{v}_q$ and $\mathbf{v}_p$ are the phase velocities. $\dot{m}_{qp}$ characterizes the mass transfer from phase q to p, $\mathbf{g}$ is the acceleration due to gravity and $\bar{\bar{\tau}}$ is the stress tensor, which is calculated through the applied turbulence model. $\mathbf{v}$ is the interphase velocity. This velocity is equal to the phase velocity of the phase that mass is transferred to, i.e. if $\dot{m}_{pq} < 0$ mass is transferred from phase q to p $\mathbf{v}_{pq} = \mathbf{v}_q$. K_{pq} is the internal phase momentum exchange coefficient.

For fluid-fluid flows, each secondary phase is assumed to form droplets or bubbles and the exchange coefficient for these types of bubbly, liquid-liquid or gas-liquid, mixtures is defined as

$$K_{pq} = \frac{\rho_p f}{6\tau_p} d_p A_i \qquad (3.6.2)$$

where A_i is the interfacial area described in section 3.5, f is the drag function, which is defined differently for the different exchange-coefficient models, and τ_p is the particulate relaxation time defined as

$$\tau_p = \frac{\rho_p d_p^2}{18\mu_q} \qquad (3.6.3)$$

3.6.1 Drag Function

The drag function, f, is used to calculate the momentum exchange coefficients between the different phases. The model includes a drag coefficient, C_D, that is based on the relative Reynolds number. In order to ensure that K_{pq}, defined in Equation 3.6.2, tends to zero whenever the primary phase is not present within the domain the drag function is always multiplied by the volume fraction of the primary phase q. the different drag models available in Fluent are [36]:

- Schiller and Neumann Model
  This model is the default model, and is acceptable for general use for all fluid-fluid pairs of phases.

- Morsi and Alexander Model
  This is the most complete model, which adjusts the function definition frequently over a large range of Reynolds numbers, but calculations with this model may be less stable than with the other models.

- Symmetric Model
  This model is recommended for flows where a secondary (dispersed) phase becomes the primary (continuous) phase in another. This model can also be used for the interaction between secondary phases.

- Grace et al. Model
  The model is well suited for gas-liquid flows where the bubbles can have a range of different shapes.

- Tomiyama
  As with the Grace et al. model, this model is well suited for gas-liquid flows in which the bubbles can have a range of shapes.

- Ishii Model
  Applies to boiling flows only.

- Universal Drag Laws for Bubble-Liquid and Droplet-Gas flows
  Is applicable to a variety of gas-liquid flow regimes and includes the bubble-liquid flow and droplet-gas flow models. These models are suitable for bubble-liquid and/or droplet-gas flow where the characteristic length of the flow domain is much larger than the average size of the particles.

With the complexity of the simulation in this thesis the default Schiller Neumann method will be used. When a stable solution with the Schiller Neumann method is achieved the effect of this choice can be investigated by switching to the Morsi and Alexander model. This investigation will, however, not be performed in the simulation as it is beyond the scope of this thesis.

3.7 Porous Media

The catalyst mesh structure manifests itself by reducing the available volume for fluid flow and a momentum source term in the energy equation. The fluid flow in a catalyst is complex and the best available method to approximate the flow is by modelling this region as a porous media. A porous medium is a heterogeneous system made of a solid matrix where the void is filled with fluids. By properly accounting for the role of each phase in this region the porous medium can be treated as a continuum [38].

Important parameters in a porous media is the porosity, which describes the relative occupancy of the fluid, and permeability, which describes how easily the fluid flow can move through the porous media [38]. The porosity, ε, is defined as

$$\varepsilon = \frac{V_v}{V_T}, \tag{3.7.1}$$

where V_v is the total void volume, where the fluid is present, and V_T is the total volume of the catalyst.

3.7.1 Porous Media Fluid Flow in Fluent

In Fluent, the solid volume blocking the fluid flow is not represented in the porous media model. Fluent therefore uses a superficial velocity, to ensure continuity of the velocity vectors across the porous media interface, and is calculated based on the volumetric flow rate. The superficial velocity is represented by

$$u' = \varepsilon u_{physical}. \tag{3.7.2}$$

The superficial velocity remains the same as the velocities outside the porous region, and cannot predict the velocity increase in porous zones and therefore limits this model. A more accurate solution can be used by modelling the porous media based on the physical velocity. The porous media momentum resistance is calculated seperately on each phase.

3.7.2 Pressure Drop in Porous Media

When the fluid flows through the catalyst, the fluid pressure drops. Numerous models have been developed to model pressure drop in porous media and the equations are often based on empirical results. Darcy introduced a one-dimensional empirical mode for *lamiar flow* through porous media [39]:

$$- \nabla p = \frac{\mu}{\alpha} u', \tag{3.7.3}$$

Darcy's law lacks the flow diffusion effects and is therefore not valid at the interface of a porous medium free flow [39]. This method is therefore the standard approach for single phase flow in microscopically disordered and macroscopically homogeneous porous media [40].

In *turbulent flow* both inertial and viscous effects increases the non-linear behaviour of the flow. Forchheimer added a term to Equation 3.7.3 and the Forchheimer equation is generally accepted as the extension to Darcy's equation for high flow rates [41]:

$$- \nabla p' = \frac{\mu}{\alpha} u' + \beta \rho u'^2, \tag{3.7.4}$$

where β is the non-Darcy coefficient or the inertial resistance coefficient and $\frac{1}{\alpha}$ is the viscous resistance coefficient.

3.7.3 Momentum Source Term

In the Eulerian multiphase model the following equations, describing a single phase flow, is applied to the corresponding flow. The conservation of momentum for invicid flow in porous media is defined by

$$\frac{\partial}{\partial t}(\rho \mathbf{v}) + \nabla \cdot (\rho \mathbf{v} \mathbf{v}) = -\nabla p + \rho \mathbf{g} + \mathbf{F}, \tag{3.7.5}$$

where p is the static pressure and ρg and F is the gravitational body force and external body forces. In a homogenous porous media, the F contains an additional momentum source term that is defined by [36]

$$S_i = -\left(\sum_{j=1}^{3} D_{ij}\mu v_j \sum_{j=1}^{3} C_{ij}\frac{1}{2}\rho|v|v_j\right), \tag{3.7.6}$$

where S_i is the source term for the x, y and z momentum equations, $|v|$ is the magnitude of the velocity and D and C are prescribed matrices. This momentum sink contributes to the pressure gradient in the porous cell, creating a pressure drop that is proportional to the fluid velocity in the cell. Comparing this equation to Equation 3.7.4 of homogeneous porous media

$$S_i = -\left(\frac{\mu}{\alpha}v_i + C_2\frac{1}{2}\rho|v|v_i\right) \tag{3.7.7}$$

the terms α, permeability, and C_2, the inertial resistance factor, simply specify the matrices D and C as diagonal matrices with $1/\alpha$ and C_2 on the diagonals. The permeability and initial resistance factor may be found by experiments performed to find the pressure drop over the porous media at different velocity rates and examine the trend line through these points or by semi-empirical relations such as the Ergun equation.

3.7.4   Ergun's Equation

The empirical Ergun's equation describes the pressure drop for flows going through packed beds containing packed columns of spheres, cylinders, round sand and other sphere shaped particles. Ergun's equation is given as [36]

$$-\nabla p' = \frac{150\mu(1-\varepsilon)^2 u'}{d_p^2\varepsilon^3} + 1.75\frac{(1-\varepsilon)\rho u'^2}{\varepsilon^3 d_p}, \tag{3.7.8}$$

where d_p is the average diameter of the spherical particle in the porous media, which in this case can be considered as the mesh wire diameter. This equation can be used to link the flow in porous media to the inertial resistance coefficient β, and the viscous resistance coefficient $\frac{1}{\alpha}$. Combining Equation 3.7.8 and Equation 3.7.7 the viscous and inertial resistance factor is given by:

$$\alpha = \frac{d_p^2}{150} \cdot \frac{\varepsilon^3}{(1-\varepsilon)^2}, \tag{3.7.9}$$

$$\beta = \frac{1.75}{d_p} \cdot \frac{(1-\varepsilon)^2}{\varepsilon^3}. \tag{3.7.10}$$

The Ergun's equation is able to accurately predict the pressure drop of single phase flow through porous media (with similar sized particles) within the porosity range of $0.35 < \varepsilon < 0.55$ [42]. The calculated porosity for this case was derived by dividing the catalyst mesh area by the total cylindrical area

$$\varepsilon = \left(1 - \frac{A_{mesh}}{\pi r_{cyl}^2}\right) \tag{3.7.11}$$

where r_{cyl} is the radius of the cylinder containing the catalyst. The porosity was calculated to be equal to 0.2, which is outside the range of the Ergun equation according to [42]. An experimental approach should therefore be used to find the inertial and viscous resistance coefficients, $1/\alpha$ and β. This was performed for the given case considered in this thesis and the complete calculations can be found in Appendix C.

The resulting coefficients from the experimental results were several orders of magnitude lower than expected and were therefore deemed unfit for this case. The reason for this issue is most likely due to the fact that the data was collected when both phases were present. Furthermore, although the same catalyst was used in the different runs of the experiment, the different configuration lead to a deviation in pressure drop over the catalyst and the mass flow rate was not remained constant throughout the experiment, due to other fluctuations in the system. In the simulation the values obtained by the Ergun equation was therefore implemented. With the approximation of setting the screen mesh diamater as the particle diameter in Equation 3.7.8, the viscous and inertial resistance coefficients were calculated to be

$$\frac{1}{\alpha} = 1.69759 \cdot 10^{11} \tag{3.7.12}$$

$$\beta = 1316418 \tag{3.7.13}$$

3.7.5 Equilibrium Thermal Model Equations

As the simulation in this thesis will not be modelling the thruster in a pulse mode firing and will only consider a steady state situation, the fluid flow inside the catalyst can be assumed to be in a thermal equilibrium with the catalyst material. The following equation is used to calculate the heat conduction flux in the catalyst medium by an effective conductivity with a transient term that includes the thermal inertia of the solid region

$$\frac{\partial}{\partial t}\left(\gamma \rho_f E_f + (1-\gamma)\rho_s E_s\right) + \nabla \cdot (\mathbf{v}(\rho_f E_f + p)) = S_f^h + \nabla \cdot \left[k_{eff}\nabla T - \left(\sum_i h_i J_i\right) + \left(\overline{\overline{\tau}} \cdot \mathbf{v}\right)\right].\tag{3.7.14}$$

The effective thermal conductivity in the porous medium, k_{eff}, is computed as

$$k_{eff} = \gamma k_f + (1-\gamma)k_s. \tag{3.7.15}$$

24

3.8   Heat and Mass Transfer Between Phases

With the Eulerian multiphase model it is possible to model the heat transfer between the phases. The internal energy balance for phase q is written in terms of the phase enthalpy, Equation 3.3.1, defined by

$$H_q = \int c_{p,q} dT_q \tag{3.8.1}$$

where $c_{p.q}$ is the specific heat at constant pressure of phase q.

Heat Exchange Coefficient

The volumetric rate of energy transfer between phases, Q_{pq} is assumed to be a function of the temperature difference and the interfacial area, A_i described in section 3.5. The rate is defined as

$$Q_{pq} = h_{pq} A_i (T_p - T_q) \tag{3.8.2}$$

where $h_{pq} = h_{qp}$ is the volumetric heat transfer coefficient between the pth phase and the qth phase. The heat transfer coefficient is related to the pth phase Nusselt number, Nu_p, by

$$h_{pq} = \frac{k_q N u_p}{d_p} \tag{3.8.3}$$

where k_q is the thermal conductivity of the qth phase and d_p is the bubble diameter.

3.8.1   Two-resistance Model

When modeling evaporation with the Eulerian model, it is generally recommended to use the Two-Resistance Model for heat transfer between phases [36]. This model considers the heat transfer as a separate process with different transfer coefficients on either side of the phase interface. At the interface between the qth and the pth phase, the temperature is assumed to be the same on both sides of the interface and is represented by T_S. The volumetric rates of phase heat exchange can be expressed as follows for the interface to the qth phase:

$$Q_q = h_q A_i (T_S - T_q) + \dot{m}_{pq} H_{qS}, \tag{3.8.4}$$

and for the interface to the pth phase

$$Q_p = h_p A_i (T_S - T_p) - \dot{m}_{pq} H_{pS} \tag{3.8.5}$$

where h_q and h_p are the phase heat transfer coefficients, and H_{qS} and H_{pS} are the phase enthalpies. The heat transfer coefficients can be computed in the same manner as in Equation 3.8.3. Since neither heat nor mass can be stored on the phase interface, the overall heat balance must be satisfied:

$$Q_q + Q_p = 0 \tag{3.8.6}$$

3.8.2 Thermal Phase Change Model

With the Two-Resistance Model enabled, the thermal phase change model is used to compute the heat transfer coefficients. In this model the evaporation-condensation process is governed entirely by the interphase heat transfer process and the overall heat balance. Applying Equation 3.8.4 and Equation 3.8.5 to a liquid-vapour pair gives for the interface to the liquid phase

$$Q_l = h_l A_i \left(T_S - T_l \right) + \dot{m}_{lv} H_{lS}, \tag{3.8.7}$$

and for the interface to the vapour phase

$$Q_v = h_v A_i \left(T_S - T_v \right) - \dot{m}_{vl} H_{vS}. \tag{3.8.8}$$

The interface temperature, T_S is determined from consideration of thermodynamic equilibrium. Ignoring the effects of surface tension on pressure, it is assumed that $T_S = T_{sat}$, the saturation temperature. By the heat transfer balance as given in Equation 3.8.6, the mass transfer through evaporation from the liquid to the vapour phase can be expressed as:

$$\dot{m}_{lv} = \frac{h_l A_l \left(T_{sat} - T_l \right) + h_v A_i \left(T_{sat} - T_v \right)}{H_{vS} - H_{lS}} \tag{3.8.9}$$

The phase enthalpies, $H_v S$ and $H_l S$, need to be computed correctly to account for the discontinuity in static enthalpy due to latent heat between the two phases as well as heat transfer from either phase to the phase interface. The conditions given for the evaporation-condensation model are given for evaporation, where $\dot{m}_{lv} \geq 0$

$$\begin{aligned} H_{lS} &= H_l \left(T_l \right) \\ H_{vS} &= H_v \left(T_{sat} \right) \end{aligned} \tag{3.8.10}$$

and for condensation, where $\dot{m}_{lv} < 0$

$$\begin{aligned} H_{lS} &= H_l \left(T_{sat} \right) \\ H_{vS} &= H_v \left(T_v \right) \end{aligned} \tag{3.8.11}$$

26

This leads to a formulation that is stable both physically and numerically, as it implies that the denominator in Equation 3.8.9 is non-zero, being greater or equal to the latent heat.

$$L = H_v\left(T_{sat}\right) - H_l\left(T_{sat}\right) \tag{3.8.12}$$

3.9 Heterogeneous Reaction Model

In addition to the evaporation described in subsection 3.8.2, volumetric reaction mechanisms can be modelled as part of the phase interactions of multiphase flows. This makes it possible to model the decomposition as a heterogeneous reaction; a reaction including two different phases. To compute the heterogeneous phase interaction rate with the Eulerian multiphase model enabled, a built in Arrhenius rate model can be used or by a user-defined function (UDF).

A UDF is a script that is written in C code with a specially developed library of functions for Fluent. An initial attempt was performed to create a UDF to apply both thermal and catalytic decomposition to the simulation. The catalytic decomposition rate would then only be calculated in the zone ID of the porous media zone, i.e. the catalyst.

The UDF model proved to be unstable and the results did not correspond to the expected values during an initial simulation of only the decomposition process. In addition, the UDF is not written in a manner that makes it possible to use parallel processing on a supercomputer, and it was therefore deemed not efficient enough for this simulation. The built in Fluent Arrhenius model was therefore selected, where only the catalytic reaction would be modelled. The catalytic reaction is highly volatile and the effects of the thermal decomposition on the overall process can therefore be regarded as negligible. The rate expression used in the Arrhenius model is given by

$$Rate = k\prod_{i=1}^{N} R\left(\frac{Y_i \rho_{ip} VOF_{ip}}{MW_i}\right)^{st}\left[\frac{kmol}{m^3 s}\right], \tag{3.9.1}$$

where

$$k = A\left(\frac{T_{ip}}{T_{ref}}\right)^{b}\exp\left(\frac{-E}{RT_{ip}}\right). \tag{3.9.2}$$

Y_i is the ith species mass fraction, NR the total number of reactants in a given inter-phase reaction, ρ_{ip} is the bulk density of the phase ip, VOF_{ip} is the volume fraction of the phase ip, MW_i is the molecular weight [kg/kmol] of the reactant species, st is the stoichiometric coefficient of the reactant in the given reaction, and k is the rate constant.

3.10 Available Surface Area for Catalytic Reaction

In reality, the catalytic decomposition is dependent upon the available surface for reaction in the catalyst as described in subsection 2.1.2. The only method that can be used to model a surface reaction in Fluent is through the species transport model. The surface

reactions can only occur within one mixture of species, and the reaction would thereby be a single phase homogenous reaction and not a multiphase hoterogeneous reaction. In Fluent, it is therefore not possible to model a surface reaction as part of a multiphase problem. The heterogeneous reaction must therefore be modelled as a volumetric reaction through the interphase interaction models.

As further elaborated on in subsection 2.1.2, the fluid flow prevents the formation of a velocity and diffusion boundary layer and the decomposition is thereby reaction limited. This means that it is not necessary to include further deactivation or restrictions to the decomposition process other than the limitation connected to the available surface for reaction.

As described in section 3.7 the porous media model in Fluent does not include the volume of the catalyst material. With a porosity of 0.2, the volume fraction within a cell includes 80% more hydrogen peroxide than it should. This over-estimation would thereby lead to a higher reaction rate. In addition to this limitation in the model, there exists other effects which reduces the available surface for reaction and must be taken into consideration. With this in mind, an approximation of the volume percentage that is actually taking part in the reaction mechanism was estimated. This is done in order to bridge the gap between the simulations volumetric reaction and the real life surface reaction.

The following subsections describe the limiting factors of the available surface area on the catalyst surface that can lead to an estimated volume/surface area that is active in the reaction.

3.10.1   Bubble Formation

At the catalytic surface, gas bubbles are formed during the reaction process. When these bubbles form, they occupy a given fraction of the surface which reduces the number of active sites on the catalyst. When the bubbles are removed, liquid is brought into contact with the surface and reaction may take place again. In the interest of estimating the reduction of active sites for decomposition caused by these bubbles it is important to determine the different fluid flow regimes in the catalyst.

The catalytic decomposition of hydrogen peroxide is a volatile reaction, this process can be compared to a boiling process. In this comparison the reaction heat can be accounted for in the same manner as the heat flux, $q"_s$, from the surface where boiling is taking place. The classical theory of pool boiling, with its different regimes, as a function of $q"_s$ versus ΔT is plotted in Figure 3.1.
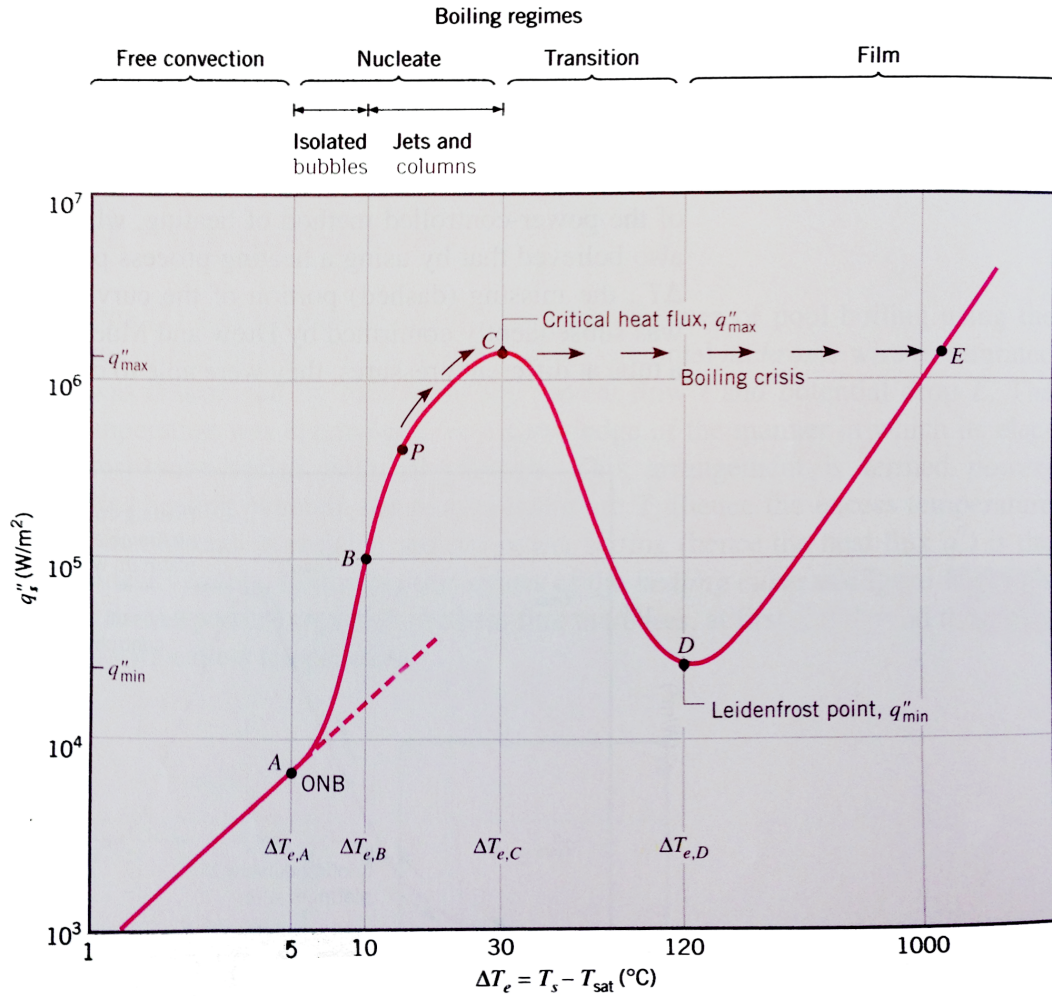
Figure 3.1. Typical boiling curve for water at 1 atm: surface heat flux $q"_s$ as a function of excess temperature, $\Delta T_e = T_s - T_{sat}$ [10].

In convective pool boiling the different flow regimes have the following characteristic behaviour [10]:

1. Free Convection Boiling
   As seen in Figure 3.1, the surface temperature T_s, must be slightly higher than the saturation temperature, T_{sat}, to sustain bubble formation. In this region, bubble inception will occur, but the fluid motion is determined by free convection effects, until the onset of nucleate boiling at point A.

2. Nucleate Boiling
   In the region A-B, isolated bubbles form and separates from the surface. Beyond this point the bubbles interfere and coalesce and in the region B-C the vapour escapes as jets or columns. At point P in this region, the critical heat flux $q"_{s,C} = q"_{max}$ is reached and the large amount of vapour formation makes it difficult for the liquid to wet the surface.

3. Boiling Crisis
   If the $q"_s$ is further increased from point C, boiling crisis occurs where the surface temperature abruptly increases and may exceed the melting point of the solid.

If the surface temperature, T_s is controlled from point C the behaviour enters into the following regimes

4. Transition Boiling
   This regime also goes by the name unstable film boiling or partial film boiling. The bubble formation is now so rapid that a vapour film starts to form on the surface and may oscillate between film and nucleate boiling.

5. Film Boiling
   At this point a vapour blanket is surrounding the surface at all times.

In this simulation, the most important effect seen in pool boiling that needs to be considered, is the formation of a vapour film and whether or not this film is stable enough to fully develop and occupy the complete surface of the catalyst. This formation would in turn reduce the reaction rate extensively, as the liquid is not able to reach the surface. To investigate the stability of these vapour films, the different aspects which influences the onset of this stage in a boiling process must be further elaborated.

The above described process and different flow regimes during boiling is given for convection pool boiling, where boyancy is the driving factor in the vapour removal from the surface. When hydrogen peroxide decomposes, the gas volume is 62 times larger than the liquid [22], so the buoyancy forces would be large. In addition, with a bulk fluid in motion in the catalyst, the different flow regimes would be more similar to flow in a tube with forced convection boiling as depicted in Figure 3.2.
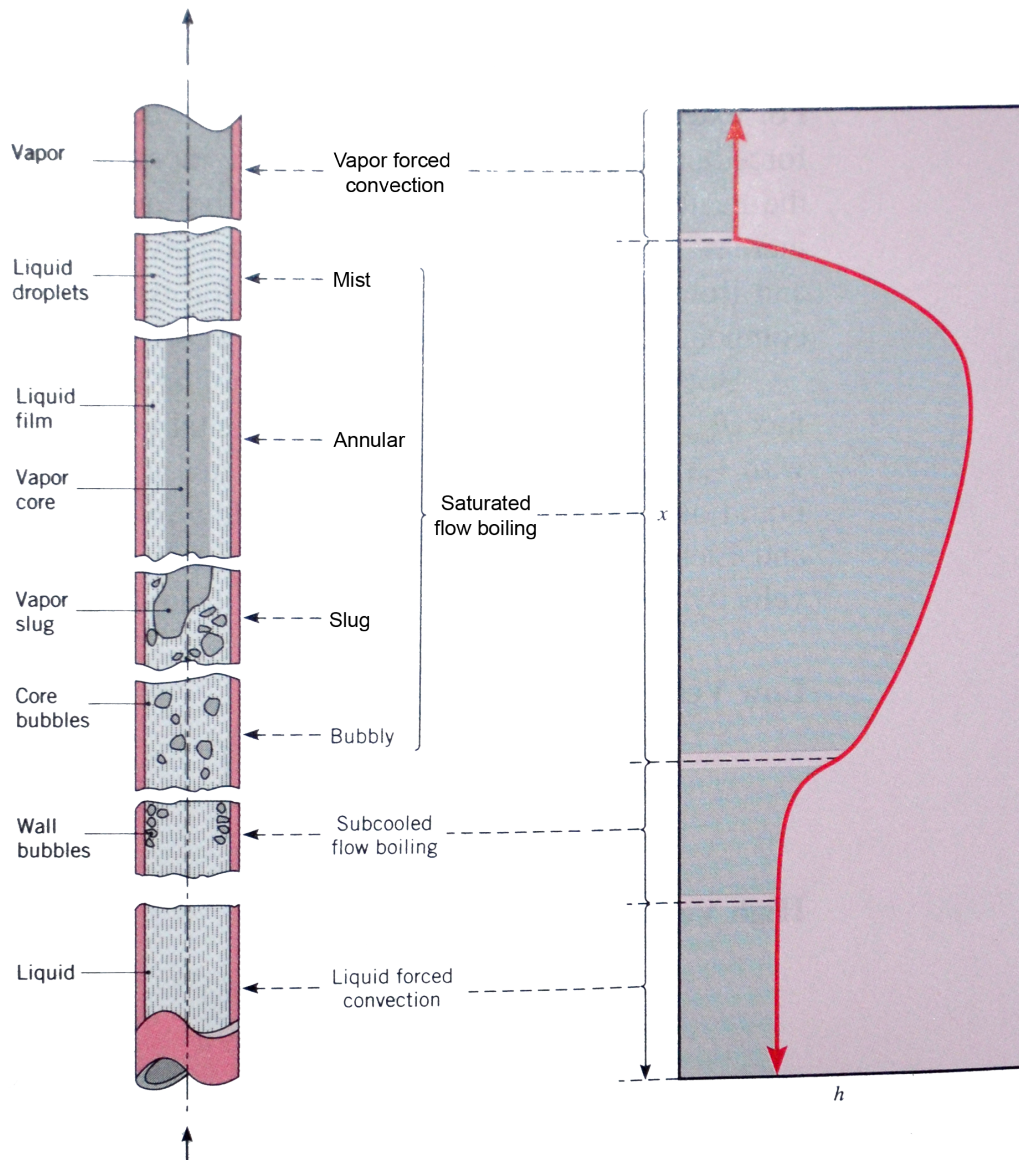
Figure 3.2. Flow regimes for forced convection boiling in a tube [10].

During forced convection boiling the maximum heat flux $q"_{max}$ is increased. In the case given in Figure 3.1 the $q"_{max}$ is increased from 1 MW in convection boiling to 35 MW for forced convective boiling [10]. Linking this effect to the decomposition of HTP, this would mean that the heat released during the reaction process can be higher with a moving bulk fluid before entering into the regime similar to film boiling. This effect can be contributed to the bulk fluid motion that is counteracting the formation of a boundary layer at the surface. In order to determine the $q"_{max}$ for HTP, the boiling curve must be determined for the HTP and water solution in a close proximity to the steady state pressure and temperature in the catalyst.

As mentioned earlier the fluid flow inside the catalyst is more similar to that of forced convection boiling in a pipe. In the catalyst, the pipe would thereby be the open area in the mesh. The hydraulic diameter, D_h, of this "pipe", as seen in Figure 3.3, is very small in a mesh wired catalyst. In the case considered in this thesis the hydraulic diameter is in the scale of millimetres. The fluid flow would therefore have characteristics which are

more similar to micro-channel flow. In micro-channel flow the boiling curve is not the same as in a larger scaled pipe.
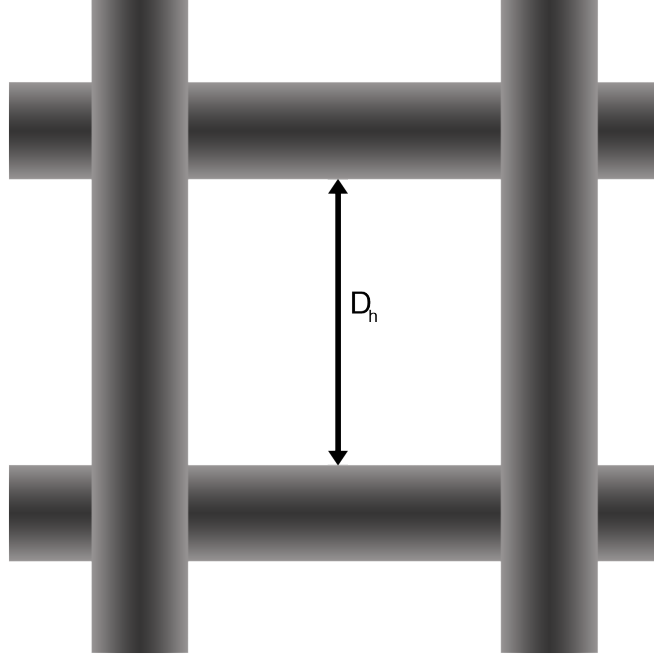
Figure 3.3. Catalyst mesh treads and hydraulic diameter.

In addition to the microchannel flow altering the boiling curve, there exists additional limitations when comparing these types of flows to the catalyst fluid flow. If the mesh threads are considered as a stand alone cylinder, the vapour bubbles formed could enfold the complete surface if the cylinder diameter is smaller than the capillary length scale L_b, which is defined by [43]

$$L_b = \sqrt{\frac{\sigma}{g(\rho_l - \rho_v)}}. \tag{3.10.1}$$

The correlation of the bubble departure diameter, d_d, and the capillary length, L_b, is typically in the order of $d_d/L_c=1$ in most systems [43]. To determine if the bubbles could in fact enfold the complete surface of a catalyst mesh wire, the capillary length of HTP must be calculated.

The density of 87.5 wt% hydrogen peroxide was found to be 1378.5 kg/s at 20 degrees celcius [44] with a surface tension of 0.079 N/m, which was calculated by a second order polynomial interpolation of values from the Evonik specifications for HTP [45]. As the temperature increases the density of HP will decrease, the same goes for the oxygen gas and water vapour. Calculating the capillary length scale as a critical diameter with a gas phase density equal to that of water vapour at 0.5863 kg/m [10], to get the minimum diameter value, we get

$$L_b = \sqrt{\frac{0.079 \text{ N/m}}{9.81 \text{ m}/s^2 (1378.5 \text{kg}/m^3 - 0.5863 \text{ kg}/m^3)}} = 0.0024\text{m}. \tag{3.10.2}$$

The catalyst mesh considered in this thesis has a thread diameter less than one millimetre, which is below the critical diameter. As a consequence, the classical pool boiling theory may not be applied in this case, as the form of the boiling curve would deviate from the one presented earlier in this section. The boiling curve according to classical theory can therefore only be used as a reference point to the different regimes in the catalyst, but it is not possible to draw any final conclusion connected to the onset of the different regimes in the catalyst. Experimental results are therefore necessary to fully comprehend to what extent this would affect the reduction in available surface area.

3.10.2   Wetting

An important factor that will influence the catalytic decomposition rate of HTP is how well the surface is able to be wetted by the liquid HTP. When a liquid is dropped on a surface with poor wettability properties the droplet will sustain its form on the surface, with a given angle, dependent upon the surface characteristics as seen in Figure 3.4. When the fluid flow has transition into a region where the liquid is only present in the form of bubbles, the wettability would then determine the contact area between the liquid and the surface.
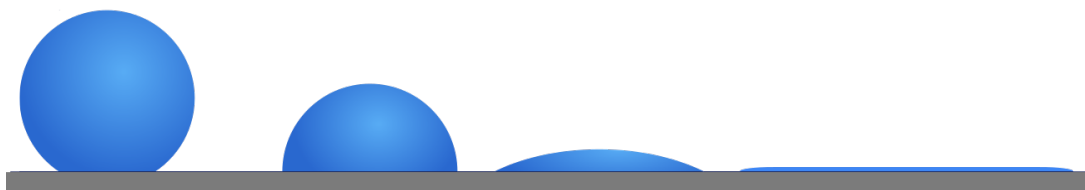
Figure 3.4.   Figure of different wetting properties of different fluids with increasing wetting from left to right.

3.10.3   Catalyst Deactivation

Another important factors that can reduce the decomposition rate in a catalyst is the extent of degradation over time. Several different processes are involved, and the traditional classifications of degradations are sintering or aging, fouling and poisoning [7].

Sintering

Sintering is a thermal degredation of the catalyst due to prolongued exposure to gases with high temperature [7]. When the temperature inside the catalyst exceeds or is operating in a region close to the melting point of the solid, small sections of the catalyst will melt together. The new formed geometry will thereby have a smaller surface area than its original form as separated mesh structures. This will in turn decrease the available surface for reaction. When designing a catalyst it is important to select a catalytic material that has the proper reaction characteristics in addition to a large enough melting point to prohibit sintering degradation.

33

Fouling

Fouling is a mechanical degradation of the catalyst and occurs when unwanted material is physically deposited on the surface, which prevents further catalytic reaction [46]. In its advanced stages it may result in disintegration of catalyst particles and plugging of the catalyst voids. This type of degradation is most often seen in catalyst involved with hydrocarbon reactions, where coke is formed on the surface. In the process described in this thesis these types of molecules are not involved, and this effect is assumed to be negligible.

Poisoning

Poisoning is a chemcial degradation due to strong chemisorption of species on catalytic sites [46]. The poisoning molecules become irreversibly chemisorbed to active sites, thereby reducing the number of sites available for the main reaction. In addition to physically blocking of adsorption sites, adsorbed poisons may induce changes in the electronic or geometric structure of the surface. The poisoning molecule, P, may be a reactant and/or a product in the main reaction or an impurity that has entered into the feed stream. Whether a species acts as a poison depends upon its adsorption strength relative to the other species competing for catalytic sites.

As discussed in subsection 2.1.1, a complete and generally supported decomposition mechanism for HTP has not been developed. It is therefore difficult to determine what kind of intermediate species would have a large enough effect to poison the catalyst. In the simulation considered in this thesis the reaction will be modelled as the overall reaction described in Equation 2.1.1, the effect of poisoning will therefore not be included in the reaction model.

3.10.4 Arrhenius Equation Implementation

As discussed in section 3.7, the catalyst will be modelled as a porous media. In this model the solid part of the catalyst will not be resolved, and the model is used primarily to simulate the pressure drop over the catalyst. With this limitation, the volume fraction of hydrogen peroxide in the catalyst is therefore overestimated.
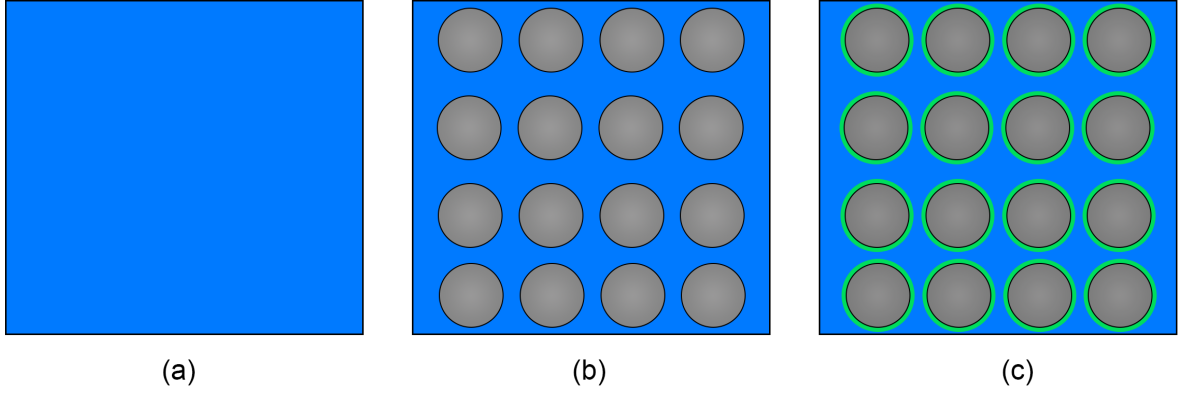
Figure 3.5. Figure describing the volume fraction involved in the catalytic reaction. (a) depicts the volume fraction of HTP=1, in blue, as Fluent does not include the solid in a given control volume. (b) depicts the actual volume fraction of HTP, blue section, in-between the solid catalyst material. (c) depicts the volume fraction, green colour, that is in contact with the surface and takes part in the reaction.

As seen in Figure 3.5, only a small portion of the HTP volume is active in the catalytic process. The issue connected to this way of modelling the catalyst is then found in how the catalytic reaction is modelled. The reaction is modelled as a volumetric reaction, not a surface reaction. It is therefore important to find a reasonable method to calculate the volume fraction of the fluid that is actually taking part in the reaction, as the reaction is a surface reaction. A theoretically developed model or theory has not been found, and an initial approximation must therefore be made. Through a model verification method of the reaction mechanism, this approximation can be validated or give way to iterate to a more correct approximation.

Most of the bulk fluid between the catalyst surface will move further into the catalyst due to the pressure and momentum forces until it gets closer to the surface and reacts. As calculated by Equation 3.7.11, the porosity of the catalyst in this case is equal to 0.2, which means that the volume of fluid as seen in Figure 3.5 b is equal to 20% of the total volume calculated by fluent, as seen in case (a) of Figure 3.5. In addition, as seen in case (c) only a smaller portion of this liquid is in physical contact with the surface per second. Keeping the effects of reduction on area as described in section 3.10 in mind and taking a conservative tall on this matter, one could assume that 10% of the liquid in a given control volume is active in the catalytic reaction. The final rate expression will therefore be equal to

$$Rate = 0.2 \cdot 0.1 \cdot k \prod_{i=1}^{N} R \left(\frac{Y_i \rho_{ip} VOF_{ip}}{MW_i} \right)^{st} \left[\frac{kmol}{m^3 s} \right]. \tag{3.10.3}$$

In experimental data, it has been found that the reaction is extremely volatile and in the temperature data it can be seen that a decomposition plane exists. The plane marks that the phase change and reaction occurs almost instantaneously. The experimental results on the position of this plane in the catalyst can be used to verify the simulation results and the actual volume fraction involved in the catalytic process.

3.11 Turbulence Model

Turbulent flows are characterized by a random and chaotic variance in velocity and other flow properties [47]. They also contain rotational flow structures which are termed turbulent eddies. The properties of larger eddies in turbulent flow are dominated by inertial effects. The dimensionless Reynolds number, which describes the relation between inertial forces and viscous forces, is therefore used to determine whether or not the flow regime is laminar or turbulent [9] and is defined as

$$Re = \frac{\rho u L}{\mu}. \tag{3.11.1}$$

3.11.1 Reynolds Averaging Navier-Stokes Equation

To solve the flow field of a turbulent flow the Navier-Stokes equation can be used with direct numerical simulation (DNS). This method is computationally demanding and expensive, and this method is mostly used on smaller scale issues for research purposes. With the case considered in this thesis the Reynolds Averaged Navier-Stokes (RANS) equation is therefore applied instead. The RANS equation decomposes instantaneous quantities into time-averaged values and fluctuating terms, and coupled with a turbulent closure model it is possible to model turbulent flow on larger scales with considerably lower computational costs.

The most well known closure model is the $k - \epsilon$ model. It is based on the presumption that there is a relationship between the action of viscous stresses and Reynolds stresses on the mean flow [48]. Two extra equations are added to the governing equation, one containing the turbulent kinetic energy per unit mass k, and the other the dissipation rate of turbulent kinetic energy per unit mass ϵ.

3.11.2 SST k-omega

The result by Balabel et. al. [49] on a simulation of a nozzle flow displayed that the empirical turbulence model shear-stress transport (SST) k-ω exhibited the best over-all agreement with experimental data. This model was therefore selected as the turbulence model for the simulation in this thesis.

SST k-ω is a combination of k-ω and k-ϵ where the standard k-ω model operates in the near-wall region and a modification of the k-ϵ is activated in the far field [36]. This model accounts for the transport of turbulent shear stress and it is especially suited for flow separations [37]. The k-ω equations are described in Fluent as follow [36]

k-equation:
$$\frac{\partial}{\partial t}(\rho k) + \frac{\partial}{\partial x_i}(\rho k u_i) = \frac{\partial}{\partial x_i}\left(\Gamma_k \frac{\partial k}{\partial x_j}\right) + \tilde{G}_k - Y_k + S_k \tag{3.11.2}$$

ω-equation:
$$\frac{\partial}{\partial t}(\rho \omega) + \frac{\partial}{\partial x_i}(\rho \omega u_i) = \frac{\partial}{\partial x_i}\left(\Gamma_\omega \frac{\partial \omega}{\partial x_j}\right) + G_\omega - Y_\omega + S_\omega \tag{3.11.3}$$

In these equations, the $\tilde{G}_k$ represents the generation of turbulent kinetic energy due to mean velocity gradients. G_ω is the generation of ω, Γ_k and Γ_ω are the effective diffusivity of k and ω. Y_k and Y_ω represent the dissipation of k and ω due to turbulence. D_ω represents the cross-diffusion term and the S_k and S_ω are user defined source terms.

In the default settings of porous media in Fluent, the turbulent quantities are treated as though the solid medium has no effect on the turbulence generation or dissipation rates [36]. This assumption is reasonable for flows where the medium's permeability is large and the geometric scale of porous medium does not interact with the scale of turbulent eddies.

3.12 Fluent Solvers

The two pressure-based solvers available in Fluent for Euerian multiphase flow is the phase coupled SIMPLE (PC-SIMPLE) and the coupled solver. The PC-SIMPLE is an extension of the segregated solver SIMPLE (Semi-Implicit Method for Pressure-Linked Equations). In this solver the velocities are solved coupled by phases, but in a segregated fashion, where a vector equation formed by the velocity components of all phases is solved simultaneously by the block algebraic multigrid scheme used by the density-based solver. A pressure correction equation is thereafter built on the total volume continuity, and the pressure and velocities are then corrected to satisfy the continuity constraint.

The Pressure-Correction Equation

For incompressible multiphase flow, the pressure correction equation is defined as

$$\sum_{k=1}^{n} \frac{1}{\rho_{rk}} \left[\frac{\partial}{\partial t} \alpha_k \rho_k + \nabla \cdot \alpha_k \rho_k \mathbf{v}_k' + \nabla \cdot \alpha_k \rho_k \mathbf{v}_k * - \left(\sum_{l=1}^{n} \left(\dot{m}_{lk} - \dot{m}_{kl} \right) \right) \right] = 0 \qquad (3.12.1)$$

where ρ_{rk} is the phase reference density for the kth phase, which is defined as the total volume average density of phase k. $\mathbf{v}_k'$ is the velocity correction for the kth phase, and $\mathbf{v}_k *$ is the value of $\mathbf{v}_k$ at the current iteration. The velocity corrections are themselves expressed as functions of the pressure corrections.

Volume Fractions

The volume fractions as discussed in section 3.4 are obtained from the phase continuity equations. in discretised form, the equation of the kth volume fraction

$$a_{p,k} \alpha_k = \sum_{nb} \left(a_{nb,k} \alpha_{nb,k} \right) + b = R_k, \qquad (3.12.2)$$

in order to satisfy the condition that all the volume fractions sum to one.

Chapter 4

Fluent Simulation Setup

4.1 Geometry

The Geometry of the total domain includes a total length of 1.1 meters, with a heigth 0.3 meters. The domain is split into three different zones; porous, nozzle and ambient. The different zones are interfaced in Fluent, which alters the mesh to improve the node connection between the elements on the boundaries of these zones. The two interfaces in the geometry are indicated in Figure 4.1 by a white line. The nozzle is designed for atmospheric pressure with an aspect ratio of 3.36. The main goal of the thruster simulation is to have a complete decomposition at the catalyst outlet to maximise thrust.

Figure 4.1. Geometry setup in Fluent split into the porous, nozzle and ambient zones.

The nozzle geometry was created by importing coordinate points which where defined by a polynomial function derived from the vacuum designed nozzle. The complete set of coordinate points can be found in Appendix A

4.2 Mesh

Several iterations of the mesh was performed due to reoccurring stability issues while performing the simulation. In order to rule out the mesh as a dominant source for these stability issues, the iterations consisted of further enhancements on quality measures, such as orthogonal quality and skewness. The first iteration consisted of a 2D model, which was not axisymmetric and with a structured and more coarse mesh. To increase the number of elements in the mesh it was also cut in half to reduce the total amount of

elements and in turn reduce the computational costs in addition to being more realistic compared to a physical thruster.

The mesh consists of a large number of quadrilateral and a small number of triangular elements. An important consideration whilst developing the mesh grid was the numerical diffusion, which is not a real phenomena but a consequence of representing the fluid flow equations in discrete form with a given truncation error. The amount of numerical diffusion is inversly proportional to the mesh resolution; by increasing the resolution, the numerical diffusion would decrease [37]. In addition, the numerical diffusion is minimised when the flow is aligned with the mesh. In a triangular mesh the flow will never be aligned with the flow, and the number of triangular cells should be kept to a minimum. By enforcing the complete domain to contain only quadrilateral elements, the skewness factor increased significantly. The highly skewed elements close to the nozzle wall would be a large source for simulation instability and caused the solution to diverge. A combination of triangular and quadrilateral elements was therefore selected to enhance convergence. The final mesh of the thruster is found in Figure 4.2, which does not depict the complete domain which is seen in Figure 4.3.
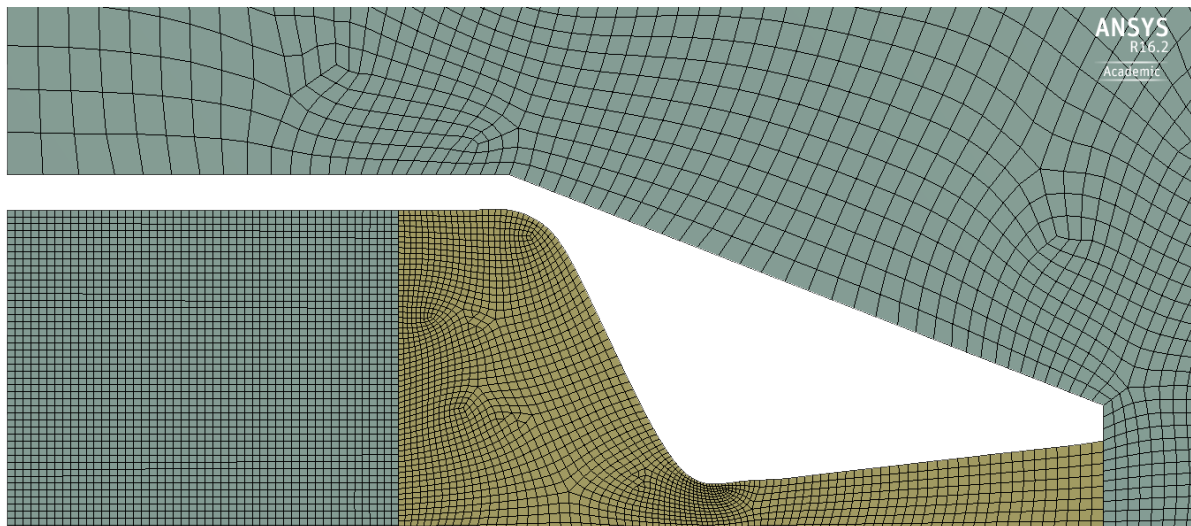
Figure 4.2. Fluent mesh of the monopropellant thruster.
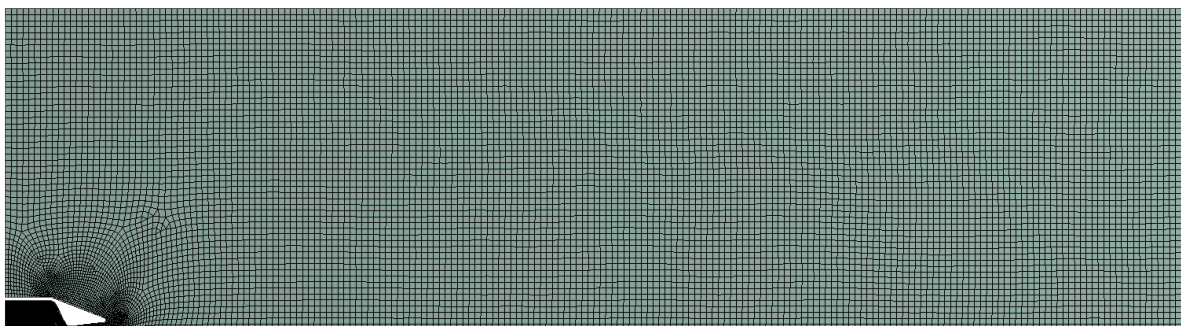
Figure 4.3. Fluent mesh of the entire domain.

To evaluate the element quality in the final mesh, particularly the orthogonal quality and skewness, an element plot was created in ANSYS Mesher. The minimum orthogonal quality in the mesh was 0.79, and the distribution of the number of elements with different quality is charted in Figure 4.4.

According to a lecture held at an official Fluent introduction course [50], elements with an orthogonal quality between 0.70 to 0.95 are considered to be very good and in the range of 0.95 to 1 the elements are considered to be excellent. By closer inspection of the orthogonal quality chart, only a small number of elements have a quality lower than 0.95. These cells can be found in the nozzle zone and the ambient zone close to the corners of the wall above the nozzle, as seen in Figure 4.5. As large gradients are not expected in this region, these elements would not cause issues in the simulation.
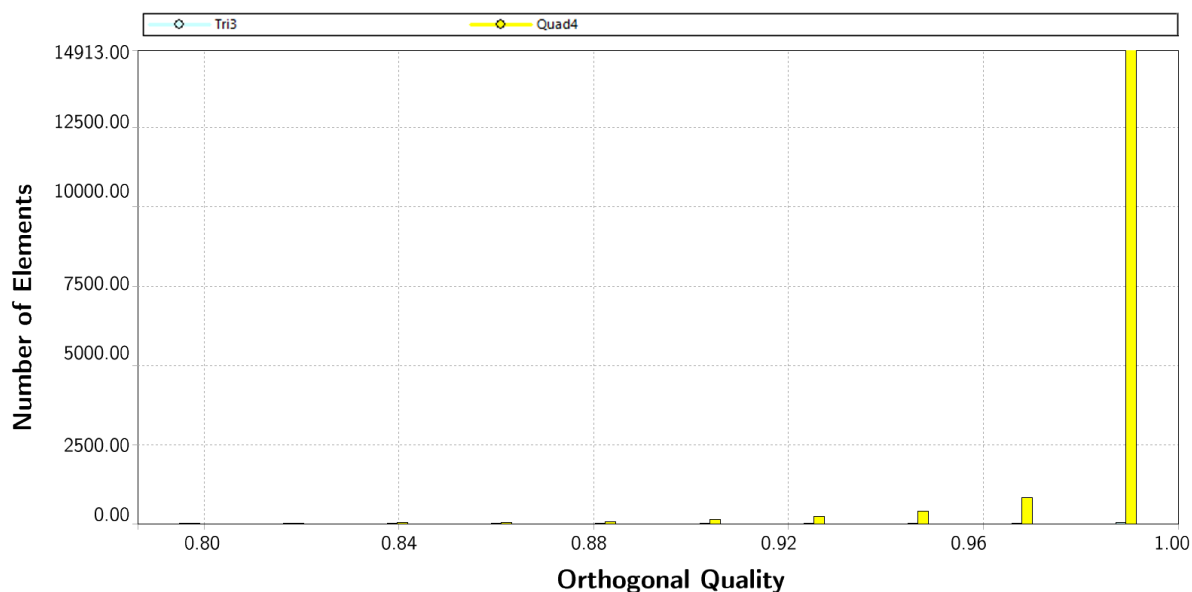
Figure 4.4. Bar chart of number of elements versus mesh orthogonal quality.
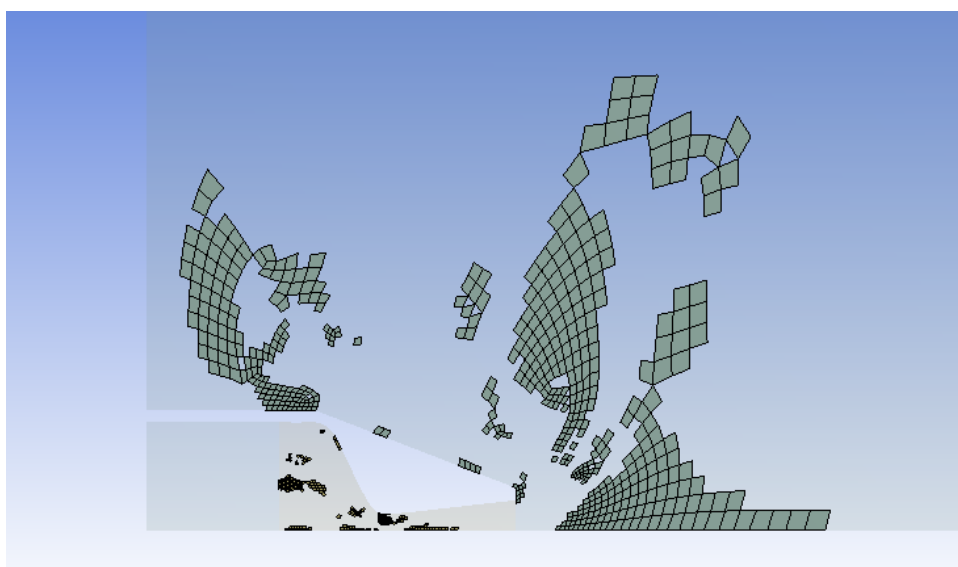
Figure 4.5. Elements with an orthogonal quality in the range of 0.79 to 0.95.

The maximum skewness was 0.47 in the final mesh, and the number of elements with different skewness metrics are charted in Figure 4.6. The elements with a skewness of 0.50-0.25 are considered to be very good, according to [50], and in the range of 0.25-0.00 they are classified as excellent. Trying to enhance the orthogonal quality of the mesh increased the maximum skewness of the mesh. The final mesh is the best fit between the two factors.
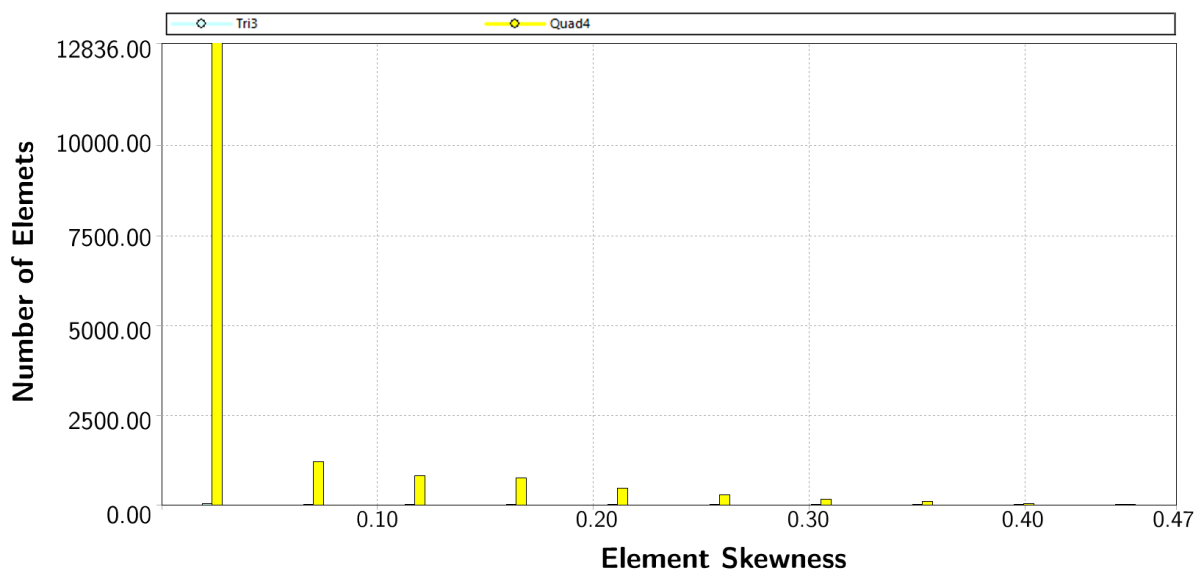
Figure 4.6. Bar chart of number of elements versus mesh skewness.

When the mesh was imported into Fluent, the quality was further improved by the built in Mesh smooth function. The quality based smoothing in Fluent divides the mesh into a number of 'bins' and improves the cells in those bins that exhibits the lowest orthogonal quality. With this smoothing method, the quality of the mesh improved, and the final values of the mesh quality is given in Table 4.1.

Table 4.1. Mesh quality metrics.

Mesh metrics	Current values	Ideal values
Number of elements	16553	-
Minimum orthogonal quality	0.827	1
Minimum ortho skew	0.173	0
Maximum aspect ratio	4.478	<5

The mesh in this case must be able to handle large gradients, as the simulation is dealing with supersonic flow in a nozzle which could lead to the formation of strong shock waves. To handle these types of phenomena the resolution of the mesh must be high, and the total number of elements was therefore increased to a large extent in the regions where these gradients are expected. In total the mesh can be classified as a very good mesh. However, with the expected complex flow pattern in the simulation, the different rules of thumb given in [50] are a matter of further discussion, but that is beyond the scope of this thesis.

4.3 Boundary Conditions

From the geometry, six boundary conditions are defined for the axisymmetric geometry. Their names have been defined as listed in Table 4.2 with the corresponding number as seen in Figure 4.7 and Figure 4.8.
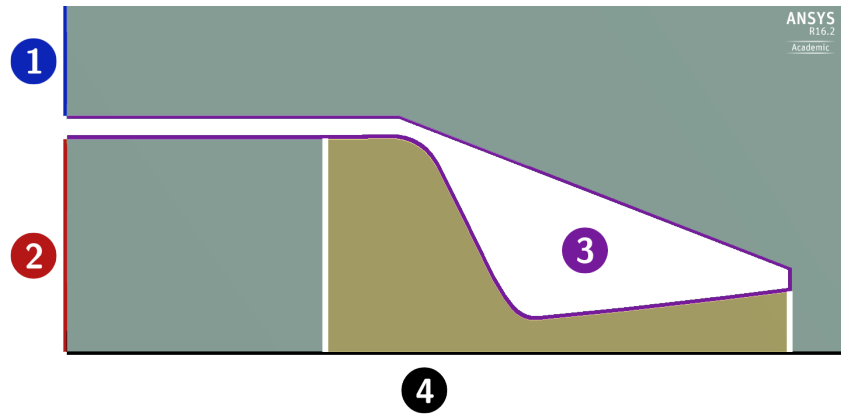
Figure 4.7. Boundaries close to the thruster.
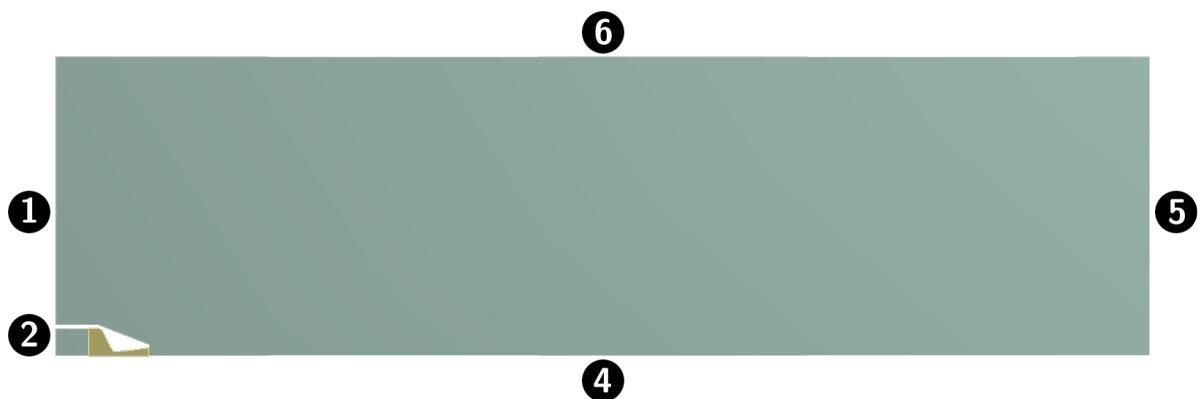
Figure 4.8. Boundaries in the complete domain.

Table 4.2. Boundary names according to numbers in Figure 4.7 and Figure 4.8.

Boundary number	Boundary name
1	Atmosphere Vertical
2	Inlet
3	Wall
4	Axis
5	Outlet
6	Atmosphere Horizontal

In Fluent the boundary number 3, nozzle wall, is separated into three sections; the porous zone wall, nozzle wall and atmospheric wall.

The inlet (2) was set to a mass inlet, as the case itself is defined by a constant mass flow rate of 150 g/s. The vertical atmospheric boundary (1) was set as a mass flow rate inlet with air entering the domain to remove numerical noise and thereby enhance stability.

The outlet boundary (5) is set to a gauge pressure = 0, this condition is similar to the Neumann boundary condition, where the pressure will not be enforced to 0 in case of a different pressure field arriving at this boundary. When the plume reaches this point it does, however, cause flow to re-enter the domain, something which the Neumann condition would not. If necessary this boundary can be switched to the Neumann condition by implementation of a UDF. When the flow has reached this point the influence on the upstream flow in the catalyst is assumed to be negligible and will not affect the solution to this problem. The implementation of a UDF defined boundary condition was therefore not performed.

Chapter 5

Results with the Eulerian Multiphase Model

The Eulerian multiphase model is the most complex multiphase model in Fluent and convergence is thereby difficult to obtain. The equations in this model are closely linked, and the additional models included in this model contributes to increase the overall residuals. An instability in one of these models would then influence the overall stability of the model and divergence would occur. These instabilities proved to be the biggest challenge in this simulation.

As the case involves compressible flow the time-stepping method and adaptive time stepping method cannot be used [37]. The time step must therefore be set as a constant and defined by the CFL condition. The CFD criterion states that the Δt should be the minimum of Δt_x and Δt_y [51], which are defined as

$$\Delta t_x = \frac{\Delta x}{u + a} \tag{5.0.1}$$

$$\Delta t_y = \frac{\Delta y}{v + a} \tag{5.0.2}$$

where a is the local speed of sound, which is defined for an ideal gas as $\sqrt{kTR}$ [9] with R being the universal gas constant, T the temperature and k being the adiabatic index / isentropic expansion factor defined as the heat capacity ratio C_p/C_v of the fluid.

In this simulation the mesh resolution is high, and Δx is therefore a very small number, which in turn demands a small time-step. The finest mesh is found inside the thruster as seen in Figure 5.1.

Assuming that the smallest cell volume, A_{min} consists of a square, then the $\Delta x = \Delta y = \sqrt{A_{min}}$. To estimate the time step, the speed of sound for air at sea level, $a = 340$ m/s was used to find

$$\Delta t = \frac{\sqrt{A_{min}}}{a_{air}} = \frac{\sqrt{3.11 \cdot 10^{-8} m^2}}{340 m/s} = 5.05 \cdot 10^{-7}. \tag{5.0.3}$$

The simulation time step was therefore always held at a lower time step than 5^10-7 to ensure convergence. During the simulation convergence was not obtained and by reducing the time step even further the solution still diverged.

The error messages given in Fluent, which describes the cause of the divergence in the solver during the simulation are limited. As the web of equations are strongly linked to each other, divergence in one equation could have another root issue. In order to
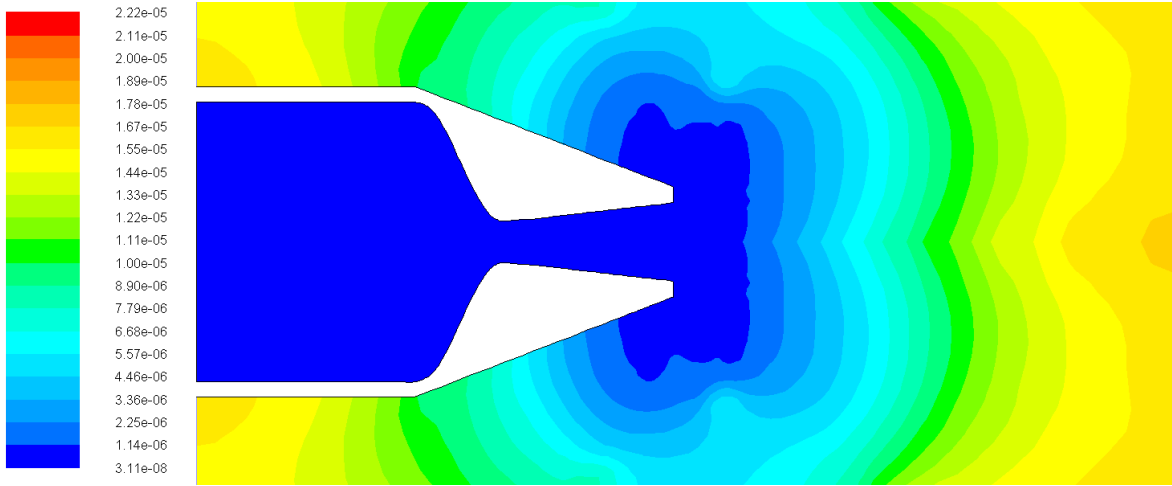
Figure 5.1. 2D cell volume in the simulation mesh.

investigate these issues a flow chart of the information flow between the equations was made and is found in Figure 5.2.

The information flow in Figure 5.2 consists of the different terms passed from one model to the other in accordance with the equations presented in chapter 3. This figure therefore only depicts a small portion of the actual information flow in the simulation as chapter 3 only covers the parts that are specific for this simulation. Despite its lack of complete information flow, from the figure it is clear that a divergence in the momentum equation could be linked to several other models in the simulation.

Because of the nonlinearity of the equation set being solved by Fluent, the under-relaxation factor is used to control the update of computed variables at each iteration of a given equation. This process can be further clarified by looking at the numerical Newton-Rapson method. In this method an initial guess is made, x_0, to the root of the function $f(x)$ through an iterative process the correct value, as defined by a certain accuracy level, of the solution is found. By including an underrelaxation factor to this method as defined in [52], the solution method is given by

$$x_{n+1} = x_n + C\frac{f(x)}{f'(x)}, \tag{5.0.4}$$

where C is the under- or over-relaxation factor. When C<0, the equation is under-relaxed as the update to the first step is reduced by that factor and thereby effectively dampens the equation solution. Reducing this factor requires that the initial guess is in a fairly close proximity to the final solution, otherwise the required number of iterations to reach the solution could be increased and the under-relaxation does not serve its purpose. To enhance the stability of the simulation, the under-relaxation factors for the pressure, momentum, energy and species equation were therefore initially reduced with approximately 20% from the default values. Despite these changes, the instabilities still persisted in the simulation.

Additional steps to enhance convergence was therefore made by altering the different options in the algebraic multigrid solver settings. In a multigrid solver the simulation results are calculated for a fine mesh and the solution is then transferred onto a coarser

45
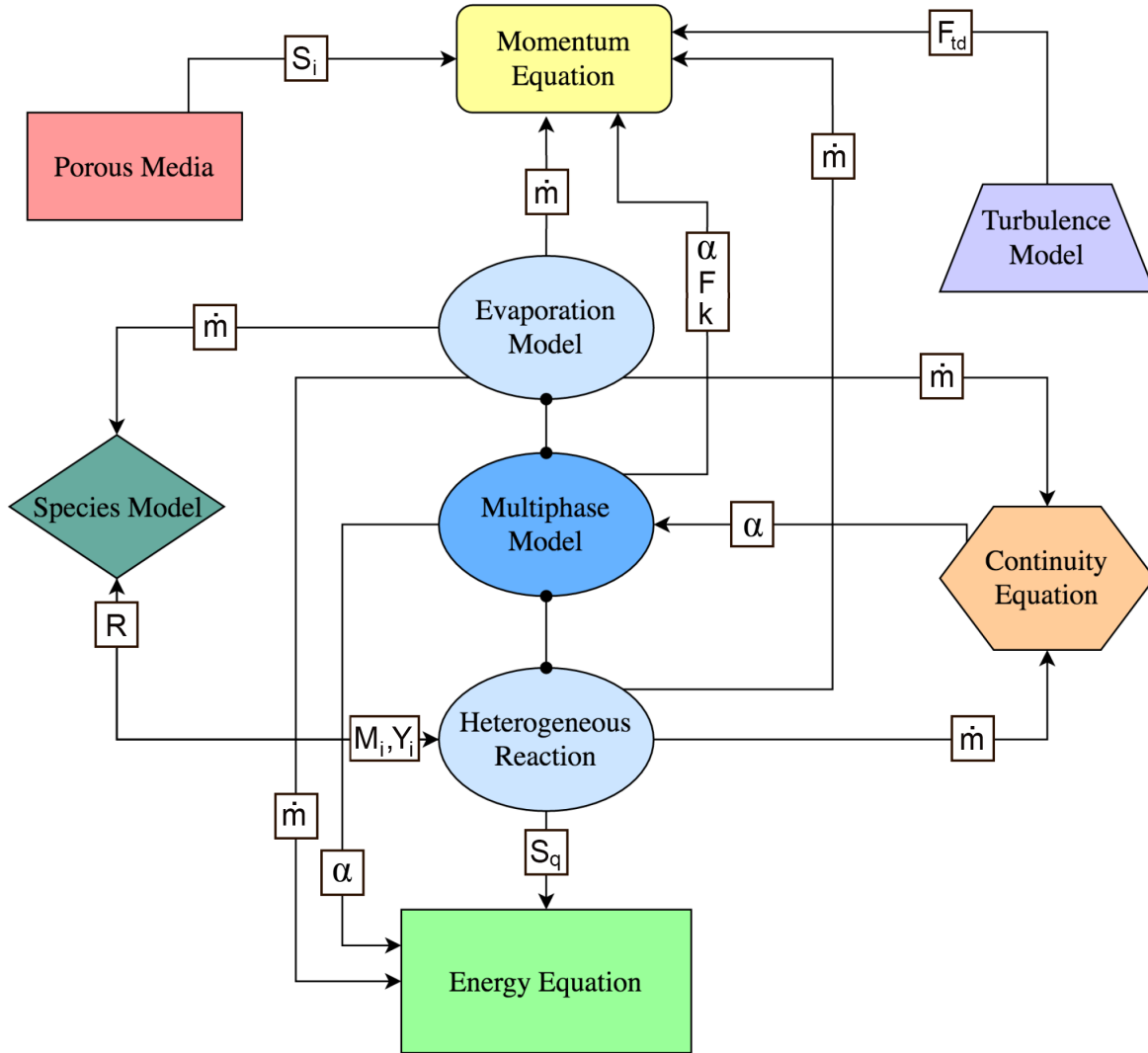
Figure 5.2. Figure of the information exchange between the different equations and models in Fluent.

mesh to remove numerical noise [53]. This process of transferring the solution is continued onto a coarser and coarser mesh. When an adequate level of noise is removed the solution is transferred in a similar iterative process back to the fine mesh again and the cycle has ended.

In Fluent, different multigrid solvers may be utilised. They consist of a F-cycle, V-cycle and W-cycle, where the differences between these models are governed by how the coarsen-refinement cycle is performed. The simulation cycle method was therefore changed from V-cycle to a W-cycle with an increased number of total cycles. In fluent there also exists two types of multigrid solvers, the aggregative AMG solver (AAMG) and the selective AMG solver (SAMG). According to the Fluent User guide [37], the SAMG solver has a better convergence rate than the AAMG. The SAMG is therefore the better choice when simulating flow with strongly varying (anisotropic) diffusive coefficients, which occurs in problems with porous media, conduction with anisotropic thermal conductivities, and multiphase problems. This solver was therefore used in this simulation. In addition

to the SAMG solver a the bi-conjugate gradient stabilized method (BCSTAB) was used as a stabilisation method.

An improved stability was observed when the multigrid solver settings were altered, but a fully convergent solution was not obtained. To further evaluate what the root cause for this issue was, the case was therefore split into different sub-cases to reduce the complexity of the simulation. The first case was a simplified version of the second, and the second a simplified version of the third case. The solution for one level would therefore be used as an initial solution for the flow field in the next level.

The first case consisted of the thruster without the porous media and reaction enabled. At the inlet of the thruster, oxygen gas and water vapour entered the domain with a mass flow rate of 0.15 kg/s, where the species mass fraction were defined by the same rate that would result from the decomposition process. When the first case had converged, the second case would then include the porous media and thereafter the reaction would be enabled in the third case.

In the simulation of the first case, convergence was still not obtained. The mass flow rate at the inlet was then reduced to 0.01 kg/s and incrementally increased to reach the final mass flow rate of 0.15 kg/s. In this simulation process it was observed that the solution diverged when the Mach number reached 0.7 in the nozzle throat. This leads to the conclusion that the Eulerian multiphase model is not capable of simulating the compressible flow for the gas phase mixture present in this simulation.

As discussed in subsection 3.1.1, the Eulerian multiphase model was selected as the phases in a HTP thruster are not in a state of equilibrium, which the mixture model assumes. Due to the convergence issues found with the Eulerian model, a final attempt to model this fluid flow was performed with the mixture model enabled.

Chapter 6

Case Setup

6.1 General Setup

All three cases were run as a transient simulation with the pressure based solver for an axisymmetric geometry. The transient solution method was selected as the thruster fluid flow may contain oscillating effects due to the compressibility and the possibility of fluid flow separation, normal shocks and shock waves in the nozzle zone. As described in chapter 3, the $k-\omega$ turbulence model was selected, and the energy equation was enabled.

The mixture multiphase model consisted of two phases, where the gas phase containing air, oxygen gas and water vapour as species was selected as the primary phase in the simulation. For the third case, the liquid phase was introduced as a mixture of hydrogen peroxide and water. The material properties of the mixture is given in Table 6.1 for the gas phase, and the liquid phase is given in Table 6.2. The species properties for the gas phase is given in Table 6.3 and for the liquid phase the properties are found in Table 6.4.

Table 6.1. Gas phase mixture properties in the simulation.

Properties	Units	Gas-phase
Species	-	Air, O_2, H_2O(g)
Density	-	Ideal gas
C_p	J/kg-k	Mixing-law
Thermal conductivity	W/m-k	constant=0.0454
Viscosity	kg/m-s	constant=1.72e-05
Mass Diffusivity	m^2/s	constant-dilute-appx=2.88e-05

Table 6.2. Liquid phase mixture properties in the simulation.

Properties	Units	Liquid-phase
Species	-	H_2O, H_2O_2
Density	-	Incompressible-gas
C_p	J/kg-k	Mixing-law
Thermal conductivity	W/m-k	constant=0.0454
Viscosity	kg/m-s	constant=1.72e-05
Mass Diffusivity	m^2/s	constant-dilute-appx=2.88e-05

Table 6.3. Gas phase species properties in the simulation.

Properties	Units	Air	O_2	H_2O
C_p	J/kg-k	1006.43	Piecewise-linear	Piecewise-linear
Molecular Weight	kg/kgmol	28.966	31.9988	18.01534
Standard State Enthalpy	j/kgmol	0	0	-2.418379e+08
Reference Temperature	k	298.15	298.15	298.15

Table 6.4. Liquid phase species properties in the simulation.

Properties	Units	H_2O_2	H_2O
C_p	J/kg-k	2626.2	4182
Molecular Weight	kg/kgmol	34.01474	18.0152
Standard State Enthalpy	j/kgmol	-1.877803e+08	-2.858412e+08
Reference Temperature	k	298.15	298.15

6.2   Heterogeneous Reaction UDF

With the mixture model selected for the multiphase model, the built in model for the
Arrhenius equation is no longer available. A UDF was therefore written to calculate the
reaction rate of the decomposition process.

```
#include "udf.h"

DEFINE_HET_RXN_RATE(rxratedecomp, c, t, r, mw, yi, rr, rr_t)
{
        Domain *d = Get_Domain(1);

        const real R = 8.3145;
        real T, P, A0, EA, mole_frac, rho;
        real vol_frac;
        real conc[2];
        const int POROUS_ID = 8, LIQ_PHASE_ID = 1;
        const enum {gas_ph, liquid_ph};
        const enum {h2o2_w, h2o_w};
        const enum {air, o2_g, h2o_g};

        //phase thread pointer to the liquid phase
        Thread *subthread = THREAD_SUB_THREAD(t,LIQ_PHASE_ID);


        //volume fraction of the liquid phase
        vol_frac = C_VOF(c,subthread);
```

49

```
        //if the liquid is in the porous zone
        if (Lookup_Thread(d, POROUS_ID) == t){

        //pre-exponential factor for catalytic decomposition
                A0 = 2.6*pow(10,4);

        //activation energy for catalytic decomposition
                EA = 52.5*pow(10,3);
        }
        else {

        //pre-exponental factor for catalytic decomposition
                A0 = 1.0*pow(10,5.8);

        //activation energy for thermal decomposition
                EA = 71.0*pow(10,3);
        }

        //temperature of the liquid phase
        T = C_T(c,subthread);

        //density of the liquid phase
        rho = C_R(c,subthread);

        //mole fraction of HP
        mole_frac=yi[liquid_ph][h2o2_w]/mw[liquid_ph][h2o2_w];

        //concentration of HP given by ideal gas law (kmol/m3)
        conc[h2o2_w]=mole_frac*rho;

        //reaction rate kmol/(m3,s)
        *rr = 0.02*A0 * exp(-EA/(R*T)) * conc[h2o2_w]*vol_frac;
}
```

With this UDF both the catalytic and thermal decomposition would be modelled in the thruster. A detailed explanation to this code can be found in Appendix B.

6.3   Boundary Conditions

6.3.1   Case 1

The boundary conditions used in case one of the three-step simulation is found in Table 6.5

Table 6.5. Final boundary, cell zone and operating conditions of the Fluent simulation Case 1: Nozzle flow.

Boundary/Cell Zone Conditions		
Boundary/Cell zone	*Type*	*Condition*
Operating condition		Pressure = 101325 Pa
Atmosphere horizontal	wall	
		-
Atmosphere vertical	Velocity inlet	
		Pressure = 101325 Pa
		Turbulence intensity = 5%
		Viscosity ratio = 10
		Air velocity = 5 m/s
		Air temperature = 300 K
Wall-Porous and nozzle zone	wall	
		Heat transfer coefficient = 20 w/m^2-K
		Free stream Temperature = 288 K
		External Emissivity = 0.3
		External Radiation Temperature = 288 K
		Wall Thickness = 0.002425 m
		Wall material = Steel
Inlet	Mass flow inlet	
		Pressure = 2.1 MPa
		Turbulence intensity = 5%
		Viscosity ratio = 10
		Liquid mass flow rate=0.15 kg/s
		Liquid temperature = 953 K
		Species mass fraction:
		H_2O=0.53
		O_2=0.47
Outlet	Pressure-outlet	
		Gauge pressure = 0 Pa

6.3.2 Case 2

The following Table 6.6 describes the simulation boundary conditions for case 2, which includes the porous zone. The boundary conditions given in this table are only the ones which are specific and altered from case 1 as given in Table 6.5.

The values for the inertial and viscous resistance were calculated in section 3.7. When the simulation was run with these values, the pressure drop over the catalyst was found to be several magnitudes larger than the ones found by experimental data. The inertial resistance factor was then reduced to zero. The pressure drop found with these values were in close accordance with experimental values. By removing the inertial resistance, the porous media would then be modelled in accordance with the pressure drop given in the Equation 3.7.3.

Table 6.6. Boundary, cell zone and operating conditions of the Fluent simulation case 2: Porous model activated.

Cell zone	Type	Condition
Porous zone	Porous zone	
		porosity=0.2
		Viscous resistance = 1.696e+11
		Inertial resistance = 0
		Heat transfer model: equilibrium
		Solid material: silver

6.3.3 Case 3

The boundary conditions for case 3, given in Table 6.7, are only the ones that have been altered from case 1 as given in Table 6.5 and case 2 Table 6.6.

Table 6.7. Boundary, cell zone and operating conditions of the Fluent simulation case 3: Porous model and reaction activated.

| Cell zone	Type	Condition
Inlet	Mass flow inlet	
		Liquid mass flow rate=0.15 kg/s
		Liquid temperature = 287.15 K
		Species mass fraction:
		H_2O_2=0.875
		H_2O=0.125

Chapter 7

Results and Discussion: Case 1

As described in chapter 5, the simulation was split into three sub-cases. The first case includes only the gas phase present in the thruster, and was performed to evaluate the nozzle flow. The simulation was initialised by the hybrid initialisation scheme with an inlet mass flow rate of air equal to 0.00001. This was done in order to ensure that the domain only contained air before the oxygen and water vapour gas entered into the thruster.

The simulation was run at a time step of $5 \cdot 10^{-7}$ and convergence of the residuals was obtained with under 40 iterations per time step. The total time needed for the oxygen and water vapour to exit the nozzle was calculated by dividing the total length of the thruster by the inlet velocity. The calculations resulted in an approximate real time of 0.02 seconds. To reach this simulation time with the $5 \cdot 10^{-7}$ time step it requires approximately 40 000 time steps and 1.6 million iterations. With this amount of iterations the simulation was therefore run on the supercomputer Vilje at NTNU (Norwegian University of Science and Technology).

The simulation results presented in this chapter was obtained at the simulation time 0.062391 seconds.

7.1   Mass Fraction of Air

As seen in the contour plot of the mass fraction of air in Figure 7.1, the thruster has been completely filled with oxygen and water vapour.
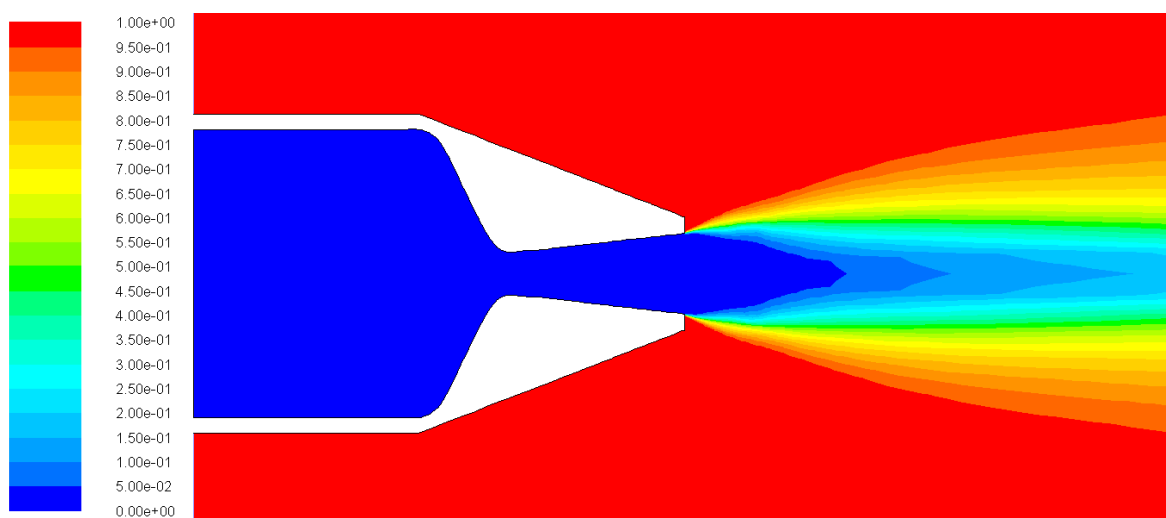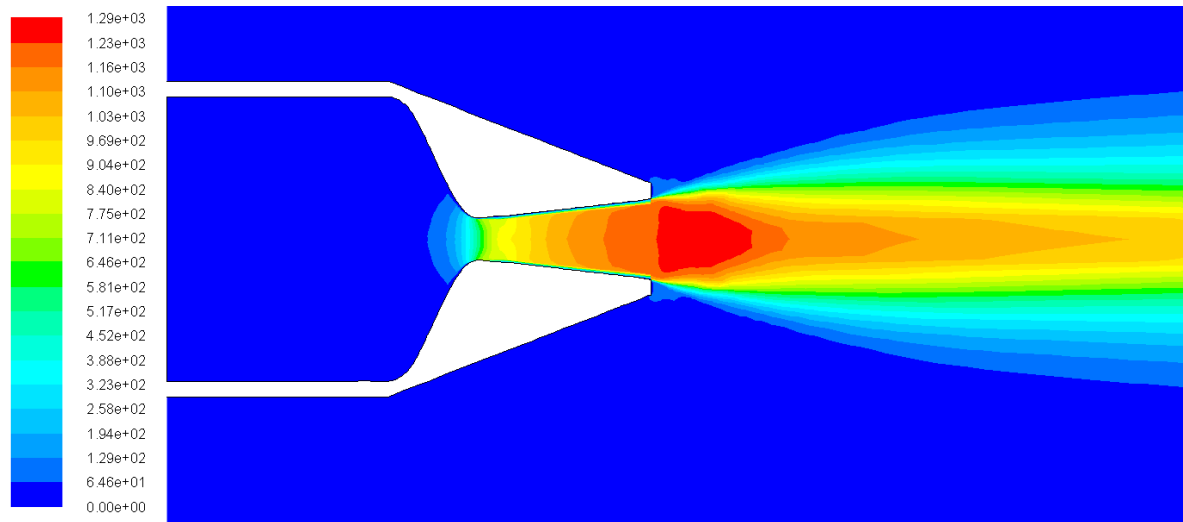

Figure 7.1. Contour plot of the mass fraction of air.

7.2 Velocity and Mach number

The contour plot of the gas phase velocity is found in Figure 7.2 with the corresponding Mach number in Figure 7.3.

Figure 7.2. Contour plot of the gas phase velocity.

As seen in Figure 7.2, the velocity approaches zero close to the wall and the no-slip condition at the wall is thereby fulfilled.

Close to the nozzle exit an increased velocity compared to the ambient air is found at the outside of the oxygen and water vapour plume. Looking at Figure 7.1, it can be seen that only air is present in this region. This result can therefore be attributed to a recirculation zone of air due to the short horizontal wall close to the nozzle exit. When air flows over the corner right above the nozzle exit, an adverse pressure gradient is found in this region and the flow would separate and establish a recirculation zone.
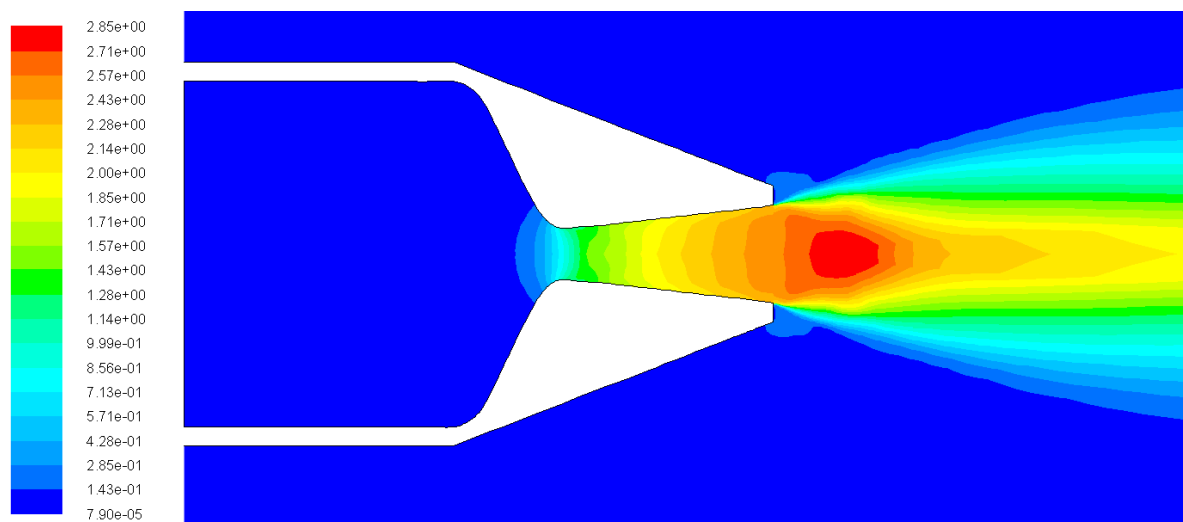

Figure 7.3. Contour plot of the gas phase Mach number.

From the contour plot of the Mach number it can be seen that the Mach number reaches

1 in the nozzle throat region, and the nozzle is thereby choked. From the nozzle throat region to the nozzle exit, the gas phase has entered into a supersonic speed regime. In this region the gases are accelerated towards the exit, which concur with the theory of a supersonic convergent divergent nozzle [9].
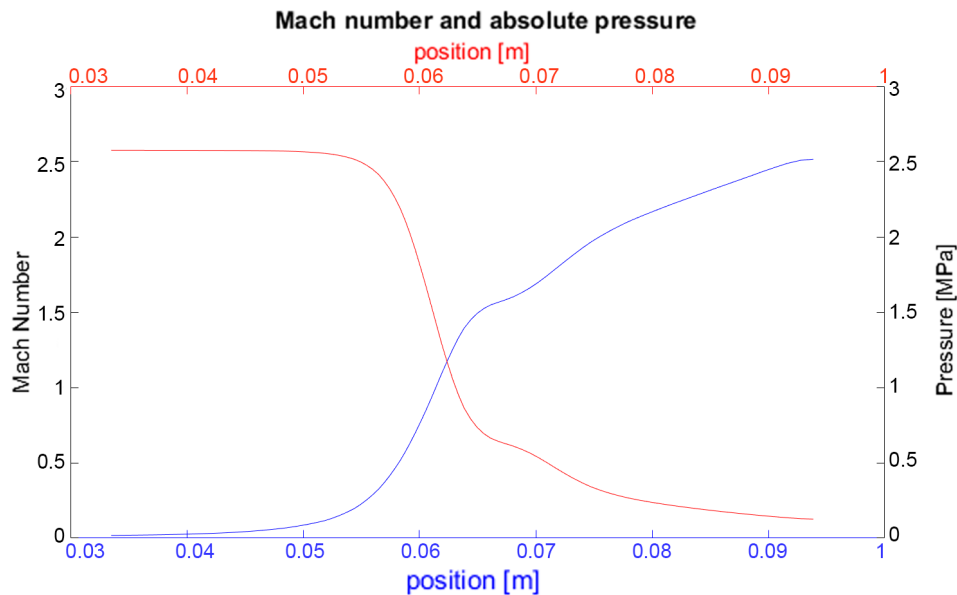
7.3   Pressure Distribution

The contour plot of the absolute pressure field in the thruster is found in Figure 7.4.
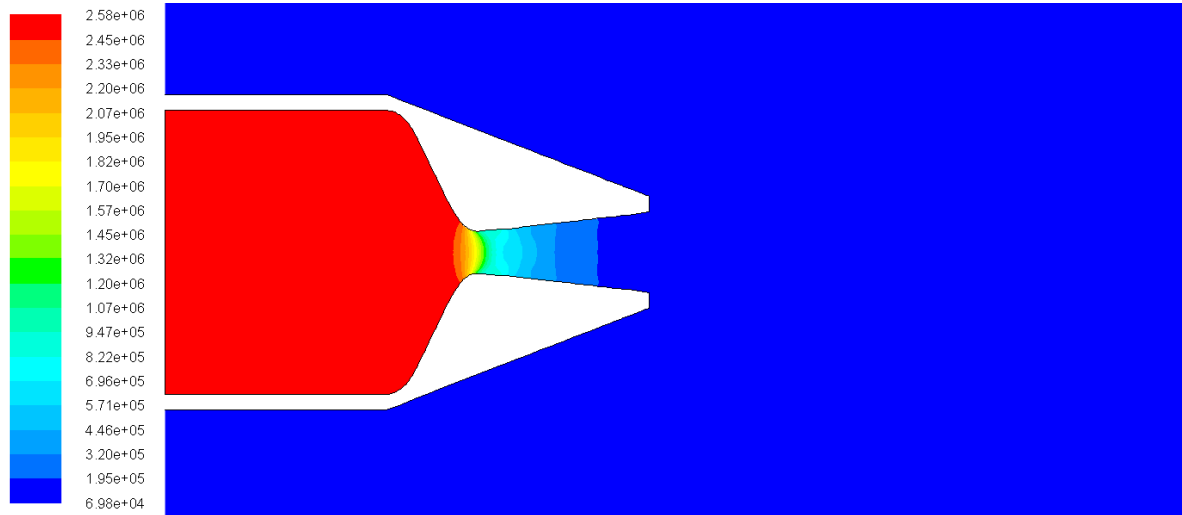
Figure 7.4. Contour plot of the mixture absolute pressure.

When the flow enters the nozzle and transitions into a supersonic flow, the pressure decreases towards the nozzle exit.


Figure 7.5. Plot of the Absolute pressure and Mach number versus the position of the Nozzle.

Taking a closer look at the pressure and Mach number along the axis of the nozzle, a small bump in both pressure and Mach number can be seen in Figure 7.5. The reason for this was found to be caused by a small offset in the conical form in the nozzle divergent section. With this error accounted for, the results show that they concur with the theory of a supersonic convergent divergent nozzle [9].

7.4   Temperature

The contour plot of the gas phase static temperature is found in Figure 7.6, and the total temperature contour plot is found in Figure 7.7.
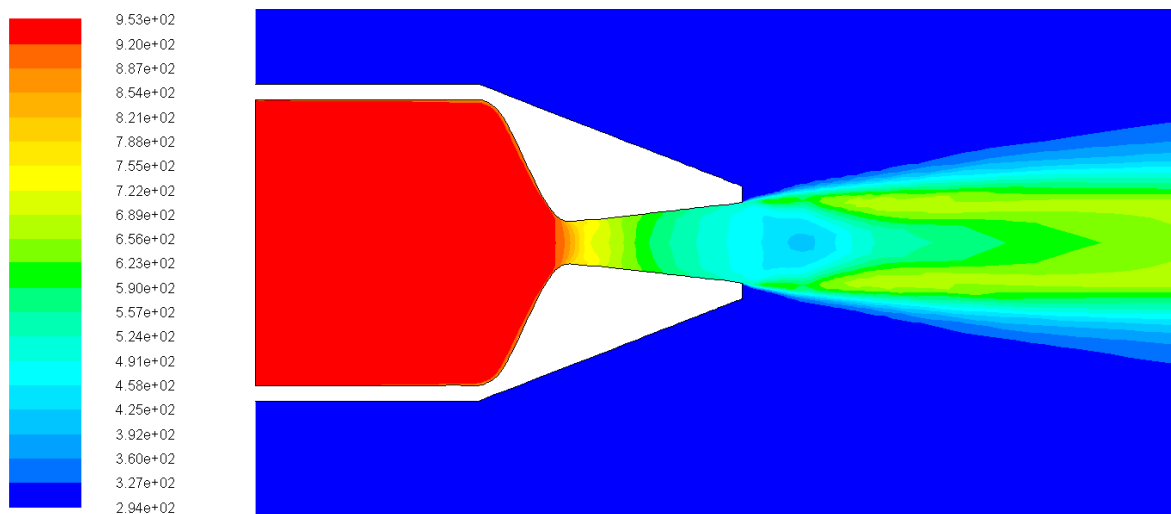
Figure 7.6. Contour plot of the gas phase static temperature.
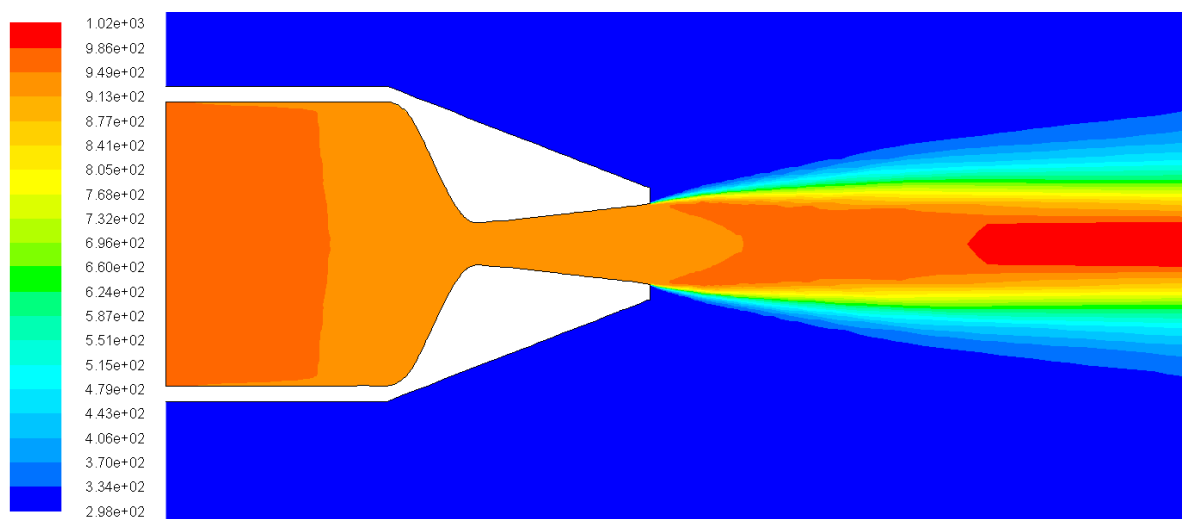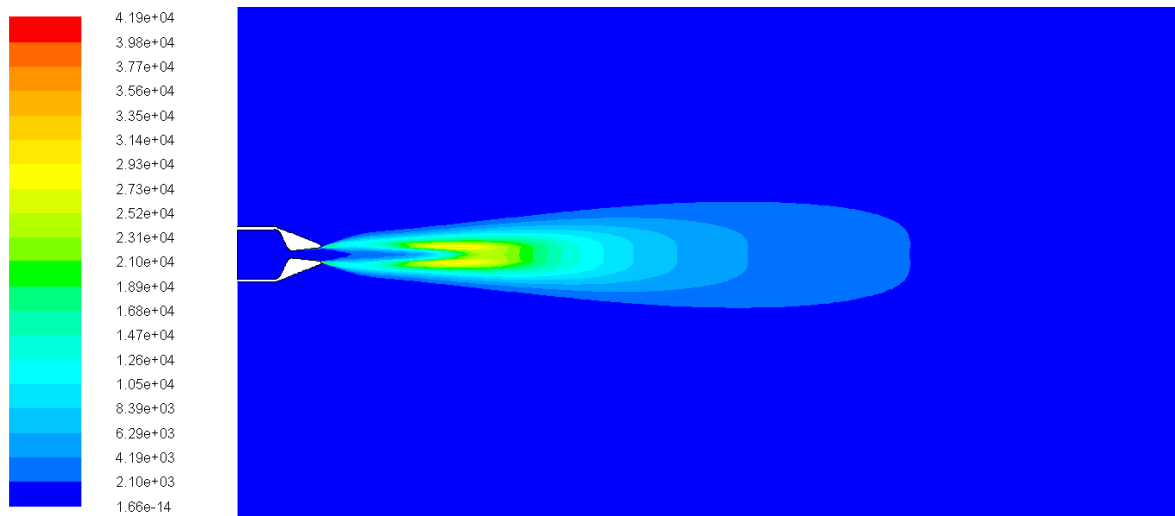

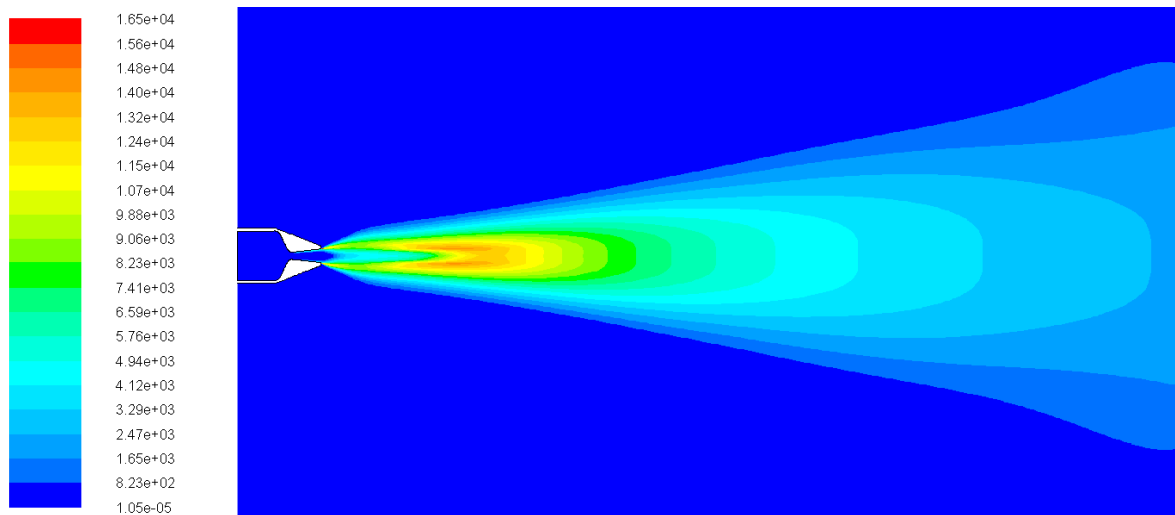**Figure 7.7.** Contour plot of the gas phase total temperature.

As seen in Figure 7.6, the static temperature remains constant until the flow reaches the nozzle throat and transitions to supersonic flow and the static temperature decreases towards the nozzle exit. The total temperature, as seen in Figure 7.7, in a compressible gas

is the same as the fluid flow stagnation temperature. The total temperature remains fairly constant inside the thruster. A small change can be seen inside the catalyst chamber, where in this simulation a catalyst is not present. As the simulation is not adiabatic, this change can be accorded for by the heat loss at the walls of the thruster. In the nozzle region the stagnation temperature remains constant which is in accordance with supersonic nozzle flow [9].
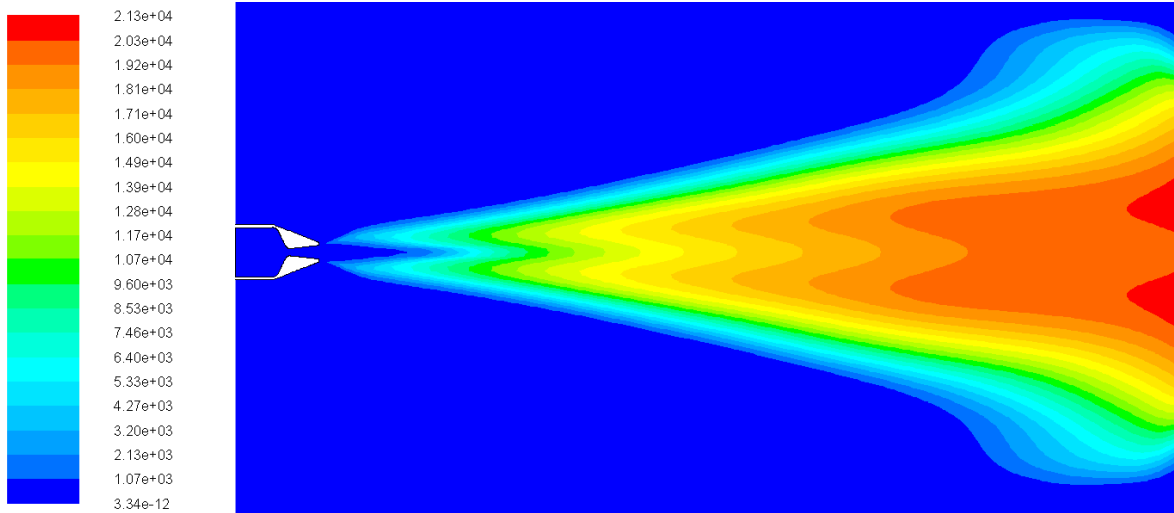
7.5 Turbulence

Figure 7.8. Contour plot of the gas phase turbulent kinetic energy.

Figure 7.9. Contour plot of the gas phase turbulent intensity.

Figure 7.10. Contour plot of the gas phase turbulent viscosity ratio.

As seen in Figure 7.8 and Figure 7.9, the turbulent kinetic energy (TKE) and turbulent intensity are largest close to the plume boundary. Due to viscous dissipation, the TKE is reduced further downstream in the plume. This can be explained by the fact that there is no production of TKE in the plume. As a result of the energy cascade, where energy is transfered from larger to smaller scales, the turbulent eddies become unstable and breaks up into smaller and less energetic eddies until the viscous forces are dominant and completely dissipates the TKE [54]. Figure Figure 7.10 confirms this, as it shows that the turbulent viscosity becomes more dominant in the region where TKE is reduced.

Chapter 8

Results and Discussion: Case 2

The second sub-case in this simulation consisted of the same boundary conditions and properties as case 1, but with the inclusion of the catalyst modelled as a porous media. The flow field solution to case 1 was used as an initial field, and the results given in this section are described at the simulation real-time of 0.078891 seconds.

8.1   Pressure Distribution
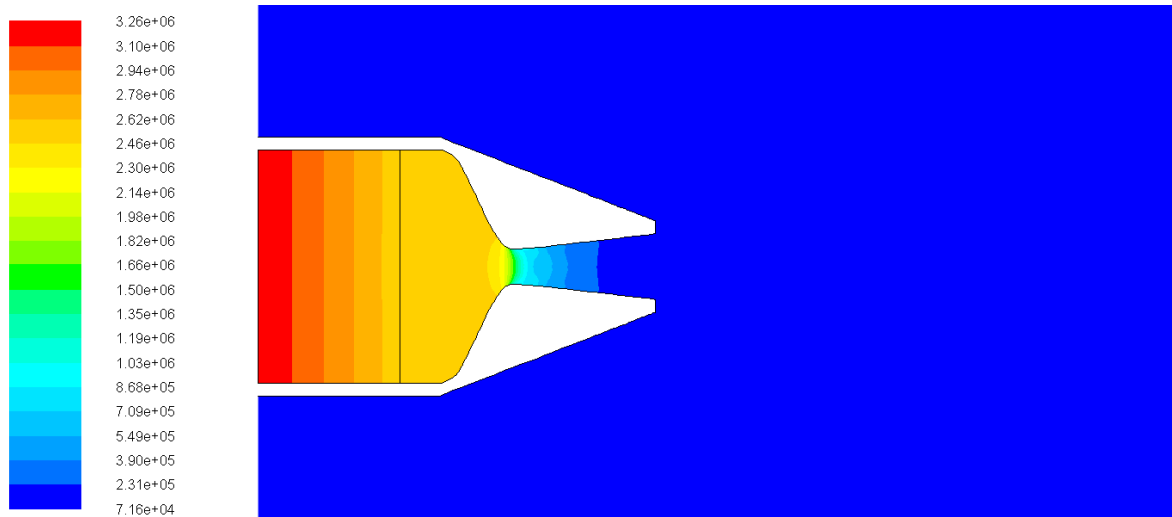
Figure 8.1. Mixture absolute pressure.

Compared to the pressure results obtained in the first case, Figure 7.4, the pressure at the inlet has increased due to the flow resistance in the porous media as seen in Figure 8.1.
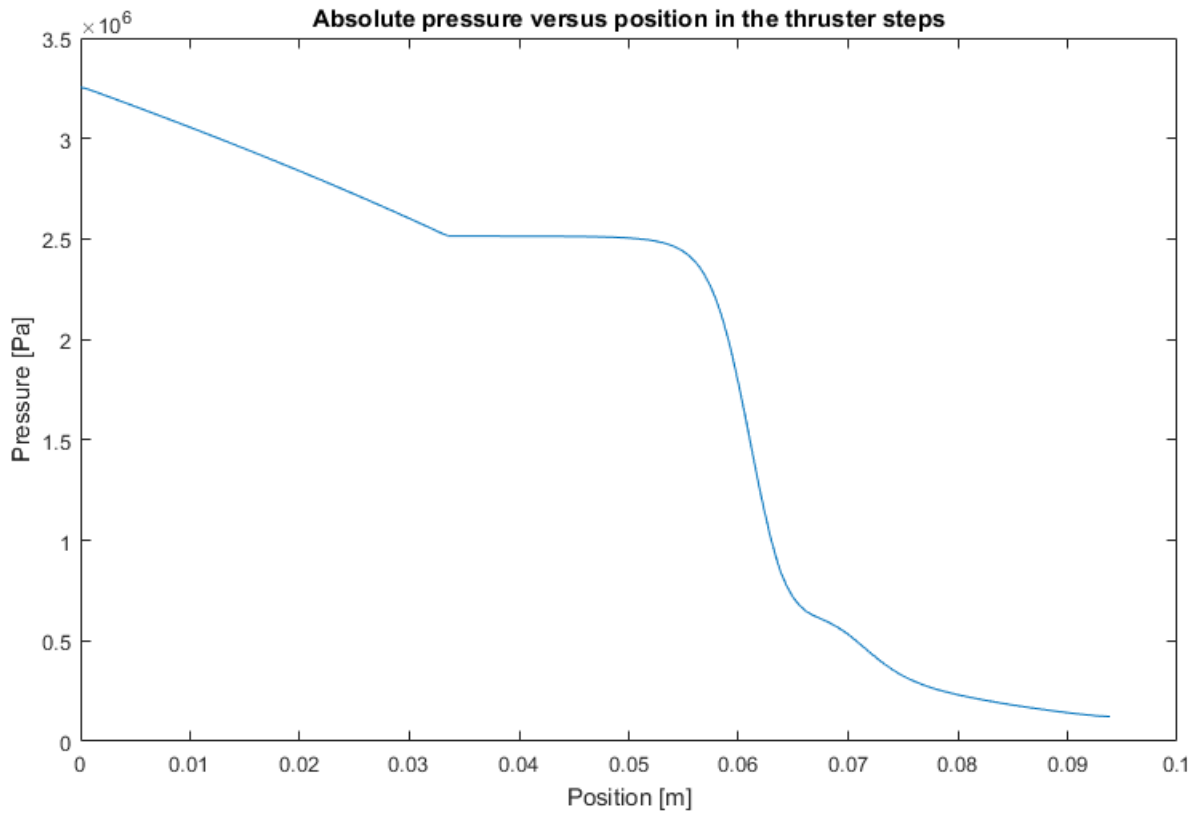
Figure 8.2. Mixture absolute pressure versus position along the axis of the thruster.

The pressure drops linearly over the catalyst, as seen in Figure 8.2, and the total pressure drop is equal to 0.74 MPa.

8.2 Temperature
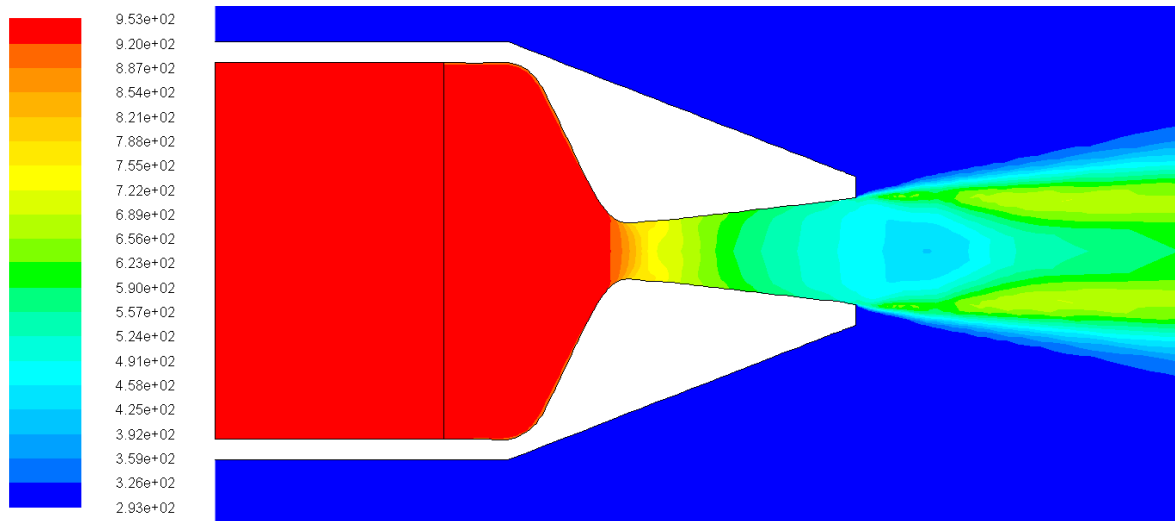
Figure 8.3. Contour plot of the gas phase static temperature.
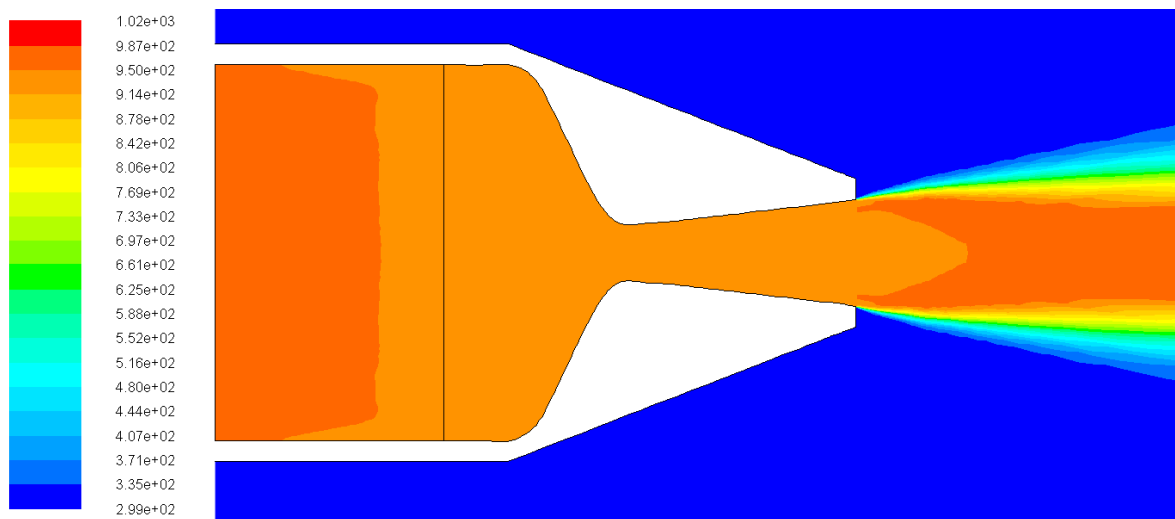
Figure 8.4. Contour plot of the gas phase total temperature.

The temperature in the thruster displays little to no changes compared to case 1, as discussed in section 7.4.

8.3 Mach Number
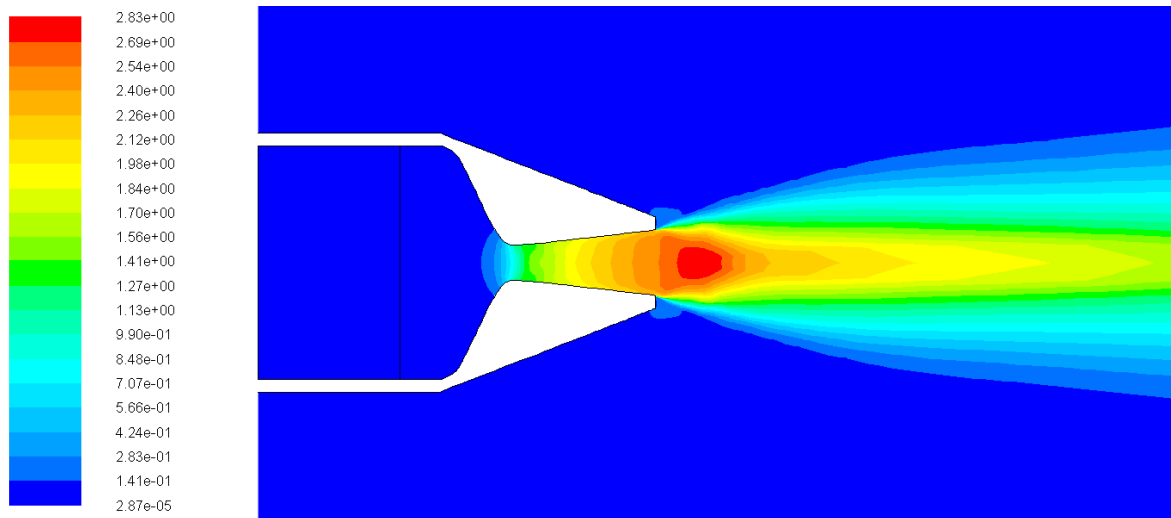
Figure 8.5. Contour plot of the gas phase Mach number.

The Mach number contour plot, as seen in Figure 8.5, shows a similar behaviour to Case 1, as discussed in section 7.2, and is displaying a behaviour which is in accordance with supersonic flow in a nozzle [9].

Chapter 9

Results and Discussion: Case 3

The third and final simulation case utilised the solution to the second case as an initial field. The liquid phase, consisting of HTP and water entered into the catalyst and reaction was enabled. During this simulation process the time step had to be reduced to $1 \cdot 10^{-10}$ in order to achieve convergence for each time step.

After approximately 2000 iterations the simulation solution diverged. The cause of this divergence was reported by Fluent to be linked to an issue in the x-momentum equation.

The results from the time step prior to divergence displayed that the pressure had increased by a factor of 2. With a pressure increase at this level over a short period of time, large gradients are present in the domain. The convergence issue could then be assumed to be linked to the porous model in the simulation. An attempt to simulate case 3, where the porous media was removed, was made based on the solution obtained in case 1. The same issue connected to convergence due was encountered in that case as well.

An issue connected to the momentum equation could have many causes. As discussed in chapter 5 for the Eulerian model, the equations are closely linked to each other which is also the case for the mixture model. The root cause for the stability issue with the mixture model could therefore not be clarified directly from the simulation results.

With no converged solution the results in this section, from the simulation of case 3 based on case 2 with porous media, are therefore presented without any further discussion of the results.

9.1 Reaction

9.1.1 Reaction Rate

Figure 9.1. Contour plot of the heterogeneous reaction rate.

9.1.2 Heat of Reaction
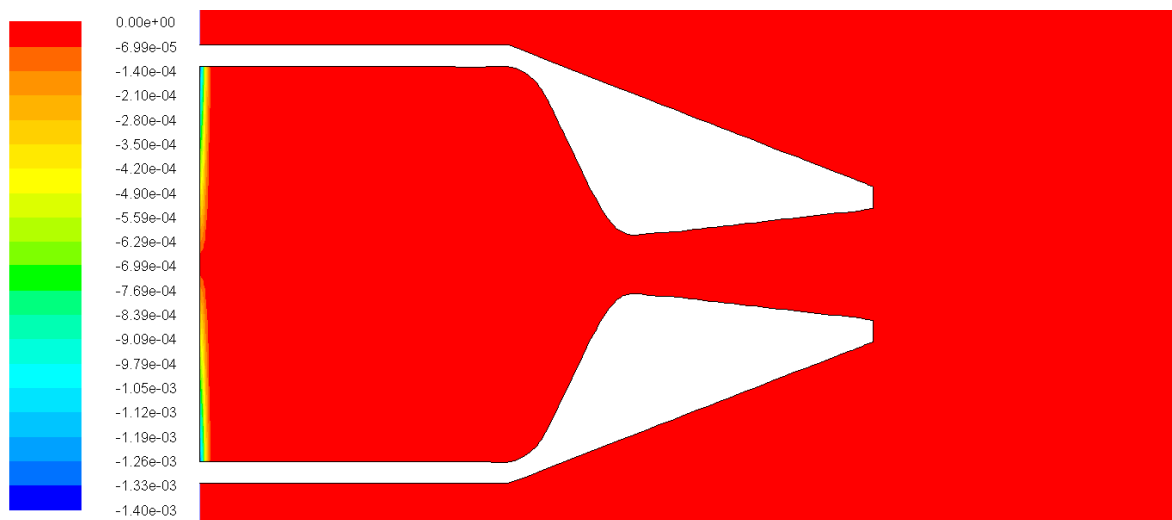
Figure 9.2. Contour plot of the heat of reaction.

9.2   Pressure Distribution
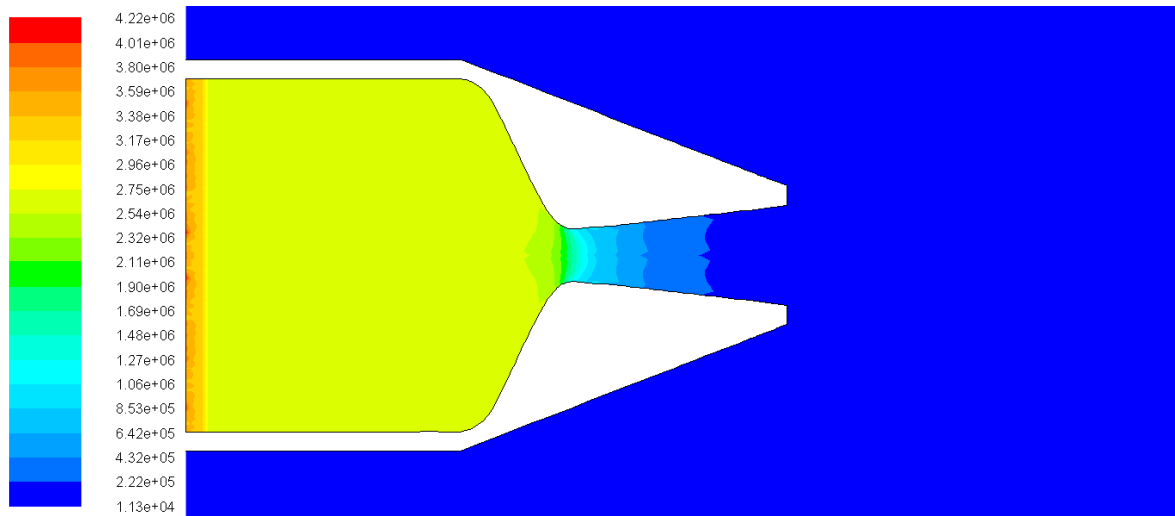
Figure 9.3. Contour plot of the mixture absolute pressure.

9.3   Temperature
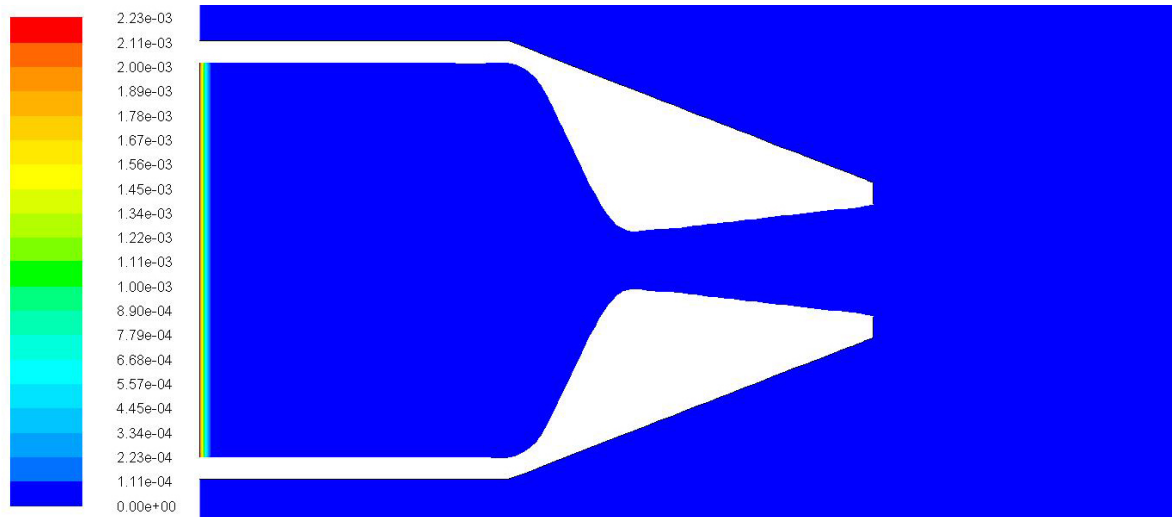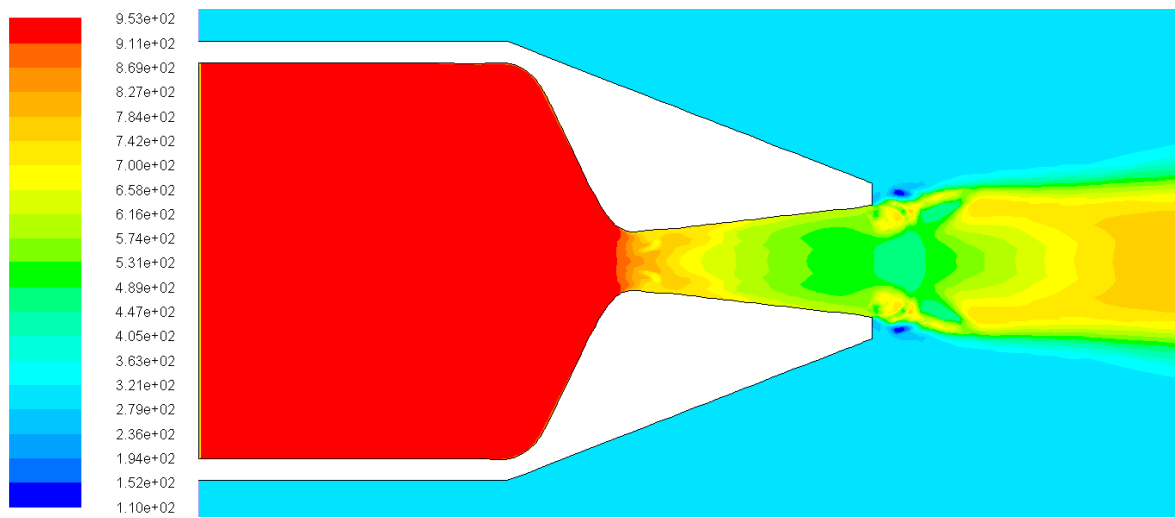

Figure 9.4. Contour plot of the static temperature.

9.4 Phase Volume Fractions
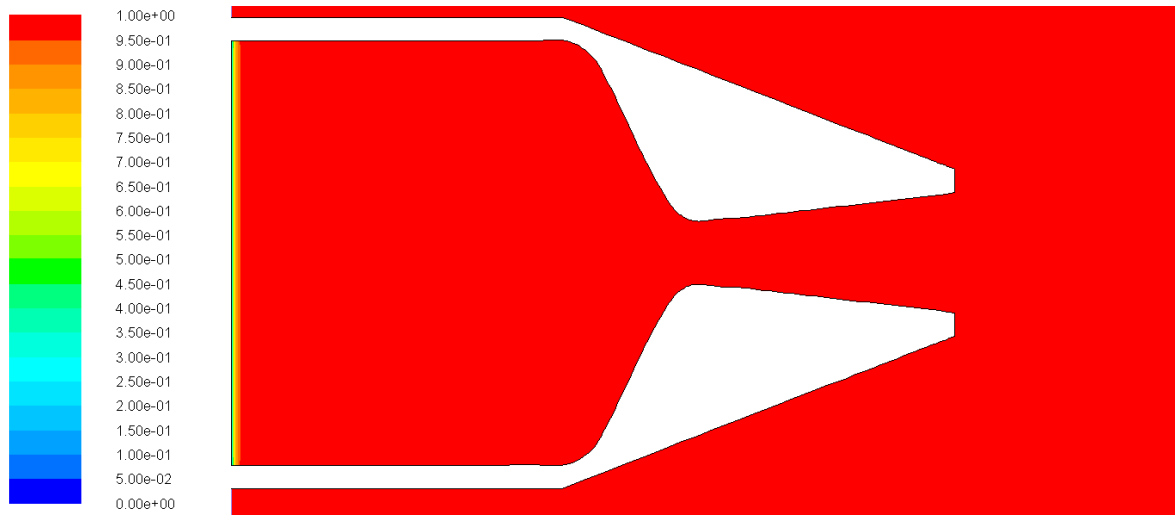
Figure 9.5. Contour plot of the gas phase volume fraction.

Chapter 10

Model Validation and Verification

10.1 Thrust Convergence

To validate that the simulation had reached a steady state condition, the time evolution of the thrust generated was evaluated. The thrust was calculated by

$$T = \dot{m}_{outlet} v_{outlet} - \dot{m}_{inlet} v_{inlet}, \tag{10.1.1}$$

and the results for case 1 are found in Figure 10.1.
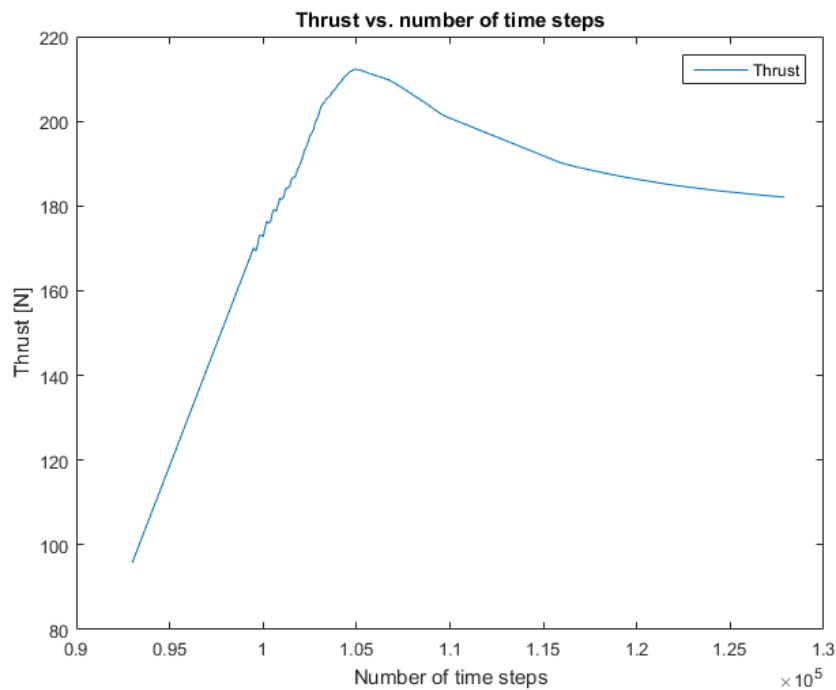
Figure 10.1. Thrust versus time-step plot.

From figure Figure 10.1, it can be seen that the thrust level was starting to fully stabilise with small changes per time step. To achieve an even more clear convergence of thrust, the simulation should have been continued. The simulation in case 1 was performed in order to find an initial field for case 2, and the level of thrust convergence was therefore deemed adequate for this purpose.

From the simulation in case 2, which included the porous media model, the thrust convergence was reached with a final thrust equal to 192 N.

10.2   y+ Values

The turbulence in a flow is significantly affected by walls, where the viscosity-affected regions have large gradients in the solution variables, and momentum and other scalar transports occur most vigorously [55]. The accuracy of the successful prediction of the near-wall region must therefore be evaluated. In order to assess this accuracy, the turbulent y^+ value in the flow field can be used for this analysis. The viscous affected region can be separated into three zones:

1. Viscous sub-layer (y+ < 5)

2. Buffer layer or blending region (5< y+ < 30)

3. Fully turbulent or log-law region (y+ > 30 to 60)

As described in subsection 3.11.2, the SST k-ω model was used to model the turbulent flow. This model is designed to be applied throughout the boundary layer, provided that the near-wall mesh resolutions are sufficient i.e. with a $y^+ \approx 1$, making it unnecessary to add a wall-function to bridge the model to the wall [55].
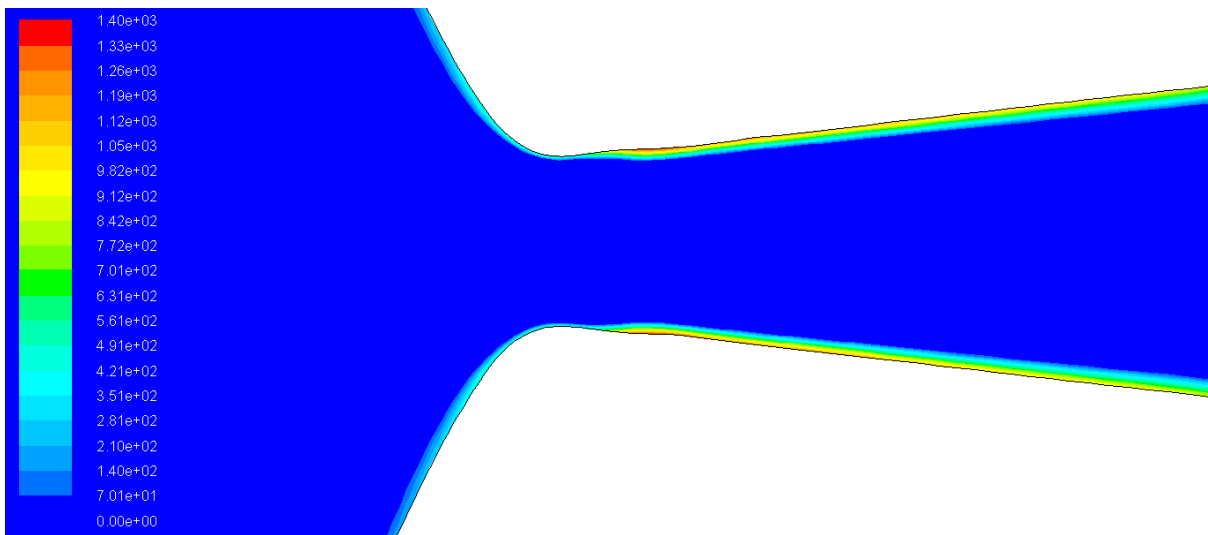
Figure 10.2. Contour plot of the y+ values in the nozzle region of the case 1 results.

As seen in Figure 10.2, the y^+ at the wall of the divergent section of the nozzle in case 1 is equal to 140. Closing up on the porous section in case 2, as seen in Figure 10.3 the y^+ value is equal to 50. With this result, the simulation is only resolving the log-law region close to the wall. Due to the large velocities in this region, the boundary layer close to the wall is very small and resolving this layer would require very refined cells and be more computationally expensive.
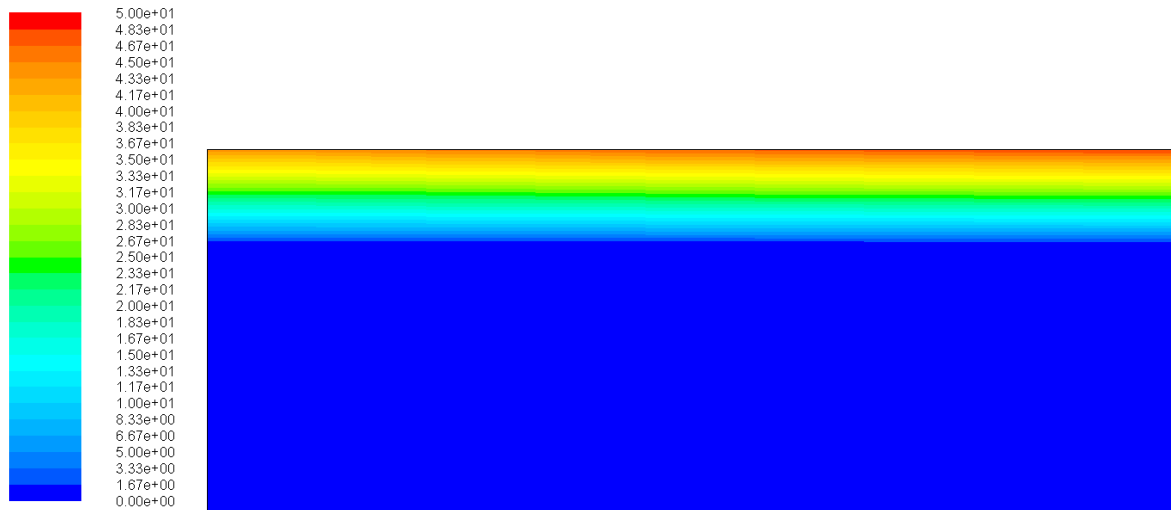
Figure 10.3. Contour plot of the turbulent y+ value close to the porous media wall in case 2.

To refine the mesh based on these results, an adaptive process was performed in fluent based on the calculated y^+ values, where an inflation layer was added to the wall region. This alteration to the mesh proved to have a strong adverse effect on the overall quality of the mesh.

By not resolving this layer is assumed effect on the heat transfer at the wall, based on the discussion presented earlier in this section. The main goal of the simulation is not to evaluate the overall heat transfer, but the catalyst fluid flow. With the deteriorative effect of adapting the mesh by the y^+ value, the mesh was therefore not further resolved.

10.3 Case Comparison wtih Star CCM+ Simulation

A similar simulation as in case 2 was performed by Øye [56]. The simulation was performed with a nozzle designed for vacuum conditions with a nozzle expansion ratio significantly larger than the case presented in this thesis. The inlet mass flow rate was at 1.225 kg/s, which is lower than the cases presented in this thesis. A multiphase model was not used, as only the gas phase was modelled, and the catalyst was modelled by an anisotropic porous model.

In the report presented by Øye, a simulation of the thruster performance was also made for atmospheric conditions. The results displayed a static temperature of 955 K in the region of the catalyst with a pressure equal to 2.0451 MPa. The temperature results are in a close proximity to the results obtained in case 2, chapter 8 with a temperature equal to 953 K.

The absolute pressure found in case 1, which includes a 1 atm operational pressure, was found to be equal to 2.58 MPa. This results in a pressure difference equal to 0.434 MPa from the simulation presented by Øye. This difference is assumed to be a result of the different nozzle designs and expansion ratios used in the simulations, in addition to the difference in mass flow rate.

The pressure in case 2 was found to be 3.26 MPa, which also includes the atmospheric operation pressure of 1 atm. The pressure obtained in this simulation is therefore not in accordance with the simulation results presented by Øye. The differences can be contributed to the same differences as in case 1, however, this indicates that the porous model has been modelled incorrectly in this thesis.

During atmospheric testing, the vacuum designed nozzle was chopped down to an expansion ratio equal to that modelled in the simulation in this thesis. In the report presented by Øye, a simulation was performed with this nozzle geometry to evaluate the Mach number at the nozzle exit. The results displayed a Mach number equal to 2.4. In case 1 and 2 the Mach number at the nozzle exit was found to be equal to 2.43 which results in a small difference compared to the results obtained by Øye. The difference can be attributed to the different geometry of the nozzle, as in this case the nozzle has been modelled as conical with a larger length than the chopped off nozzle used by Øye. This would result in a smoother transition and less losses connected to the nozzle flow.

10.4   Case Comparison with Experimental Data

Data retrieved during a vacuum chamber steady state firing (SSF) mode of the thruster was used to further analyse the validation of the simulation results. During the test, thermal probes and pressure taps were placed on the thruster with locations given in Figure 10.4.
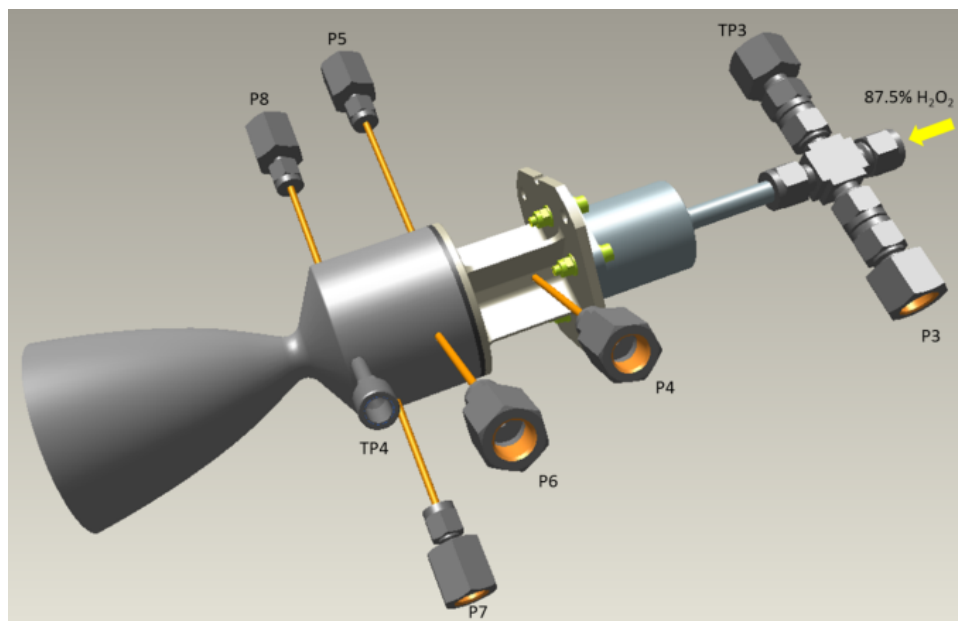
Figure 10.4. Physical location of the different pressure taps and thermal probes on the thruster during testing [11].

As seen in Figure 10.5 the pressure in the thruster at the location of pressure tap P7, as seen in Figure 10.4, reaches a pressure level close to the results found in case 1. The pressure found in this region in case 2 is much larger than the test data results.
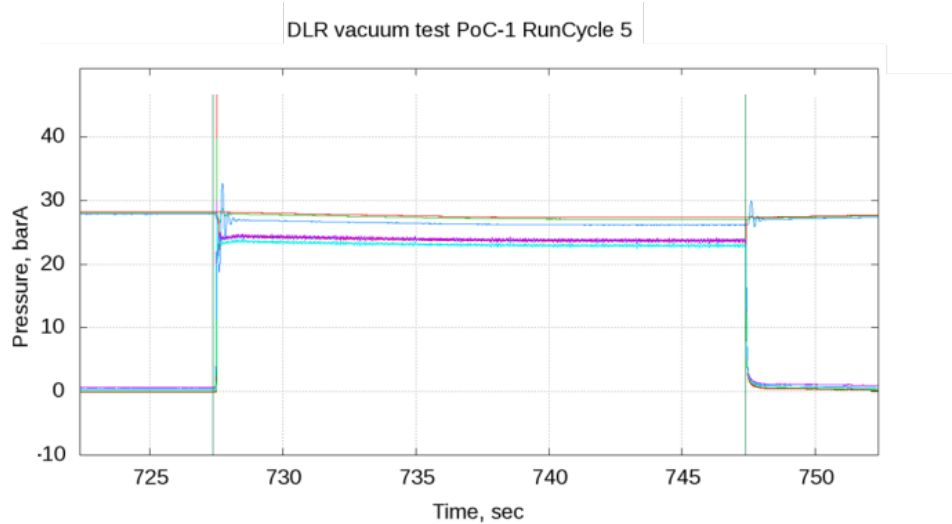
Figure 10.5. Pressure versus time at SSF high thrust mode (228 N) [11]. The purple line depicts the measured data for pressure tap P7.

According to [11], the pressure drop over the catalyst was found to be equal to 0.05 MPa. In the simulation of case 2, the pressure drop was found to be approximately 70 bar. This leads to the conclusion that the porous media is not correctly modelled in the simulation presented in this thesis. With this conclusion, the results obtained from the experimental results as described in Appendix C could have proved to give more correct results than the coefficients obtained in subsection 3.7.4. As the porous model was found not to be the root cause of the convergence issues for case 3, a simulation with these constants was not performed.
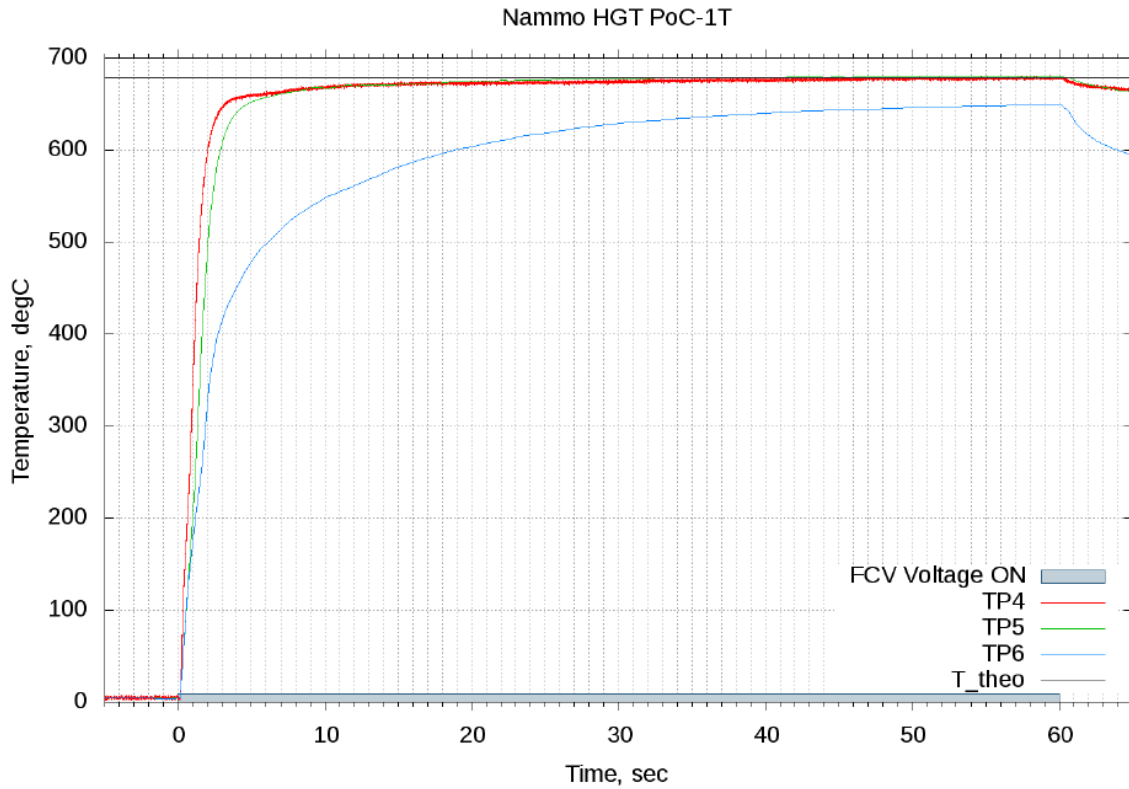
Figure 10.6. Temperature response observed on cold start without pre-heating of hot gas thruster at maximum mass flow rate [11].

The temperature test results for the different thermal probes are found in Figure 10.6. The temperature in the catalyst, measured by TP4 as seen in Figure 10.4, was found to be in a very close proximity to the results obtained both in case 1 and 2, where the temperature was found to be equal to 953 K.
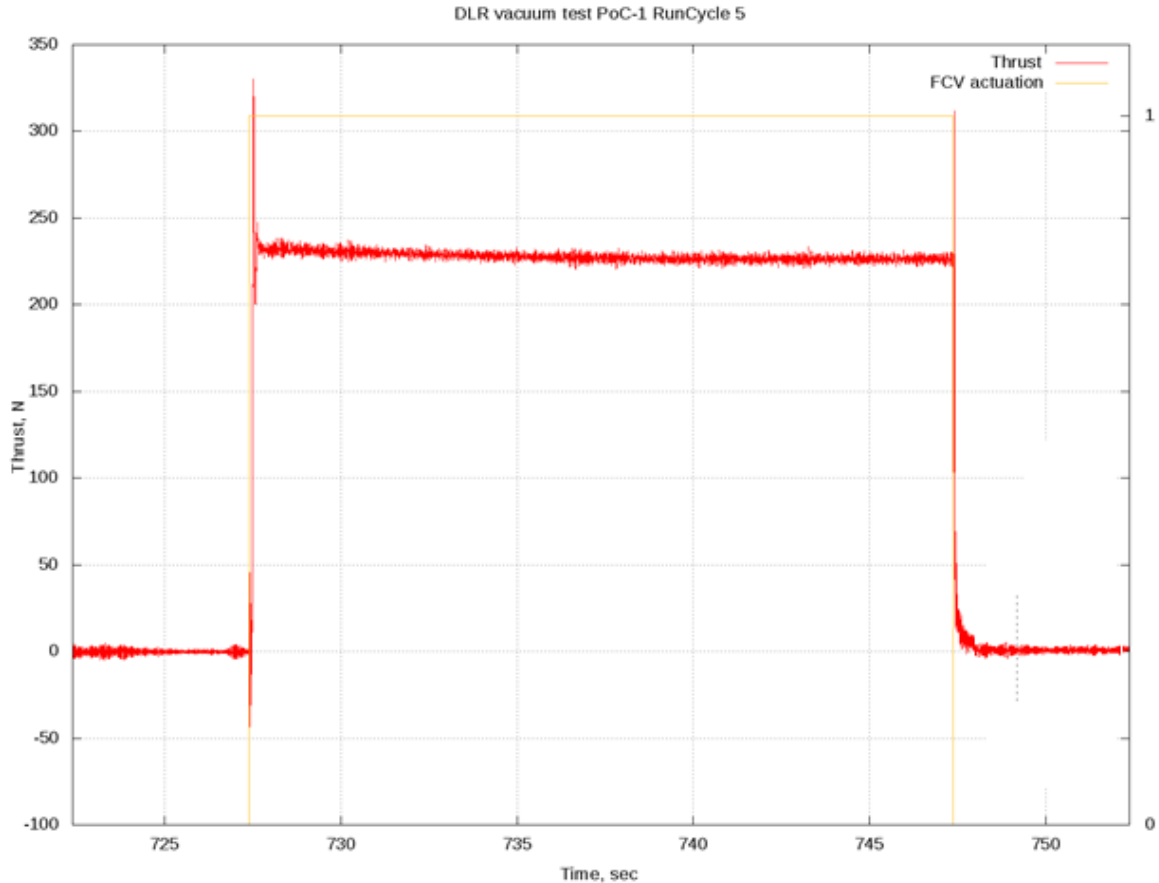
Figure 10.7. Thrust versus time at SSF high thrust mode (228 N) [11].

The thrust measured during the test is found in Figure 10.7. The resulting thrust of 228 N is larger than found in case 1 and 2, whereas in case 2 the thrust was measured to be equal to 192 N. This difference can be attributed to the fact that the test was performed in a vacuum chamber where the resistance from the atmospheric pressure is not present.

10.5   Reaction Plane

In order to validate if the reaction mechanism had been modelled correctly, experimental temperature data obtained with a higher resolution per length in the catalyst could be used to determine the reaction plane. Previous tests of the thruster system has displayed a rapid temperature change over a short distance in the catalyst. This can be attributed by the fact that lower temperatured liquid reacts very quickly into the hot gas, resulting in a dispersed flow with a diffuse boundary.

By properly simulating the reaction, a similar formation would be expected and an approximated position of this plane could have been determined. With no converged solution obtained for case 3, this comparison was not made.

Chapter 11

Conclusion

The simulations performed with the Eulerian multiphase model did not provide a converged solution of the residuals. By splitting the simulation into three different sub-cases it was found that the Eulerian multiphase model is not capable of modelling compressible flow. The three case-setups were therefore simulated by the mixture multiphase model, where the solution to the first simulation was used as an initial field for the next simulation.

Instability issues were also found with the mixture model when the reaction mechanism and the vaporisation of liquid water was enabled. The reported issue in Fluent was divergence in the x-momentum equation. An error in this equation could have many root causes, as the equations in the simulation is closely linked to each other. The results obtained prior to divergence in this case displayed a large pressure in the thruster catalyst region modelled as a porous media. To remove the porous media as a source for divergence, the results obtained from the pure nozzle flow was used as an initial field for the reaction case. The solution diverged in this case as well with the same results as the previous case. Due to the complexity of the information shared between the different equations in Fluent the issue connected to this problem was not found.

By comparing the simulation results obtained for case 1 and 2 with experimental test data the results in case 1 were verified and validated. The porous media model was concluded to be modelled incorrectly in case 2 as the pressure drop far exceeded results found during experimental test. The y+ values obtained in the solutions were used to conclude that the $k-\omega$ turbulence model used in this simulation was accurately modelled for the overall goal of the simulation.

Through the simulations performed in this thesis it was concluded that with the current setup used in this simulation it is not possible to simulate the fluid flow in a monopropellant rocket engine in ANSYS Fluent 16.2 due to stability issues connected to the Eulerian multiphase model and the heterogeneous reaction model modelled in the mixture multiphase model.

Chapter 12

Further Work

The convergence issues connected to the mixture model simulation in this thesis were not resolved. The divergence did occur when the reaction mechanism and two-resistance model was used for vaporisation. It is therefore expected that the issues are related to how these models influence the other equations. A detailed description of this has not been found in the Fluent manual, and a parametric study can therefore be used to find the most sensitive parameter for divergence. To perform the parametric study, the UDF must be optimised for parallel processing as the required time-steps taken in this simulation makes it highly inefficient to compute on a personal computer.

Furthermore, the results in this thesis proved that there are certain points of improvements to the model that can be done. The nozzle geometry includes a minor bump, which should be removed, though it is not expected to have a larger influence on the overall results. The turbulence model is not able to resolve the viscous sub-layer close to the wall. For thermal analysis purposes, this should be improved by the addition of an inflation layer close to the wall of the porous region without large alteration to the overall quality of the mesh.

The constants for porosity, viscous and inertial resistance coefficients used in the porous model must be changed based on more stable experimental results. Furthermore it is important to perform experimental research on the reaction mechanism of hydrogen peroxide, and investigate if the pre-exponential factor and activation energy found in literature is correct.

As the divergence with the Eulerian multiphase model was due to compressible flow, though the Fluent manual states that this should be possible [37], there might be issues connected to the solver in the Fluent version 16.2 that has been used for this simulation. The simulation should therefore be performed with later editions to see if this issue has been resolved.

Bibliography

[1] Charles D. Brown. Monopropellant systems, 2002. URL `http://www.globalspec.com/reference/28350/203279/4-4-monopropellant-systems`. Accessed 21.11.2015.

[2] Airbus Defence and Space. 400 n chemical monopropellant hydrazine thruster, 2003. URL `http://www.space-propulsion.com/spacecraft-propulsion/hydrazine-thrusters/400n-thruster.html`. Accessed 11.06.2016.

[3] Airbus Defence and Space. Galileo - europe's global navigation satellite system, Accessed 21.11.2015. URL `http://www.space-propulsion.com/spacecraft-propulsion/showcase/galileo-esa.html`.

[4] Marcel J. Sidi. *Spacecraft Dynamics and Control: A Practical Engineering Approach.* Cambridge University Press, 1997.

[5] Peroxide Propulsion. Decomposition catalyst, Accessed 06.12.2015. URL `http://www.peroxidepropulsion.com/catalysts.php`.

[6] Timothy P. Morgan. Rockets shake and rattle, so spacex rolls homegrown cfd, 2015. URL `http://www.nextplatform.com/2015/03/27/rockets-shake-and-rattle-so-spacex-rolls-homegrown-cfd/`. Accessed 11.06.2016.

[7] H. Scott Fogler. *Elements of Chemical Reaction Engineering.* Prentice Hall, 5th edition edition, 2016.

[8] H. S. Fogler. *Elements of Chemical Reaction Engineering.* Prentice-Hall PTR, 4th. edition edition, 2004.

[9] Frank M. White. *Fluid Mechanics.* McGraw-Hill, New York, USA, 7th edition edition, 2006.

[10] F. Incropera, d. Dewitt, T. Bergman, A. lavine. *Fundamentals of Heat and Mass Transfer.* John Wiley & Sons, New York, USA, 6th edition edition, 2007.

[11] Jan-Erik Rønnningen et. al. Development of a high-performance hydrogen peroxide monopropellant thruster for launcher applications. *Space Propulsion Conference*, 2016.

[12] *Member State Committee Support Document for Identification of Hydrazine as a Substance of Very High Concern Because of its CMR Properties.* European Chemicals Agency, ec number: 206-114-9 cas number:302-01-2 edition, May 2011.

[13] Enterprise and Industry thematic site on EUROPA. Reach - registration, evaluation, authorisation and restriction of chemicals, Accessed 21.11.2015. URL `http://ec.europa.eu/enterprise/sectors/chemicals/reach/index_en.htm`.

[14] J. Wallbank, P. Sermon, A. Baker , A. Courtney and R. Sambrook. Development of a htp mono-propellant thruster by using composite silver catalyst. *Proceedings of the 2nd International Conference on Green Propulsion for Space propulsion*, 47th, 2004.

[15] Y. Batonneau et. al. Green propulsion: Catalysts for the european fp7 project grasp. *Topics in Catalysis*, 57(6):656–667, 2014.

[16] C. Oommen et. al. Catalytic decomposition of hydroxylammonium nitrate monopropellant. *2011 International Conference on Chemistry and Chemical Process*, 10:656–667, 2011.

[17] Ball Aerospace and Technology Corporation. Green propellant infusion mission (gpim), 2016. URL `http://www.ball.com/aerospace/programs/gpim`. Accessed 13.06.2016.

[18] G. Sutton and O. Biblarz. *Rocket Propulsion Elements*. Wiley, New York, 8th edition edition, 2010.

[19] R. Humble, G. Henry and W. Larson. *Space Propulsion Analysis and Design*. McGraw-Hill, 1995.

[20] G. Goor, j. Glenneberg and S. Jacobi. Hydrogen peroxide. *Ullmann's Encyclopedia of Industrial Chemistry*, 2007.

[21] Stephen R. Turns. *An Introduction To Combustion - Concepts and Applications*. McGraw-Hill, third edition edition, 2012.

[22] R. Koopmans. *Modeling of Multiphase Multicomponent Chemically Reacting Flows through Packed Beds*. PhD thesis, University of Southampton, 2013.

[23] Octave Levenspiel. *Chemical Reaction Engineering*. John Wiley and Sons Inc., third edition edition, 1999.

[24] N.J.B Green. *Comprehensive Chemical Kinetics, Volume 39,Unimolecular Kinetics Part 1. The Reaction Step*. Elsevier, 2003.

[25] D.E. Hoare, J.B. Protheroe, and A.D. Walsh. The thermal decomposition of hydrogen peroxide vapour. *Transactions of the Faraday Society*, 55:283–293, 1957.

[26] N. Pearson, T. Pourpoint and W.E. Anderson. aporization and decomposition of hydrogen peroxide drops. Number 2003-4642, Huntsville, Alabama, 2003. 39th AIAA/ASME/SAE/ASEE Joint Propulsion Conference and Exhibit.

[27] J. Takagi and K. Ishigure. Thermal decomposition of hydrogen peroxide and its effect on reactor water monitoring of boiling water reactors. *Nuclear Science and Engineering*, 89(2), 1985.

[28] R.A. Holub, M.P. Dudukovic, and P.A. Ramachandran. Pressure drop, liquid holdup, and flow regime transition in trickle flow. *AIChE Journal*, 39(2), 1993.

[29] T. Oehmichen, L. Datsevich and A. Jess. Influence of bubble evolution on the effective kinetics of heterogeneously catalyzed gas/liquid reactions. part i: Reactions with gaseous products. *Chemical Engineering & Technology*, 33(6):911–920, 2010.

[30] E. Giamello, P. Rumori, F. Geobaldo, B. Fubini, and M.C. Paganini. The interaction between hydrogen peroxide and metal oxides: Epr investigations. *Applied Magnetic Resonance*, 10(1):173–192, 1996.

[31] X. Zhou and D. Hitt. One-dimensional modeling of catalyzed h_2o_2 decomposition in microchannel flows. Number number AIAA/ASME/SAE/ASEE 2003-3584. 33rd AIAA Fluid Dynamics Conference and Exhibit, 2003.

[32] S. Bonifacio and A. Russo Sorge. Modelling hydrogen peroxide decomposition in monolithic beds. Number SP-635. Proceedings of 3rd International Conference on Green Propellant for Space Propul- sion and 9th International Hydrogen Peroxide Propulsion Conference, ESA, 2006.

[33] J.H. Corpening, S.D. Heister, W.E. Anderson and B.J. Austin. Thermal decomposition of hydrogen peroxide, part 2: Modeling studies. *Journal of Propulsion and Power*, 22(5):996, 2006.

[34] D. Krejci, A. Woschnak, C. Scharlemann, and K. Ponweiser. Structural impact of honeycomb catalysts on hydrogen peroxide decomposition for micro propulsion. *Chemical Engineering Research and Design*, 2012.

[35] M. Ishii and T. Hibiki. *Thermo-fluid dynamics of two-phase flow*. Springer, 2006.

[36] *ANSYS Fluent, Release 16.2, Help System, Theory Guide*. Ansys, Inc, .

[37] *ANSYS Fluent, Release 16.2, Help System, User's Guide*. Ansys, Inc, .

[38] M. Kaviany. *Principles of Heat Transfer in Porous Media*. Springer-Verlag, 1991.

[39] S. Liu, A. Afacan and J. Masliyah. Steady incompressible laminar flow in porous media. *Chemical Engineering Science*, 49(21):3565–3585, 1994.

[40] U.M.S. Costa , J.S. Andrade, H.A Makse and H.E Stanley. The role of inertia on fluid flow through disordered porous media. *Physica A*, 266:420–424, 1999.

[41] P. Macini, E. Mesini and R. Viola. Laboratory measurements of non-darcy flow coefficients in natural and artificial unconsolidated porous media. *Journal of Petroleum Science and Engineering*, 77:365–374, 2011.

[42] J. Levec and D. Nemec. Flow through packed bed reactors: 1, single-phase flow. *Chemical Engineering Science 60*, pages 6947–6957, 2005.

[43] Van P. Carey. *Liquid-vapor phase-change phenomena : an introduction to the thermophysics of vaporization and condensation processes in heat transfer equipment*. Hemisphere Publishing Corporation, 1992.

[44] Evonik Industries. About hydrogen peroxide - calculations, . URL http://h2o2.evonik.com/product/h2o2/en/about-hydrogen-peroxide/basic-information/calculations/pages/calculate.aspx. Accessed 16.06.2016.

[45] Evonik Industries. About hydrogen peroxide - physico-chemical properties, . URL http://h2o2.evonik.com/product/h2o2/en/about-hydrogen-peroxide/basic-information/physico-chemical-properties/pages/default.aspx. Accessed 16.06.2016.

[46] Calvin H. Barholomew. Mechanism of catalyst deactivation. *Applied Catalysis A: General*, 202:17–60, 2001.

[47] Peter Davidson. *Turbulence - An introduction for Scientists and Engineers.* Oxford University Press, 2nd edition edition, 2015.

[48] Frank M. White. *Viscous Fluid Flow.* McGraw-Hill, New York, USA, 2006.

[49] A. Balabel, A.M. Hegab, M. Nasr, and Samy M. El-Behery. Assessment of turbulence modeling for gas flow in two-dimensional convergent–divergent rocket nozzle. *Applied Mathematical Modelling*, 35:3408–3422, 2011.

[50] Inc. ANSYS. Lecture 7: Mesh quality and advanced topics. Training course - ANSYS CFD with FLUENT, 2015.

[51] John David Anderson. *Fundamentals of Aerodynamics.* McGraw-Hill Education, 5th edition edition, 2010.

[52] Erwin Kreyszig. *Advanced Engineering Mathematics.* John Wiley & Sons Ltd, 9th edition edition, 2005.

[53] John David Anderson. *Computational Fluid Dynamics: the basics with applications.* McGraw-Hill Inc., 5th edition edition, 1995.

[54] Stephen B. Pope. *Turbulent flows.* "Cambridge University Press", 2000.

[55] S.M. Salim and S.C. Cheah. Wall y+ strategy for dealing with wall-bounded turbulent flows. *Proxeedings of the International MultiConference of Engieneering and Computer Scientists*, 2, 2009.

[56] Ivar Øye. Performance prediction of nammo poc-1 hot gas thruster for dlr high-altityde chamber testing. *2065458*, 2014.

Appendices

Appendix A

Nozzle Coordinates

#Group	Point	X_cord	Y_cord	Z_cord	
1	1	0.0335	0.0275	0	
1	2	0.04631	0.02593	0	
1	3	0.04848	0.0228	0	
1	4	0.05121	0.0172	0	
1	5	0.05387	0.01165	0	
1	6	0.05681	0.0065	0	
1	7	0.058	0.0051	0	
1	8	0.05961	0.0042	0	
1	9	0.05961	0.0042	0	
1	10	0.06281	0.00433	0	
1	11	0.06601	0.00451	0	
1	12	0.06921	0.00488	0	
1	13	0.07241	0.00525	0	
1	14	0.07561	0.00562	0	
1	15	0.07881	0.00599	0	
1	16	0.08201	0.00636	0	
1	17	0.08521	0.00672	0	
1	18	0.08841	0.00708	0	
1	19	0.09161	0.00744	0	
1	20	0.09386	0.00780	0	
1	21	0.043	0.0275		0

Appendix B

Detailed Description of the Reaction Rate UDF

1. `Domain *d = Get_Domain(1);`

   Returns a fluid domain pointer where 1 is the mixture domain.

2. `const real R=8.3145;`

   defines the area density and universal gasconst. as constants of real type (float, double, long double).

3. `real T, P, A0, EA, mole_frac, rho, vol_frac;`

   Defines T, P, A0, EA, molefrac, rho and volfrac as real type, i.e. a float, double, long double.

4. `real conc[2];`

   Defines "conc" as an array including 2 elements of type real (float, double, long double)

5. `Const int POROUS_ID=8, LIQ_PHASE_ID=1;`

   Defines the Porous ID number, which is defined by the given zone in boundary conditions in Fluent. The water phase domain ID is set to 1 as the primary phase-level is defined as 0 and the secondary phase 1. This phase tread, by its definition in the Fluent UDF Manual, is actually a struct that includes all the information in a given BC-Zones.

6. `Const enum {gas_ph, liquid_ph};`

   Gas phase and Liquid phase is here given values of 0 and 1 respectively.

7. `Thread *subthread = THREAD_SUB_THREAD(t, LIQ_PHASE_ID);`

   The function uses t, which is a cell thread (actually a pointer) at mixture level. This points to a struct in the given zone you will be applying the reaction to. The function returns a pointer to the struct in the primary phase that corresponds to the same zone as in the mixture. In simpler terms, when standing at a given point, a pointer to the data for the liquid phase in the same spot is retuned in this function.

8. `if (Lookup_Thread (d, POROUS_ID) == t)`

   This is a logic test used to check if the pointer to the porous zone is same pointer as the one that is currently being calculated. If the test returns true, the pre-exponential factor and activation energy for catalytic reaction is defined. If it returns false, the pre-exponential factor and activation energy for the thermal decomposition of HTP is defined.

9. `T=C_T(c, subthread);`

   This function is a macro for cell flow variables and returns the temperature for a given cell index in the primary phase. In this case it is used to find the temperature of the HTP in the liquid phase.

10. `rho = C_R(c,subthread);`

    As with CT, the CR is a macro for cell flow variables and returns the density of the HTP in the liquid phase.

11. `mole_frac=yi[liquid_ph][h2o2_w]/mw[liquid_ph][h2o2_w];`

    The mole fraction of the HTP is calculated from the molecular weights and the species mass fraction of HTP.

12. `conc[h2o2_w]=mole_frac*rho;`

    The mole fraction calculated in the previous step and the density of HTP is used to calculate the concentration of HTP by the ideal gas law.

13. `*rr = 0.02*A0 * exp(-EA/(R*T)) * conc[h2o2_w]*vol_frac;`

    The reaction rate of HTP decomposition by either thermal or catalytic reaction is calculated based on the Arrhenius equation with constants found in litterature. An additional factor is included in the equation, 0.02, which is defined by the estimated volume fraction that is actually taking part in the reaction.

Appendix C

Experimental Data; Porous media

The catalyst pressure drop is modelled by porous media, as discussed in section 3.7. To find the inertial resistance and viscous resistance constants to be added to the model simulation the pressure drop at different mass flow rates were examined by experimental data and are plotted along with their respective polynomial trendline in Figure C.1.
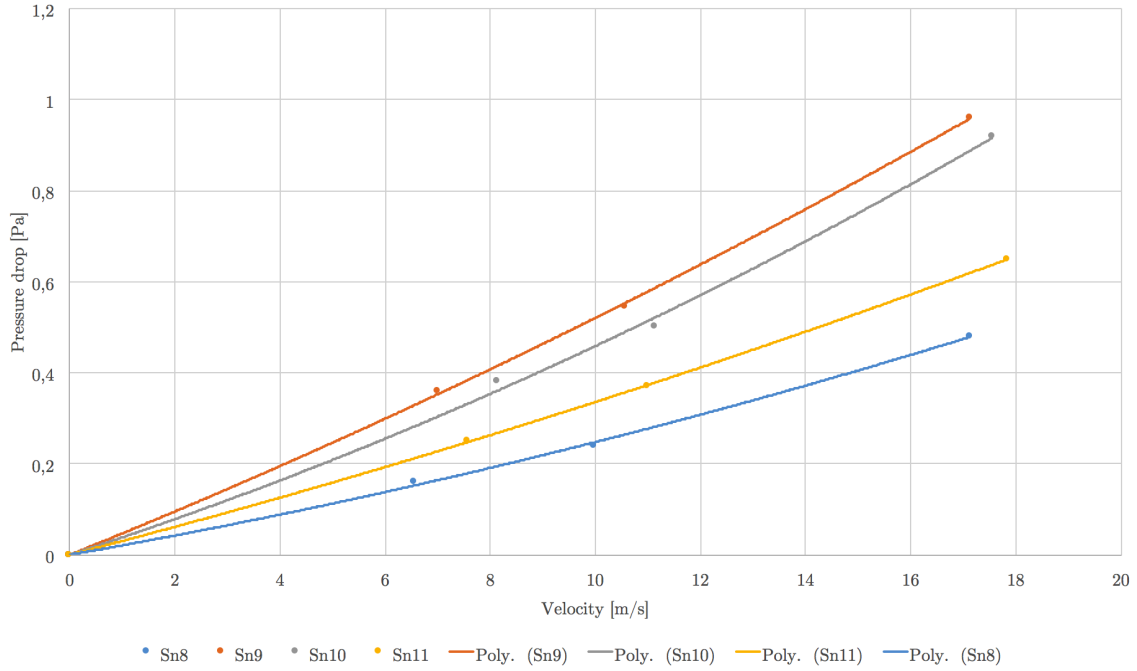
Figure C.1. Pressure drop at different velocities and their corresponding polynomial trendline.
The corresponding trendlines for the functions were found to be:

$$\Delta P_{Sn9} = 0.0004473v^2 + 0.0203v$$
$$\Delta P_{Sn10} = 0.00055v^2 + 0.04655v$$
$$\Delta P_{Sn11} = 0.0008355v^2 + 0.0376178v \tag{C.0.1}$$
$$\Delta P_{Sn8} = 0.0003617v^2 + 0.02997v$$

From the average values found for the constants calculated for the different trendlines, the viscous and inertial resistance coefficients were found to be:

$$\frac{1}{\alpha} = 26400 \tag{C.0.2}$$

$$\beta = 0.011 \tag{C.0.3}$$